DISSERTATION

MICROWAVE STUDIES OF FERROMAGNETIC RESONANCE, MAGNONIC CRYSTALS, AND PASSIVE EARTH REMOTE SENSORS

Submitted by

Adam G. Whitney

Department of Physics

In partial fulfillment of the requirements

For the Degree of Doctor of Philosophy

Colorado State University

Fort Collins, Colorado

Spring 2026

Doctoral Committee:

Advisor: Kristen Buchanan
Co-advisor: Steven Reising

Mingzhong Wu
Hua Chen
Matthew Shores

ABSTRACT

MICROWAVE STUDIES OF FERROMAGNETIC RESONANCE, MAGNONIC CRYSTALS, AND PASSIVE EARTH REMOTE SENSORS

This thesis collects the work and results of three microwave experiments for materials science applications in the contexts of data storage, communications, and passive remote sensing. The first topic measures the Gilbert damping constant of magnetic materials at elevated temperatures. This is performed using a setup for cavity-based ferromagnetic resonance (FMR) measurements adapted to reach and measure at temperatures above 700 K. Significant effort is being made in the digital storage industry to increase the areal density of magnetic storage by using techniques such as heat-assisted magnetic recording (HAMR) and spin-transfer-torque (STT) recording. The Gilbert damping constant is directly related to the efficiency of magnetic storage because a greater damping constant corresponds to more energy required to flip the orientation of the magnetic dipole moment that represents a digital bit. Characterizing the performance at the high effective temperatures required by HAMR and expected in STT devices has not been widely available due to limitations of typical FMR measurement systems. This work demonstrates measurements of the Gilbert damping constant in STT magnetic random-access memory (MRAM) free layers at temperatures up to 560 K. A typical STT MRAM free layer design, which includes a relatively thick layer of tungsten, is compared to a novel design where the tungsten layer has been split into two thinner layers. The results show that the novel design has a reduced damping constant compared to the traditional design, and that this advantage of the novel design grows with increasing temperature.

Discussed second are measurements of spin wave propagation through thin films. The propagation is manipulated using magnonic crystals: spin-wave waveguides that have non-uniform magnetic properties affecting the transmission of the wave. For example, a thin film with spatially periodic features such as grooves will support destructively-interfering reflections satisfying the Bragg condition, resulting in wavenumbers that are forbidden to propagate. The effect of Bragg reflections is observed as strong dips in transmission amplitude (functioning as a notch filter) and as band gaps in the dispersion relation. The design space for magnonic crystals remains relatively unexplored,

and a number of nonlinear effects are predicted to be observed in designs with increased complexity. In pursuit of this, a nanofabrication recipe for yttrium iron garnet thin films was developed using photolithography and wet etching. A doubly-periodic magnonic crystal with two alternating lattice periods was fabricated and the transmission of surface spin waves was measured using a vector network analyzer. It was observed that the transmission dips were stronger at wavenumbers satisfying the Bragg condition for both lattice periods, which is a distinct result from singly-periodic designs, and that the wavenumbers satisfying the Bragg condition corresponded to an effective period equal to the sum of the two periods.

Presented third is the emissivity characterization of a novel blackbody calibration target for use in passive remote sensing microwave radiometers. State-of-the-art blackbody calibration targets are microwave-absorbing epoxies that are ferrite-loaded and arranged in arrays of pyramids to maximize loss. These targets are excellent approximations to a blackbody, meaning that the radiometric brightness temperature measured by the radiometer is approximately equal to the physical temperature of the target. However, state-of-the-art targets are disadvantaged by their mass and volume and by thermal gradients that exist across the pyramids, which is a source of uncertainty that can be difficult to characterize. Calibration targets based on metamaterial absorbers are presented that address both of the aforementioned disadvantages in pyramidal targets via their planar design. Monostatic measurements of the metamaterial-based blackbody calibration targets show their emissivity as a function of frequency in bands relevant to remote sensing of the Earth's atmosphere, and nearly all of the targets reach an absorptivity target of 30 dB. A radiometer is used to support the result at the highest frequencies with measurements that directly determine emissivity from the physical and radiometric temperatures of the metamaterial.

ACKNOWLEDGMENTS

I entered graduate school with a clear goal—to get a degree—and maybe half of an idea of how to achieve that goal. Left to my own devices, I would probably be just about where I started. I've been fortunate to have people that I could call upon who were able see the bigger picture and a pathway towards it, who reminded me that I was more capable than I sometimes thought, and who kept me sane for the last seven(!) years. Time flies when you're having fun. I've crossed paths with lots of people during this time, and I think each of them is worthy of some appreciation.

First and foremost I would like to thank my professors and advisors, who helped me become the researcher I am today. I would like to thank Dr. Mingzhong Wu, who inspired me early on by noting that, by the end of my research, I would be the expert on the things that I went to him for guidance on (which was most things, and is still many); Dr. Steven Reising, who welcomed me with open arms into a field in which I had little background when it was unclear how I would continue; Dr. Kristen Buchanan, who more than once took a complicated-seeming situation and helped me find a simple, achievable solution; and Dr. Carl Patton, a titan in his field who has always been available to teach and learn, and whose open-door discussions and fundamentals approach instilled in me the importance of a thorough understanding of my work.

I would like to especially thank my wife, Jackie, who seemed to enjoy my company enough to move two thousand miles away with me *and* bring home the bacon for Maggie (the cat) and myself. She's the one who makes it all feel possible. I would like to thank my parents, Mom and Dad (aka Cathy and Glenn) who simply rock, no notes, and my two brothers, Kevin and Ian, who aren't so bad themselves. Their love and support has been the foundation upon which I have been able to build anything.

Thanks to my co-conspirators Camden, Ryan, and Jamie for regular impromptu Mugs runs, time spent together working and commiserating on classes and research, and time spent together doing anything but. To the Wheats: Cheyenne, Daniel, et al., who turned Thursdays into the start of the weekend and quickly fell into the esteemed category of family friends. To Zach, Brian, Dan, Eric, Mike, and Mike, who make home feel like it can be anywhere; and to Sean, the linchpin of the previous list and who at the very beginning, in a hotel lobby, made Colorado feel not quite as

far from home as I feared.

A lot of what I learned as a graduate student came from the dissertations of graduate students before me. As a new student, they occupied some mythical and omniscient role, and I would find these dusty tomes in the lab that seemed to hold all of the answers I was looking for. As I continued, I began to recognize much of the language, references, and experiences that were written down, and see that previous did in fact face challenges that were similar to my own. My work has covered a number of topics, and at times it feels to me to be scattered, but I hope that a future graduate student can use what is here to get their feet on the ground or answer that one sticking, specific problem. Rest assured: you are not an impostor, and what you're doing will be worth it.

DEDICATION

To Uncle Steven with a “V”, Olsen with an “E,”

who taught me that any problem can be fixed.

TABLE OF CONTENTS

LIST OF TABLES

LIST OF FIGURES

Chapter 1. Introduction

1.1 Big Picture

The microwave region of the electromagnetic spectrum is generally defined as between 300 MHz and 300 GHz, or wavelengths of 1 m to 1 mm, lying within the broader characterization of radio frequencies (rf) defined as 100 MHz–1000 GHz. In a practical sense, microwaves have wavelengths on the scale of the elements in a microwave circuit. This means that there is a meaningful phase change across the circuit elements and that analysis occupies a regime between circuit theory and geometrical optics.

Electromagnetic waves at microwave frequencies travel through the atmosphere by line of sight and, relative to higher frequencies, are only weakly attenuated by scattering with things like clouds or foliage. These properties make them natural carriers for over-the-air (OTA) communications and active remote sensing applications, i.e., radar. Applications of radar are diverse and widespread, and OTA communications have unquestionably defined the modern era. The microwave spectrum is also host to a suite of physical phenomena. Transitions between rotational states in oxygen and water vapor emit microwave radiation that is measured by passive sensors called radiometers and used to characterize atmospheric temperature and humidity, sea surface temperature and ice coverage, soil moisture, and more. At a much smaller scale, and applied magnetic field will cause the magnetic moments in a material to precess at frequencies within the microwave regime—this phenomenon is the basis of a rich field of magnetization dynamics with applications in digital data storage, nonlinear research, and spin-based computing. Magnetic data storage in particular has also had a major impact on the modern era, to support the immense and growing amount of data that is produced for research, business, communication, and entertainment.

This dissertation details three microwave experiments that demonstrate the broad applicability of microwave research in physics and engineering within the fields of magnetization dynamics and in passive remote sensing. The current chapter provides an introduction and review of subject matter common between each project. Chapter 2 and Chapter 3 discuss spectroscopic measurements of ferromagnetic resonance (FMR) and an experimental setup for measuring FMR at elevated temperatures. There is a present need for high-temperature FMR to characterize the Gilbert damping constant in materials intended for near-future technologies such as heat-assisted magnetic recording and spin-transfer torque magnetic random-access memory (STT MRAM). The damping constant is critical to characterizing efficiency in these devices because it is correlated to the energy required to flip a magnetic moment—the physical object representing binary bit.

Chapter 4 discusses excitations of magnetic systems called spin waves, or magnons. Spin waves have attractive properties for fundamental physics research and for high-frequency communications. This is due in part to a flexible dispersion relation, which is a function of the magnetic environment. Magnonic crystals are devices with engineered magnetic properties to affect the spin-wave dispersion. The simplest example is a thin film strip with periodic changes in magnetization, which can be realized in a myriad of ways. This structure supports Bragg reflections, which rejects spin waves with particular wavenumbers and functions as a tunable notch filter. The work in Chapter 5 describes the fabrication, simulation, and measurement of a magnonic crystal with a double periodicity that displays a dispersion relation with notable distinctions from singly periodic designs.

Chapter 6 discusses the passive sensing of thermally-emitted radiation, called radiometry, in the Earth's atmosphere. Spaceborne radiometers measure, among other things, the thermal signatures of oxygen and water vapor and are powerful tools for numerical weather prediction, atmospheric research, and climate science. Precise calibration is required for these instruments to separate the small and noiselike signals from the instrument's own thermal profile, and to make meaningful comparisons between different instruments and datasets. These calibrations require targets that approximate a blackbody, a theoretical object that absorbs all incident energy and, according to the conservation of energy, emits a known amount power defined by its physical temperature. Chapter 7 presents the development and characterization of a novel calibration target built from metamaterial absorbers. The metamaterial absorber calibration targets reduce uncertainty by eliminating physical temperature gradients in current state-of-the-art targets, and have size and weight advantages for miniaturized instruments with those constraints, which are becoming increasingly popular for spaceborne applications.

1.2 Electromagnetism

Standard textbooks on microwave engineering and classical electrodynamics are the aptly-titled books by Pozar [1] and Jackson [2], respectively. The sections here are meant to summarize some generally-applicable topics.

1.2.1 Maxwell's Equations

Electromagnetics is described by Maxwell's equations, which are (in differential form):

$$\nabla \cdot \mathbf{D} = \rho, \tag{1.1}$$

$$\nabla \cdot \mathbf{B} = 0, \tag{1.2}$$

$$\nabla \times \mathbf{E} = -\frac{\partial \mathbf{B}}{dt}, \tag{1.3}$$

$$\nabla \times \mathbf{H} = \frac{\partial \mathbf{D}}{dt} + \mathbf{J}. \tag{1.4}$$

Maxwell's equations relate the electric field $\mathbf{E}$ (with units of [V/m]), the magnetic field $\mathbf{H}$ [A/m], and their corresponding flux densities (usually also referred to as fields or inductions) $\mathbf{D}$ [C/m^2] and $\mathbf{B}$ [Wb/m^2] to each other and to the charge density ρ [C/m^3] and current density $\mathbf{J}$ [A/m^2]. The fields and flux densities are related by the electric permittivity ε [F/m] and magnetic permeability μ [H/m] of the material. In vacuum these are the real-valued constants

$$\varepsilon_0 = 8.854 \times 10^{-12}, \tag{1.5}$$

$$\mu_0 = 4\pi \times 10^{-7}. \tag{1.6}$$

In materials, electric or magnetic moments align with an applied field to create a polarization, P. In linear media, and using the magnetic fields as an example,

$$\mathbf{B} = \mu_0(\mathbf{H} + \mathbf{P}) = \mu_0(\mathbf{H} + \chi\mathbf{H}) \tag{1.7}$$

where χ is the complex susceptibility. Letting $\mu_0(1+\chi) = \mu$ leads to the constitutive relations

$$\mathbf{B} = \mu\mathbf{H}, \tag{1.8}$$

$$\mathbf{D} = \varepsilon\mathbf{E}. \tag{1.9}$$

The relation between the electric fields are handled in an identical manner.

Imaginary components of μ and ε represent losses. Losses are due to damping mechanisms on the vibrating dipole moments and, in electric conductors, due to resistive losses according to Ohm's law

$$\mathbf{J} = \sigma\mathbf{E}, \tag{1.10}$$

which describes the conduction current density due to the material conductivity, σ. Microwave electronic components are often characterized by a real relative permittivity, ε_r, also called the dielectric constant, and a factor called the loss tangent, $\tan\delta$. Loss can be introduced to a lossless model by then letting real $\varepsilon \to \varepsilon_0\varepsilon_r(1 - i\tan\delta)$.

It is common to consider fields that are at steady-state and have a harmonic, or sinusoidal, time dependence. For example,

$$\mathbf{E}(x, y, z, t) = \mathbf{E}(x, y, z)e^{i(\omega t+\phi)}. \tag{1.11}$$

Oftentimes, the harmonic term, $e^{i\omega t}$, is suppressed.

1.2.2 Propagation of Electromagnetic Waves

Propagation of an electromagnetic wave through "free space" refers to travel through a perfect vacuum: an empty, isotropic, and homogenous region with $\mu = \mu_0$ and $\varepsilon = \varepsilon_0$. Air is approximately free space. (1.3) and (1.4) become

$$\nabla \times \mathbf{E} = -i\omega\mu_0\mathbf{H}, \tag{1.12}$$

$$\nabla \times \mathbf{H} = i\omega\varepsilon_0\mathbf{E}, \tag{1.13}$$

so either **E** or **H** can be determined. Choosing **E**, take the curl of (1.12) and substitute (1.13):

$$\nabla \times \nabla \times \mathbf{E} = -i\omega\mu_0 \left(i\omega\varepsilon_0 \mathbf{E}\right) = \omega^2 \mu_0 \varepsilon_0 \mathbf{E}, \tag{1.14}$$

then use the vector identity $\nabla \times \nabla \times \mathbf{E} = \nabla \left(\nabla \cdot \mathbf{E}\right) - \nabla^2 \mathbf{E}$ to yield

$$\nabla^2 \mathbf{E} + \omega^2 \mu_0 \varepsilon_0 \mathbf{E} = 0. \tag{1.15}$$

The result for **H** is identical. This result is a Helmholtz equation—the wave equation—with wave number $k = \omega\sqrt{\mu_0\varepsilon_0}$ [m^{-1}].

The simplest case for (1.15) is a uniform field like $\mathbf{E} = E_x \hat{x}$, which has the solution

$$E_x(z) = E^+ e^{-ikz} + E^- e^{ikz}. \tag{1.16}$$

This shows a wave that propagates in $\hat{z}$ and in $\hat{z}$. To determine the result for **H**, take the curl of **E** above:

$$\nabla \times \mathbf{E} = -i\omega\mu_0 H = -\hat{y}\frac{dE_x}{dz}, \tag{1.17}$$

$$\omega\mu_0 H_y = kE_x, \tag{1.18}$$

$$H_y = \frac{1}{\eta_0} E_x, \tag{1.19}$$

where

$$\eta = \frac{\omega\mu}{k} = \sqrt{\frac{\mu}{\varepsilon}} \tag{1.20}$$

is the intrinsic wave impedance of the medium, which relates the amplitudes of **E** and **H** and has units of impedance. In free space, $\eta_0 = 376.73\,\Omega$.

The phase velocity, v_p, of the wave traveling in $\hat{z}$ is taken from a phase-constant point, and it is shown that $v_p = 2.998 \times 10^8$ m/s $\equiv c$, the speed of light.

$$v_p = \frac{dz}{dt} = \frac{d}{dt}\left(\frac{\omega t - kz}{k}\right) = \frac{\omega}{k} = \frac{1}{\sqrt{\mu_0\varepsilon_0}} = c \tag{1.21}$$

1.2.3 Selected Microwave Components

Transmission Lines

Transmission lines, such as rigid waveguides, coaxial cables, strip lines, and microstrip lines, carry electromagnetic waves. It is common to see microstrip lines as printed-circuit boards (PCBs), which allows for flexible designs using lithographic fabrication techniques. Coaxial cables, often with SubMiniature version A (SMA) connections, are very common because they are cheap, flexible, and support frequencies from DC to 18–26 GHz. Similar-appearing but varyingly-compatible connectors exist that enable higher frequencies. Rigid waveguides are a straightforward implementation of a transmission line—essentially just conductive pipe. They can be expensive, but they can carry high power with minimal loss. They can support frequencies up to hundreds of gigahertz, but the actual bandwidth supported by a particular waveguide is a function of its dimensions. Labels may use the lettered-band designations—e.g., X-band, V-band, Ku-band—or WR numbers—e.g., WR-5, WR-6, WR-12. The number refers to the inner dimension and, intuitively, larger waveguide dimensions support larger wavelengths (lower frequencies) and vice versa.

For a wave propagating in $\hat{z}$, modes get classified as transverse electric (TE) if $E_z = 0$, transverse magnetic (TM) if $H_z = 0$, and as transverse electromagnetic (TEM) if $E_z = H_z = 0$. The wave through a transmission line propagates as currents in the conducting walls that support standing waves, and these standing waves determine the mode number. Contained in two-dimensions, there are thus two values, e.g., TE_{01}. Modes propagate above their cutoff frequency, f_c, determined by the line geometry, and the lowest-frequency mode is called the dominant mode.

Resonant Cavities

A resonant cavity contains the energy of a guided wave. For the measurement of a sample loaded in the cavity, a cavity can provide a significantly improved signal-to-noise ratio (SNR). Resonator circuits are modeled as a series or parallel resistor-inductor-capacitor (RLC) circuit. The inductor and capacitor store magnetic and electric energy, W_m and W_e. At resonance, these are equal, defining the resonant frequency as

$$\omega_0 = \frac{1}{\sqrt{LC}}. \tag{1.22}$$

The resistance, R, represents the power lost by the resonator, be it ohmic, dielectic, or radiative. The ratio of energy stored to energy lost per second describes the quantity Q, oftentimes referred to as the Q-factor or quality factor.[1] Q is the figure of merit for resonant systems and a higher Q represents a a more effective resonator.

$$Q = \omega_0 \cdot \frac{\text{energy stored in the resonant circuit}}{\text{time-averaged power loss}} \tag{1.23}$$

When a resonant circuit is connected to an external circuit, and when a sample is included, Q is reduced and called loaded. The unloaded Q_0 represents the isolated resonator.

The resonant frequency and Q of a resonator can be found by measuring the reflected voltage against the frequency, as shown in Figure 1.1. The point of minimum voltage, where the most energy is absorbed, is the resonant frequency, f_{res}. It can be shown that

$$Q = \frac{f_{res}}{\Delta f}, \tag{1.24}$$

where Δf is the half-power bandwidth. This is valid for voltage when the signal is determined by a square-law detector.

A microwave resonator can be built from an open- or short-circuited line, but a closed section of waveguide, a cavity, typically has much higher Q. Similar to transmission lines, standing waves between the cavity walls describe the cavity mode. The experiments in Chapter 3 take advantage of high-Q cylindrical cavities operating in the TE_{011} mode. This mode, illustrated in Figure 1.2 maximizes the magnetic field at the center of the cavity, where the sample was located. Figure 1.3 is a photo of one of the cavities used in this experiment. It is made of high-purity copper and couples to a waveguide via a small hole at the top called an iris. The hole in the cap is used to insert a sample holder.

Antennas

An antenna is a transducer that converts a guided wave into unguided free space, or vice versa. Microwave antennas are, of course, essential for wireless communications, and antenna design is

[1] The word "quality" was applied after-the-fact to the variable Q, which was chosen simply because it was available [3].

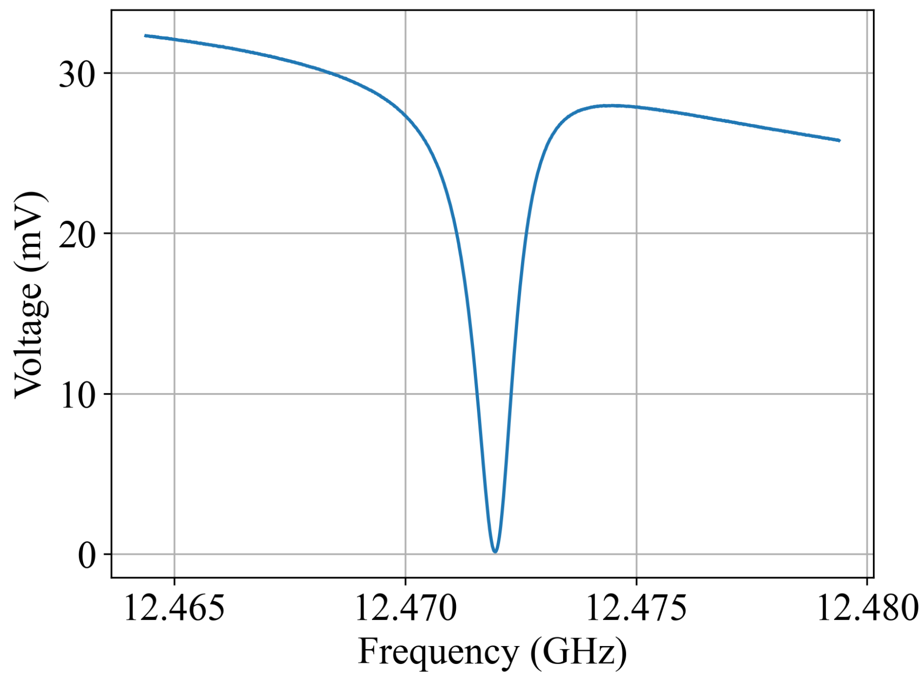

Figure 1.1: Measured resonance of an unloaded cylindrical microwave cavity.

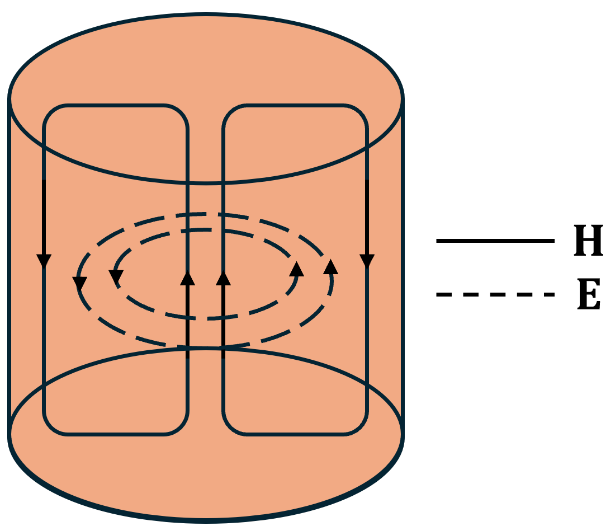

Figure 1.2: Illustration of the TE_{011} mode in a cylindrical microwave cavity. The magnetic field strength is maximum at the center.

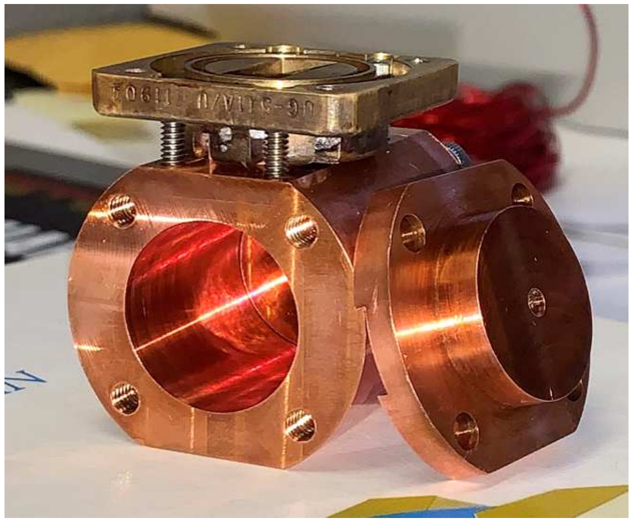

Figure 1.3: A cylindrical microwave resonant cavity open at one end. The cavity couples to a Ku-band rectangular waveguide.

fittingly an expansive and growing field—the IEEE Antennas and Propagation society includes over 16,000 members per the society president's 2026 address.

Much of the theory of antennas is simplified when the antenna is within the far-field region. This is when spherical wavefronts from a source are able to be considered planar at the receiver. The far-field distance, R, is

$$R = \frac{2D^2}{\lambda}, \tag{1.25}$$

where D is the largest dimension of the antenna and $\lambda = c/f$ is the wavelength. The far-field condition is generally desired and assumed.

Most antennas are reciprocal, meaning that an antenna has the same characteristics whether it is acting as a transmitter or as a receiver. An antenna is described by its radiation pattern, which represents how the energy is distributed into (or received from) space. The antenna pattern function is

$$F(\theta, \phi) = \left.\frac{S(R, \theta, \phi)}{S_{max}}\right|_R, \tag{1.26}$$

where S is the time-averaged power density,

$$\mathbf{S} = \frac{1}{2}\mathrm{Re}\left(\mathbf{E} \times \mathbf{H}^*\right), \tag{1.27}$$

and the evaluation is at some fixed distance R. $F(\theta, \phi)$ is normalized to the maximum value. The total radiated power, P_{rad}, is calculated by integrating F over a spherical surface:

$$P_{rad} = R^2 S_{max} \iint_{4\pi} F(\theta, \phi) d\Omega, \tag{1.28}$$

where $d\Omega = \sin\theta d\theta d\phi$ is an element of solid angle.

Figure 1.4 shows a typical style of plotting antenna patterns. The plot is polar for θ with $\phi = 0$. A radiation plot would typically mark the peak of the main lobe as 0 dB. The figure shows a directive antenna with multiple local maximas called lobes. The mainlobe is the desired direction of propagation. Sidelobes and backlobes are generally undesirable: for a transmitting antenna they represent energy directed away from the target, and for a receiving antenna they represent interference contributions. Relevant angular regions include the full-width at half-maximum, $\beta_{1/2}$, called the 3 dB or half-power beamwidth, and the null beamwidth, β_{null}, marking the minima that separate the mainlobe from the first sidelobes.

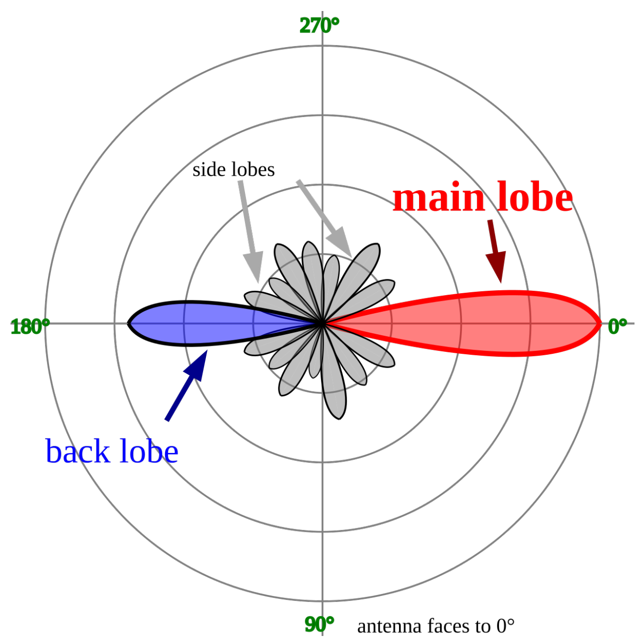

Figure 1.4: A typical polar radiation plot for a directive antenna, from Wikipedia. The mainlobe is the desired direction of propagation; sidelobes and backlobes are generally undesirable.

The ratio of F_{max} (= 1, by definition) to the average in space, F_{avg}, defines the directivity, D. For a pattern with a single mainlobe centered on $\hat{z}$,

$$D \approx \frac{4\pi}{\beta_x \beta_y}, \tag{1.29}$$

where β_x and β_y are half-power beamwidths in x and y. A greater directivity represents a narrower mainlobe. Directivity can be directly related to antenna gain, G. For a lossless antenna, analysis shows by equivalence that $G = D$. Ohmic losses are included by the radiation efficiency, ξ, defined as

$$\xi = \frac{\text{Power radiated}}{\text{Power supplied}}, \tag{1.30}$$

and the gain is simply $G = \xi D$.

1.2.4 Aside: On Units

In Magnetism

Magnetic quantities have historically favored a system of units based on the centimeter-gram-second systems of units, CGS, such as the Gaussian system or the EMU (electromagnetic units) system, based on—as with any system, ultimately—convenience and convention. Today, many publications require (or strongly suggest) that units are standardized and presented using the international system of units, the SI,[2]. This transition hasn't been without some confusion for magnetics researchers (author included)—Jackson includes a ten-page appendix on the topic in his textbook [2], and Goldfarb at the National Institute of Standards and Technology (NIST) has most recently published on the topic in 2021 [4], following the 2019 revision of the SI [5]. This revisison fixes the values of seven fundamental constants that are used to define seven base units. The magnetic permeability, μ_0, which was previously a fixed constant, is now determined using the speed of light in vacuum, c, which is a fixed fundamental constant and the fine-struture constant, α, which is measured in experiment. The relative uncertainties in α, μ_0, and ε_0 are equivalent.

Within the scope of this dissertation, the relavent differences are summarized by the constitutive relation, (1.8), in each system:

$$\text{SI: } B = \mu_0(H + M), \tag{1.31}$$

$$\text{Gaussian: } B = H + 4\pi M. \tag{1.32}$$

In SI units, H and M have the same unit of amperes per meter [$\mathrm{A\,m^{-1}}$], and B is in units of

[2]from French *système international d'unités*

teslas [T]. In Gaussian units, B and H are in gauss [G] and oersted [Oe], respectively, which are equivalent. M on its own doesn't have a named unit,[3] but $4\pi M$ is in G. In both systems, $\chi = M/H$.

Jackson and Goldfarb both present tables for converting quantities between systems. It is useful to remember that 10 G = 1 mT (relevant for applied fields) and that 4π Oe = 1 kA m^{-1} (relevant for magnetizations). Derivations using SI should include a factor of μ_0, which is typically common to each term; and Gaussian derivations should let $M \to 4\pi M$.

In Microwave Engineering

Microwave engineering typically works in a base-10 logarithmic scale of "units" called decibels [dB].[4] For some linear quantity, q, its value in dB is

$$q[\mathrm{dB}] = 10 \log q, \tag{1.33}$$

and in the other direction,

$$q = 10^{q[\mathrm{dB}]/10}. \tag{1.34}$$

Decibels are useful because logarithmic addition represents linear multiplication. A change of +/- 10 dB is a factor of 10 above/below the initial quantity, and a change of +/- 3 dB is approximately double/half of the initial quantity. It is standard for instruments to present power in units of decibel-milliwatts [dBm], which defines 0 dBm as 1 mW. Then, gains and losses can be simply calculated by adding and subtracting in dB.

[3] "emu" may be used, which stands for "electromagnetic unit."

[4] Mathematics sometimes prefer logarithms of base-e, and these are called nepers. 1 neper = 8.686 dB.

Chapter 2. Ferromagnetic Resonance

2.1 Magnetism in Materials

The orbital angular momentum of a flow of electrons, i.e., a current-carrying loop of wire, creates a magnetic moment according to a right-hand rule. Each electron has a purely quantum mechanical intrinsic contribution to its angular momentum called spin, $\mathbf{s}$, that likewise yields an intrinsic magnetic moment, $\mathbf{m}$. The magnetic properties of a material arise almost entirely from contributions of the spin magnetic moments from unpaired electrons. In ferromagnetic materials, the magnetic moments have order: a net alignment that summate to a spontaneous macroscopic magnetization, $\mathbf{M}_0$. The ordering is opposed by thermal energy up to the Curie temperature, T_C, at which the moments are fully randomized and $M_0 = 0$.

In the presence of an applied magnetic field, $\mathbf{H}$,

$$\mathbf{M} = \mathbf{M}_0 + \chi \cdot \mathbf{H}, \tag{2.1}$$

where $\mathbf{M}$ is the magnetization and χ is the susceptibility tensor. It will be assumed in general that the material is isotropic, such that χ is a scalar. Non-magnetic materials have $\mathbf{M}_0 = 0$, and those with $\chi > 0$ are called paramagnetic. Paramagnetism is seen in materials that have unpaired electrons but no spontaneous magnetic ordering. Magnetic materials at temperatures above T_C will exhibit a paramagnetic response. Diamagnetic materials have no unpaired electrons, $\mathbf{M}_0 = 0$ and $\chi < 0$. In diamagnets, eddy currents induced by $\mathbf{H}$ create an opposing field. Materials with magnetic ordering are characterized by the relative strength and orientation of the moments as ferri-, ferro-, or antiferromagnetic. Figure 2.1 presents a flowchart to determine these classifications.

A measurement of M against H is a common method to characterize the internal magnetic fields of materials. Ferromagnets demonstrate a nonlinear relationship called hysteresis, whereby changes in M depend on the state of M. Figure 2.2 illustrates an example of a hysteresis curve (or loop). A demagnetized sample is quickly magnetized from the origin to its saturation magnetization (or saturation induction), M_s, at which point the individial moments have become completely aligned. This occurs at the saturating field strength, H_s. Reducing the applied field strength reduces M

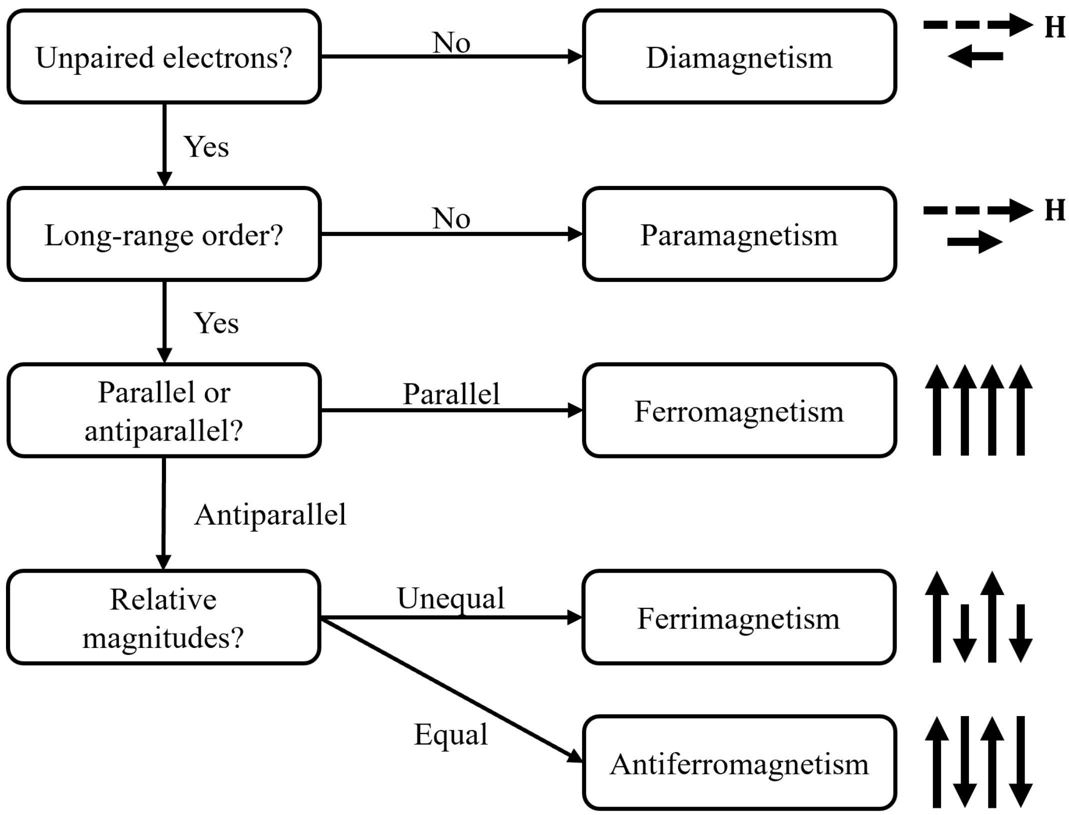

Figure 2.1: Flow chart for magnetically characterizing a material. Solid arrows to the right of each type of magnetism represent magnetic moments. The dashed arrows next to cells labeled "diamagnetism" and "paramagnetism" represent an externally-applied magnetic field, **H**.

along the indicated path to the remanence value, M_r, when no field is applied. With the applied field in the opposite direction, the sample magnetization changes direction to align with H at the coercivity field strength, H_c, and eventually reaches M_s in the new direction. The curve is symmetrical from this point. The area within the hysteresis curve corresponds to the energy dissipated in the switching process.

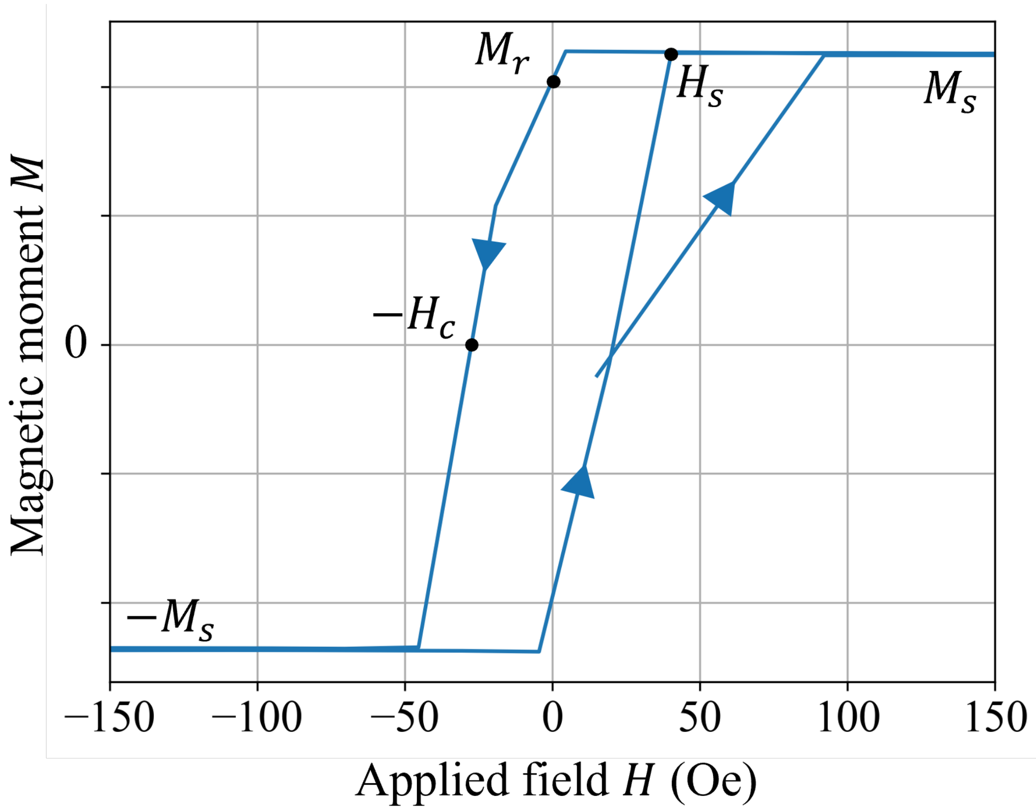

Figure 2.2: A hysteresis curve measured from a yttrium iron garnet (YIG) sample. The paramagnetic response of the substrate (gadolinium gallium garnet) has been removed. The saturation magnetization, M_s, remanence magnetization, M_r, coercivity field strength, H_c, and saturating field strength, H_s, are marked. This particular measurement used relatively large steps in H, limiting resolution.

Hysteresis loops are often measured using a vibrating sample magnetometer (VSM). A typical VSM configuration is shown in Figure 2.3. The sample (star) is positioned between magnetic pole pieces (gray trapezoids) producing a field, $H\hat{z}$. It is affixed to a holder that oscillates in $\hat{x}$. The oscillation is typically generated by a piezoelectric material at a known rate, dx/dt. The oscillating sample generates a voltage difference, U, in sensing coils (red rectangles) according to (1.3), such that

$$U = \frac{d\Phi}{dt} = \frac{dx}{dt}\frac{d\Phi}{dx}, \tag{2.2}$$

where Φ is the magnetic flux through the sensing coils. $d\Phi/dx$ is proportional to the sample moment and the cross-sectional area of the sensing coils.

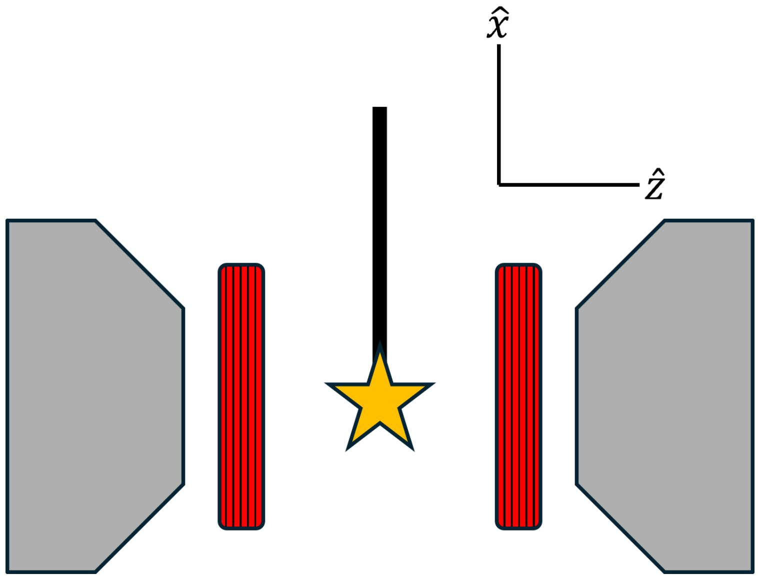

Figure 2.3: Basic diagram of a vibrating sample magnetometer. A magnetic field is applied between the pole pieces (grey trapezoids) in $\hat{z}$. The sample (star) oscillates in $\hat{x}$, and the change in magnetic flux is measured by the sensing coils (red, striped).

2.1.1 Exchange Interaction

The angular momentum of an atom or ion in its ground state can be found using a simple set of criteria called Hund's rules, and this predicts the paramagnetic or diamagnetic response of that atom or ion. The prediction generally holds when scaled up to solids, but is unable to predict magnetism from spontaneous ordering. A magnetic moment in a solid will exist due primarily to electrostatic correlations between spin sites. Ashcroft & Mermin [6] and Stancil [7] both discuss the difficulty of modeling this problem, particularly in metals, and provide derivations of the two-electron hydrogen atom.

When the wavefunction distributions of the electrons overlap, the expectation value for the energy of the state includes a so-called exchange integral, which describes the probability of a transition where the (indistinguishable) electrons swap positions. This is called the exchange interaction. It may be direct between spin sites or mediated between sites by other mechanisms. Further analysis that considers the orientation of electron spins yields the spin Hamiltonian

$$H = -2J\mathbf{S_1} \cdot \mathbf{S_2}, \tag{2.3}$$

where $\mathbf{S}_1$ and $\mathbf{S}_2$ are the spin operators for each site and J is the exchange constant and proportional to the difference in energies of the electron singlet and triplet states. $J > 0$ has minimized energy with a parallel alignment (a ferromagnet), and $J < 0$ with an anti-parallel alignment (an antiferromagnet).[5] A scaled-up version of this Hamiltonian can be constructed by taking the summation of all ion pairs:

$$H = -2\sum_{ij} J_{ij}\mathbf{S}_i \cdot \mathbf{S}_j. \tag{2.4}$$

This is the Heisenberg Hamiltonian. It is assumed, at a minimum, that the system has wavefunctions that overlap only slightly (e.g., it is an insulator) and that orbital contributions to the total angular momentum are small.

The leap from two coupled spins to N coupled spins in two or three dimensions is quite generous; however, (2.4) does well to describe observed phenomena. For example, the exchange energy along a two-dimensional chain of spin sites can be interpreted as an excitation with varying spin orientation from site to site. This is an exchange spin wave, illustrated in Figure 2.4.

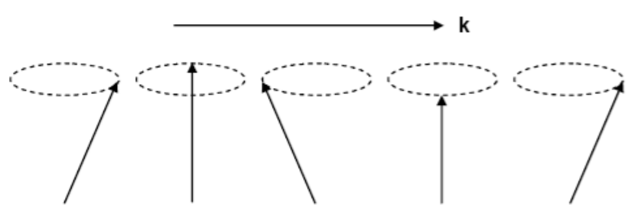

Figure 2.4: Illustration of a spin wave, from Stancil [7]. The wave is described by the relative orientation of magnetic dipole moments at spin sites and has wavenumber k.

2.1.2 Magnetic Anisotropy

Magnetic anisotropy refers to an energy bias that defines a preferred orientation for a material's magnetization. This can be the result of crystal structure (called magnetocrystalline anisotropy),

[5] The two-electron hydrogen atom, for the record, is antiferromagnetic.

sample shape, tension, or exchange between ferro- and antiferro- magnetic layers. Most relevant to this dissertation is magnetocrystalline uniaxial anisotropy, which occurs naturally in hexagonal crystals and can be present in thin films as a result of their growth conditions. Uniaxial anistropy is characterized by a single axis with a minimized (called an easy axis) or maximized (called a hard axis) energy bias.

The effects of anisotropy can be modeled as an internal field called the effective anisotropy field, $\mathbf{H}_k$. To first order and when the sample is magnetized along its easy axis,

$$H_k = \frac{2K}{\mu_0 M_s}, \tag{2.5}$$

where K is the anisotropy constant and M_s is the saturation magnetization of the material.

Anisotropy is often a desirable property for applications, because high $\mathbf{H}_k$ can eliminate the need for an externally-applied biasing field and is stable against perturbations. For example, perpendicular magnetic recording (PMR) is a technology used in magnetic data storage that takes advantage of materials with high out-of-plane anisotropy to dramatically reduce the effect of nearest-neighbor interactions. This allowed for an order-of-magnitude increase in storage density in those devices.

2.1.3 Demagnetization

Maxwell's equation (1.2) that describes "no magnetic monopoles" requires continuity in $\mathbf{H}$ at either side of an interface. Consider a field H_0 applied normal to a plate with magnetization M_s. Continuity requires that

$$H_0 = M_s + H, \tag{2.6}$$

where H is the effective internal field of the plate. H is smaller than H_0, and this phenomenon is called demagnetization. Demagnetization depends on sample geometry and orientation with respect to the applied field, and is modeled as

$$\mathbf{H} = \mathbf{H}_0 - N_{x,y,z}\mathbf{M}. \tag{2.7}$$

Table 2.1: Demagnetization factors for common geometries. The direction of the applied field is chosen as $\hat{z}$.

Shape (field direction)	$\mathbf{N_x}$	$\mathbf{N_y}$	$\mathbf{N_z}$
Sphere	1/3	1/3	1/3
Cylinder (major axis)	1/2	1/2	0
Cylinder (minor axis)	1/2	0	1/2
Thin film (out-of-plane)	0	0	1
Thin film (in-plane)	1	0	0

$N_{x,y,z}$ are the demagnetization factors, which are defined such that $N_x + N_y + N_z = 1$. Table 2.1 collects values of N for common sample geometries with H_0 in $\hat{z}$.

2.2 Precessional Motion

The electron spin, $\mathbf{s}$, and the corresponding magnetic moment, $\mathbf{m}$, are directly related by a constant called the gyromagnetic ratio, γ:

$$\mathbf{m} = \gamma \mathbf{s}. \tag{2.8}$$

Classically analyzing an electron in a circular orbit shows that $\gamma = -e/2m_e$, where $-e$ is the electron charge and m_e is its mass. The quantum mechanical result is equal to this times a factor (the "g-factor") of two:

$$\gamma = \frac{-e}{m_e}. \tag{2.9}$$

For $|\mathbf{s}| = \hbar/2$, the magnitude $|\mathbf{m}|$ is defined as one Bohr magneton, $\mu_B = e\hbar/2m_e$. The negative charge of the electron has the effect that γ is negative and that $\mathbf{m}$ and $\mathbf{s}$ are anti-aligned. It is generally preferred to refer to the magnitude, $|\gamma|$, for explicitness.

$|\gamma|$ has units of radians per tesla. As a linear frequency,

$$|\gamma|/2\pi = 28\,\mathrm{GHz}\,\mathrm{T}^{-1}. \tag{2.10}$$

It is not uncommon for the factor of 2π to be implied and omitted. This value provides a practical order of magnitude for magnetization dynamics. For example, a field strength of 350 mT corresponds to a frequency of nearly 10 GHz, within the microwave X-band. These values are very accessible for experiments.

Since $|\gamma|$ is typically multiplied by a field, it is often convenient to refer to their product, which is a frequency:

$$\omega = |\gamma|\,\mathbf{B} = |\gamma|\,\mu\mathbf{H}. \tag{2.11}$$

I refer to this as the "field-frequency substitution." In SI units, this includes a common μ term as well; occasionally, μ is combined into $|\gamma|$ and omitted.

For a bound particle, there is an additional magnetic moment associated with the orbital angular momentum; however, the macroscopic moment of most materials is almost entirely due to spin contributions from unpaired electrons. This is due to the interaction between spin and orbital angular momenta, called spin-orbit coupling, typically being very weak. As a result, spin contributions have more weight [7] and, in a lattice, electronic interactions from neighboring ions serve to eliminate the orbital angular momentum entirely, and it is referred to as "quenched." Materials with strong spin-orbit coupling have potential applications in spintronics by providing electrical control over spin orientations [8].

In the presence of an external magnetic field, $\mathbf{B} = \mu_0\mathbf{H}$, the magnetic dipole moment, $\mathbf{m}$, of the electron will experience a torque

$$\tau = \frac{d\mathbf{s}}{dt} = \mathbf{m} \times \mathbf{B} = \mu_0\mathbf{m} \times \mathbf{H}. \tag{2.12}$$

The cross product shows that the direction of this torque will drive the tip of $\mathbf{s}$ to precess around $\mathbf{B}$. By substituing $\mathbf{s}$ with (2.8), the result is

$$\frac{d\mathbf{m}}{dt} = -\mu_0\,|\gamma|\,\mathbf{m} \times \mathbf{H}. \tag{2.13}$$

This is the Landau-Lifshitz equation of motion, which is valid for a single moment or collective magnetization, $\mathbf{M}$. The Landau-Lifshitz equation is the fundamental equation for magnetization dynamics.

(2.13) can be solved to determine the frequency of precession. Consider an field $H_0\hat{z}$ applied to a material, and a magnetization $\mathbf{M} = (m_x, m_y, M_s)$. Assume a small angle of precession; therefore, second-order products m_x and m_y are zero and M_s is the saturation value of the material. m_x and m_y are harmonic terms with (omitted) factors of $\exp(i\omega t)$. The total field includes a demagnetizing

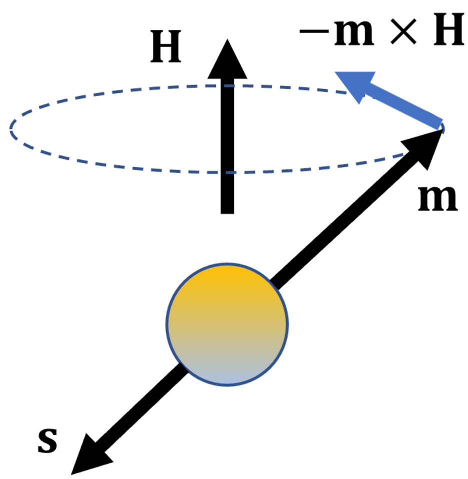

Figure 2.5: Precessional motion of an electron.

field, H_d, so $\mathbf{H} = (-N_x m_x, -N_y m_y, H_0 - N_z M_s)$.

The vector components of (2.13) are

$$\frac{d\mathbf{M}}{dt} = (i\omega m_x, i\omega m_y, 0)\,, \tag{2.14}$$

$$\mathbf{M} \times \mathbf{H} = (H_y m_y, -H_x m_x, 0)\,, \tag{2.15}$$

where $H_x = H_0 + M_s(N_x - N_z)$ and $H_y = H_0 + M_s(N_y - N_z)$ are referred to as the stiffness fields. Using the field-frequency substitution to further collect terms, (2.13) becomes

$$\begin{pmatrix} i\omega & -\omega_y \\ \omega_x & i\omega \end{pmatrix} \begin{pmatrix} m_x \\ m_y \end{pmatrix} = 0. \tag{2.16}$$

Solutions require the determinant of the 2×2 matrix to be zero, therefore

$$\omega = \sqrt{\omega_x \omega_y}. \tag{2.17}$$

Returning to fields,

$$\omega = |\gamma|\,\mu_0 \sqrt{[H_0 + (N_x - N_z)M_s]\,[H_0 + (N_y - N_z)M_s]}. \tag{2.18}$$

This is the Kittel equation. For an isolated spin, or for a spherical sample (using the values in Table 2.1), this reduces to $\omega = |\gamma| \mu_0 H_0$. This frequency is called the Larmor frequency. For a thin film, we see that

$$\text{in plane: } \omega = |\gamma| \mu_0 \sqrt{H_0(H_0 + M_s)}, \tag{2.19}$$

$$\text{out of plane: } \omega = |\gamma| \mu_0 (H_0 - M_s). \tag{2.20}$$

2.3 Magnetic Damping

2.3.1 Magnetic Torque Equation

Lev Landau and Evgeny Lifshitz included a term to describe the relaxation of precessional motion, referred to as damping. In 1955, Thomas Gilbert modified the equation to better explain damping observed in thin ferromagnetic sheets [9], and the Gilbert form is most commonly used today (though for small damping the two forms are equivalent). The Landau-Lifshitz-Gilbert (LLG) equation of motion is

$$\frac{d\mathbf{m}}{dt} = -\mu_0 |\gamma| \mathbf{m} \times \mathbf{H} + \frac{\alpha}{M_s} \mathbf{m} \times \frac{d\mathbf{m}}{dt}. \tag{2.21}$$

The Gilbert damping constant, α, is a unitless term that describes the rate of damping.[6] The LLG equation of motion accurately captures damping—which may be the sum effect of multiple processes—in a majority of cases.

Damping processes in magnetic materials are categorized as being either intrisic or extrinsic. Intrinsic damping processes are independent of the material and unavoidable. This includes damping due to eddy currents, spin-orbit coupling, and phonon and electron scattering. Extrinsic damping processes are associated with the sample structure, and could theoretically be eliminated. These processes include two-magnon scattering, whereby interaction with a material imperfection yields two degenerate modes, and spin pumping, whereby spin current in a magnetic layer of material is transfered to a neighboring nonmagnetic layer [10]. Ultimately, all energy is transferred to the crystal lattice as heat, either by direct means or via intermediary spin-wave modes.

[6] $1/\alpha$ is proportional to the number of precessions that occur during relaxation.

2.3.2 A Derivation of the Damping Constant

One method for deriving α begins from the lossless equation of motion, (2.13), and is similar to the derivation of the Kittel equation, (2.18). Here, demagnetization is not considered and a small rf magnetic field perpendicular to H_0 is used to drive precession.

$$
\begin{aligned}
\mathbf{H} &= (h_x, h_y, H_0)\,, \\
\mathbf{M} &= (m_x, m_y, M_s)\,, \\
\frac{d\mathbf{M}}{dt} &= (i\omega m_x, i\omega m_y, 0)\,, \\
\mathbf{M} \times \mathbf{H} &= (m_y H_0 - h_y M_s, M_s h_x - H_0 m_x, 0)\,.
\end{aligned}
$$

Each lowercase variable is small such that their squares go to zero and has an implied harmonic time dependence, $\exp(i\omega t)$. The Landau-Lifschitz equation becomes

$$
i\omega \begin{pmatrix} m_x \\ m_y \end{pmatrix} = \begin{pmatrix} \omega_M h_x - \omega_0 m_y \\ \omega_0 m_x - \omega_M h_y \end{pmatrix}, \tag{2.22}
$$

where we have used the field-frequency substitution for $\omega_0 = \mu_0 |\gamma| H_0$ and $\omega_M = \mu_0 |\gamma| M_s$. This equation shows the linear relationships between $\mathbf{M}$ and $\mathbf{H}$, which can be solved to determine the susceptibility tensor, χ, that relates the two as $\mathbf{M} = \chi \mathbf{H}$. The result is

$$
\chi = \frac{1}{\omega_0^2 - \omega^2} \begin{pmatrix} \omega_0 \omega_M & i\omega_M \omega \\ -i\omega_M \omega & \omega_0 \omega_M \end{pmatrix}. \tag{2.23}
$$

which shows a resonant condition at $\omega = \omega_0$ for all terms. The resonance is handled by allowing the resonant frequency to be complex and introducing a loss factor, α:

$$
\omega_0 \rightarrow \omega_0 + i\alpha\omega. \tag{2.24}
$$

Substituting this into Equation 2.23 creates complex components such that

$$\chi \rightarrow \frac{1}{D'} \begin{pmatrix} \chi_{11} = \chi'_{11} - i\chi''_{11} & \chi_{12} = \chi''_{12} + i\chi'_{12} \\ \chi_{21} = -\chi_{12} & \chi_{22} = \chi_{11} \end{pmatrix}. \tag{2.25}$$

After a bit of algebra, the results are:

$$D' = \left[\omega_0^2 - \omega^2\left(1+\alpha^2\right)\right]^2 + \left(2\alpha\omega_0\omega\right)^2, \tag{2.26}$$

$$\chi'_{11} = \omega_0\omega_M\left[\omega_0^2 - \omega^2\left(1+\alpha^2\right)\right], \tag{2.27}$$

$$\chi''_{11} = \alpha\omega_M\omega\left[\omega_0^2 + \omega^2\left(1+\alpha^2\right)\right], \tag{2.28}$$

$$\chi'_{12} = \omega_M\omega\left[\omega_0^2 - \omega^2\left(1+\alpha^2\right)\right], \tag{2.29}$$

$$\chi''_{12} = 2\omega_0\omega_M\omega^2\alpha. \tag{2.30}$$

The double-primed terms are seen to be a Lorentz (or Cauchy) distribution. Plots of χ are shown in Figure 2.6. Materials that are considered for their damping values often have $\alpha \ll 1$, so $1+\alpha^2$ is taken to be 1.

In practice, the applied ac field is often in one dimension, $\hat{x}$ or $\hat{y}$, suppressing the mixing terms. The losses in the sample are defined by χ'', and related to the linewidth ΔH of the response. For a fixed frequency ω and a swept field ω_0 (recall that $\omega_0 = \mu_0\left|\gamma\right|H_0$), and using the small α approximation above, the maximum occurs when $\omega_0 = \omega$:

$$\chi'' = \frac{\alpha\omega_M\omega\left(\omega_0^2+\omega^2\right)}{\left(\omega_0^2-\omega^2\right)^2 + \left(2\alpha\omega_0\omega\right)^2}, \tag{2.31}$$

$$\omega_0 = \omega \rightarrow \frac{\omega_M}{2\alpha\omega}. \tag{2.32}$$

Next solve for the half-maximum value at $\omega_0 = \omega_{02}$:

$$\frac{\omega_M}{4\alpha\omega} = \frac{\alpha\omega_M\omega\left(\omega_{02}^2+\omega^2\right)}{\left(\omega_{02}^2-\omega^2\right)^2 + \left(2\alpha\omega_{02}\omega\right)^2}, \tag{2.33}$$

$$\omega_{02} = \omega\sqrt{1+2\alpha} \approx \omega\left(1+\alpha\right). \tag{2.34}$$

The final step again takes advantage of the approximation using small α. The linewidth ΔH is then

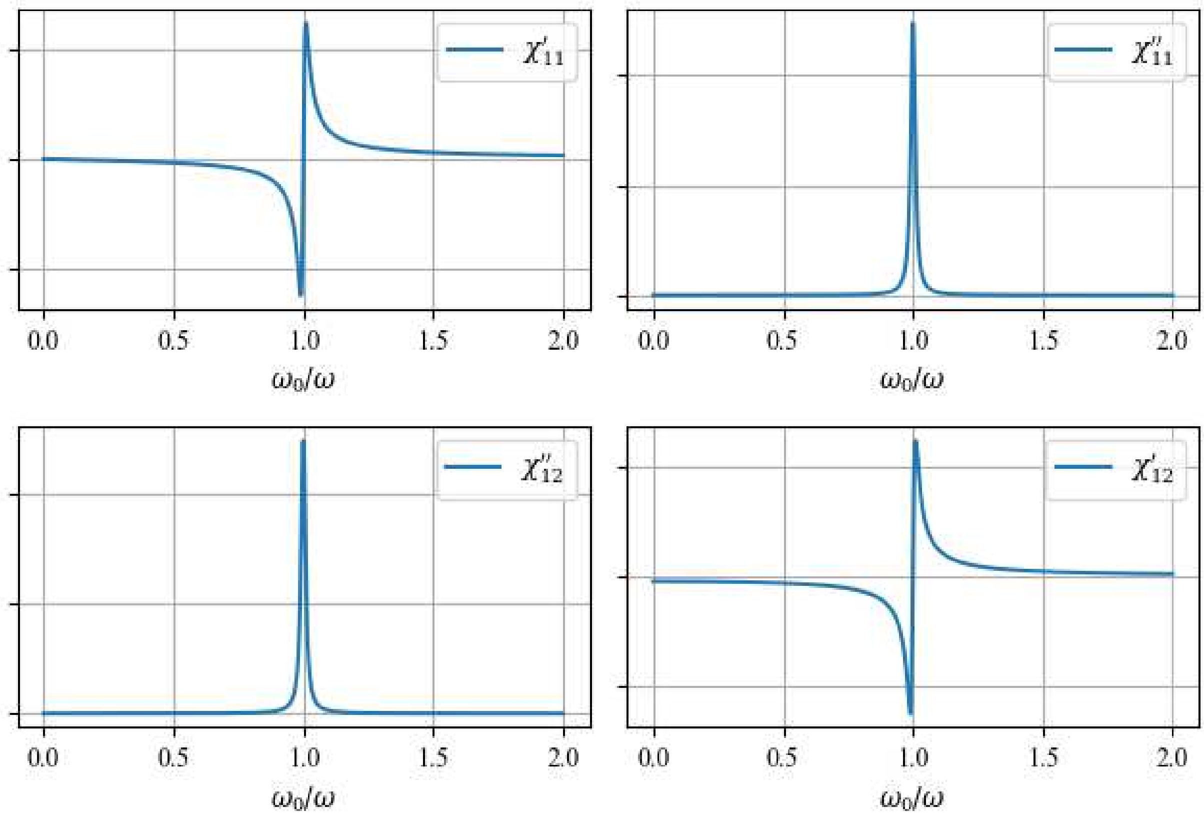

Figure 2.6: Components of the susceptbility tensor, χ, when a loss term is included at the resonant frequency.

determined as twice ω_{02} from the resonance, and converted to units of field strength by expanding the field-frequency notation:

$$\Delta H = \frac{2\alpha\omega}{\mu_0 |\gamma|}. \tag{2.35}$$

An offset term, ΔH_0, represents line broadening due to sample inhomogeneities:

$$\Delta H = \Delta H_0 + \frac{2\alpha\omega}{\mu_0 |\gamma|}. \tag{2.36}$$

(2.36) is the linewidth equation for damping, showing that the resonant linewidth is a function of damping and frequency.

2.4 Ferromagnetic Resonance

Ferromagnetic resonance (FMR) is the phenomenon described in the previous sections: it is the uniform precessional motion of magnetic moments at a resonant frequency of maximum energy absorption. Measurements of FMR provide a method that can be used to determine the damping, gyromagnetic ratio, inhomogeneous line broadening, and internal fields by use of (2.18) and (2.36).[7] FMR is similar to nuclear magnetic resonance (NMR) and electron paramagnetic resonance (EPR), which are more common in biological research or medical applications, but is set apart by the relative strength of the resonance and its relevance to magnetic materials. For those looking for additional information on FMR, it may be beneficial to include resources on NMR and EPR.

2.4.1 Cavity-Based Ferromagnetic Resonance

A common method of measuring FMR is to use a vector network analyzer (VNA) to measure the transmission and reflection properties of a sample. VNA-FMR has many upsides: measurements are fast and broadband, setup (such as a coplanar waveguide "flip-chip"[8] configuration) can often be convenient, and the VNA itself is a powerful and versatile instrument for many microwave experiments. However, the signal-to-noise ratio (SNR) can be quite low, and analyzing the resultant

[7] Using FMR to measure internal fields is typically less convenient than a static measurement like VSM; however, certain applications may prefer FMR. For example, the free layers measured in Chapter 3 are intended to be one part in a stack of magnetic materials. The full stack complicates VSM measurements, but FMR provides a point of comparison.

[8] This is exactly as it sounds: the sample is placed face down on the waveguide.

data to determine complex susceptibility can be difficult. FMR experiments using cavity resonators are the opposite: flexibility and convenience are low, but SNR is high and analysis is simple. Cavity-FMR setups may also be more robust and adaptable; for example, rigid waveguides can handle high power and high temperatures. The latter will be explored in the next section.

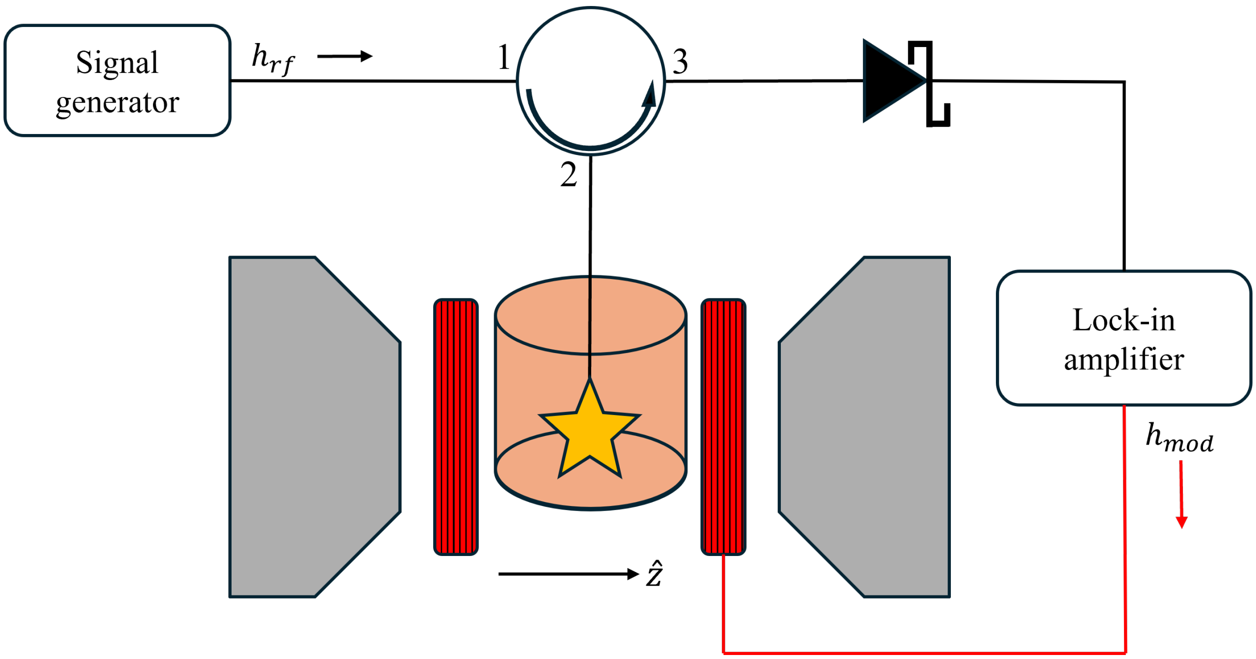

Figure 2.7: Illustration of a typical cavity FMR setup. The sample (star) in a cavity is placed within a field, $H\hat{z}$, provided by the pole pieces (gray trapezoids). The signal, h_{rf}, is reflected from the sample, detected by a Schottky diode, and measured using a lock-in amplifier. The lock-in amplifier also provides a signal to the Helmholtz coils that provide the modulation field, $h_{mod}\hat{z}$.

A standard cavity-FMR experiment is set up as shown in Figure 2.7. An rf signal generator provides a microwave signal, $\mathbf{h}_{rf}$ at some frequency, f. The signal is passed to a circulator or directional coupler to isolate the source signal, which is sent to the sample, and the signal reflected from the sample, which is sent to the detector. The sample is placed between the poles of an electromagnet that provides the dc biasing field, $\mathbf{H}_0 \perp \mathbf{h}_{rf}$, and within a microwave resonant cavity to improve SNR (this could be the end of a shorted waveguide, if the sample resonates strongly enough). Some microwave power is absorbed by the sample, driving the precessional motion. FMR will occur at a resonant frequency per the applied field strength according to the Kittel equation, (2.18). The experiment could sweep the frequency with a fixed field but, in practice, f is kept fixed while H_0 is swept. The power not absorbed by the sample is reflected towards a diode detector and finally to the measuring instrument.

Figure 2.8 shows an example of a fixed-frequency FMR measurement. The x-axis shows the applied field strength, H_0, and the y-axis shows the microwave power absorbed by the sample. The power absorbed is proportional to the imaginary part of the susceptibility χ'', and the result is shown to be a Lorentz (or Cauchy) distribution. The distribution is described by the point of peak absorption, which is the FMR field strength, H_{FMR}, and by its full width at half maximum, ΔH. ΔH is referred to as the FMR linewidth. Note that the quantities of interest, H_{FMR} and ΔH, are both fields—the amount of power absorbed is not typically of interest.

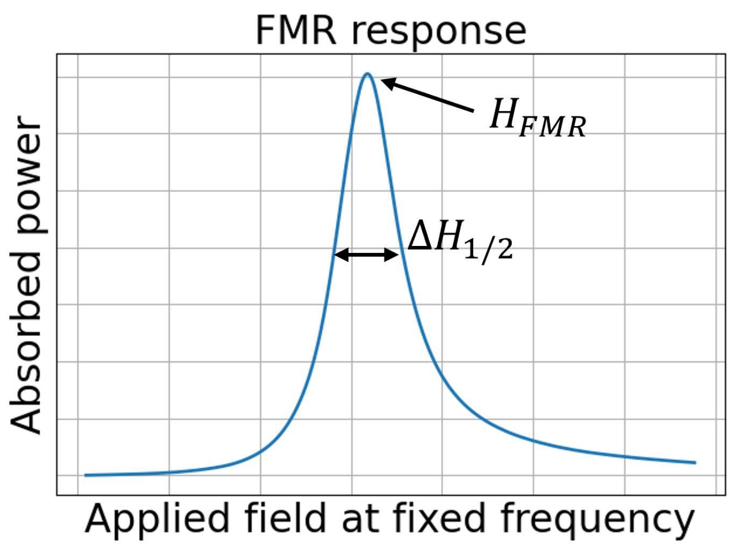

Figure 2.8: Example of a measured permalloy FMR profile. Maximum absorption occurs at the resonant field strength, H_{FMR}. The FMR linewidth, ΔH, is the full width at half maximum.

FMR signals are typically very small, so lock-in detection is typically used as a method of greatly improving the measured SNR. A lock-in detector works by comparing the measured signal against a reference signal at the same frequency. The product of the two signals is a high-frequency term and a dc term proportional to the measured signal amplitude. A low-pass filter then removes the high-frequency term and noise. In fixed-frequency FMR measurements, the lock-in configuration is achieved by modulating $\mathbf{H}_0$ with a low-frequency ($\sim$Hz) field applied in parallel, $\mathbf{h}_{mod} \parallel \mathbf{H}_0$, and provided by a Helmholtz coil: a connected pair of coils that provide a uniform field at their center. The FMR signal is modified in H_0 and compared to the reference signal. The net effect of the modulation in H_0 is that the detected signal becomes the derivative of the FMR response.

Figure 2.9 shows an example of a fixed-frequency FMR measurement using lock-in detection.

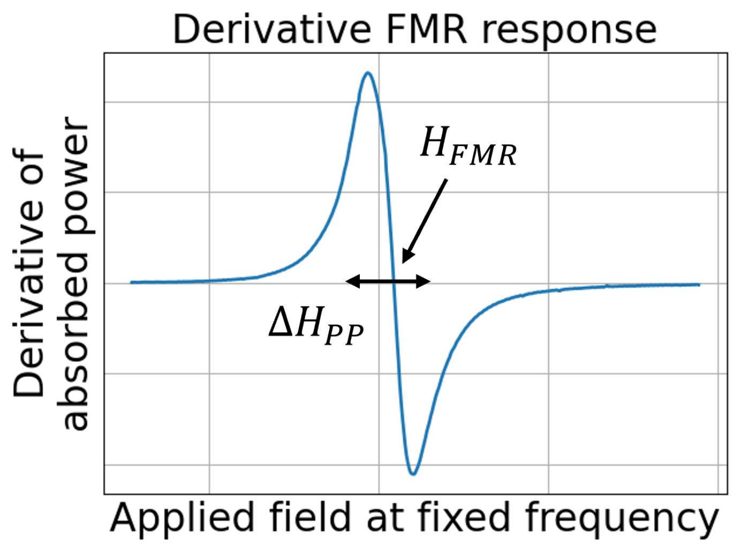

Figure 2.9: Example of a measured permalloy FMR profile using lock-in detection. Now, H_{FMR} is at the crosssing point and the FMR peak-peak linewidth, $H_{pp} = \Delta H/\sqrt{3}$, is measured.

The x-axis shows the applied field strength, H_0, and the y-axis shows the derivative of microwave power absorbed by the sample. The FMR field strength, H_{FMR}, is now observed at the point where the signal crosses the x-axis. The FMR linewidth is measured as the distance between the peak and trough in the signal. This is called the FMR peak-to-peak linewidth, ΔH_{pp}, and it is smaller than the full width at half maximum linewidth, ΔH, by a factor of $\sqrt{3}$:

$$\Delta H = \sqrt{3} \cdot \Delta H_{pp}. \tag{2.37}$$

FMR measurements can be used to determine internal field strengths and γ by using the Kittel equation, (2.18), and to determine α and ΔH_0 using the damping equation, (2.36).

2.4.2 High-Temperature Ferromagnetic Resonance

The amount of digital data that is created and stored has rapidly increased enabled by, e.g., artificial intelligence demands, high-definition content creation and consumption, and centralized network-accessible storage, referred to as "the cloud." Figure 2.10 shows the exponential growth in data created and consumed year over year. The means of storing this data has traditionally been met by magnetics-based hard disk drives (HDDs) which, though they have been surpassed in most other metrics, remain unmatched in price per terabyte of storage.[9] HDD technology has largely remained stagnant in the last twenty years since the generational leaps provided by giant magnetoresistance (GMR) sensors and perpendicular magnetic recording (PMR). Additionally, regular improvements within the current generation have come to reach physically limiting factors, referred to as the magnetic recording trilemma: increasing storage density requires smaller grain volumes (the physical regions whose magnetic moment defines a digital bit), which requires materials with greater anisotropy to maintain thermal stability, which requires greater field strengths to write to those bits. Numerous technologies have been proposed for next-generation HDD devices, and one such technology that has received much research effort is heat-assisted magnetic recording (HAMR). HAMR addresses the trilemma from its third face, and works on the principle that magnetic ordering is reduced at increased temperatures to the Curie temperature, T_C. Heat is applied to the material localized to the bit area to reduce the anisotropy and coercivity of the material for the duration of a write operation. The small region quickly cools and high anisotropy—stability—is restored. HAMR has taken longer than anticipated to realize, but has recently been made available to consumers by Seagate [11].

Characterizing the efficiency of materials at the temperatures required for HAMR has been a challenge for the field. The magnetization dynamics lab at Colorado State University created a cavity-based FMR system to measure damping at high temperatures, which has produced published research on materials related to HAMR (References [12], [13]) as well as on materials related to spin-transfer torque magnetic random-access memory (Chapter 3). The system is fundamentally the same as the system described in Section 2.4.1. The microwave cavity was enclosed in a vacuum chamber with dc and rf feedthroughs, and the cavities were modified to allow for heating the sample while maintaining high Q. A resistive heater cannot be placed directly within the microwave cavity because the conductive heating elements will destroy the resonance condition of the cavity; however, a small hole in the wall of the cavity will only slightly reduce Q. The heater can then be kept external to the microwave cavity, and thermally-conductive dielectric materials can be used to position the sample. The dielectric chosen to position the sample was optical-grade chemical vapor deposition (CVD) diamond, and Ceramabond 865 adhesive paste was used to affix the sample to the diamond.

[9] "diskprices.com" as of Feb. 2026 lists consumer HDDs starting as low as about \$16/TB vs. \$70/TB for solid state drives. Storage demands for artificial intelligence data centers will likely raise these prices.

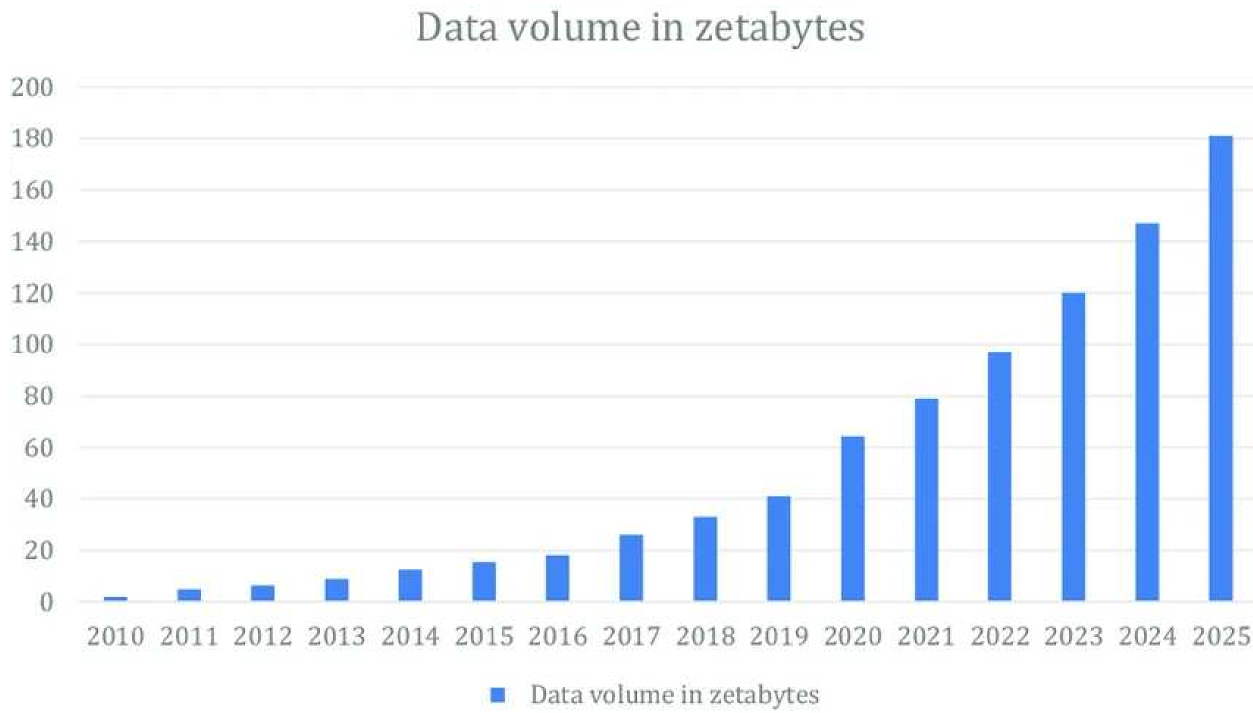

Figure 2.10: The volume of data created, captured, copied, and consumed worldwide, from Statista and based on data from the International Data Corporation.

The sample temperature is controlled by the voltage applied across the heater, and after some time it is reasoned that the temperature is constant. The temperature is determined using one of two methods. In the first, a measurement with the sample replaced by a resistive temperature sensor is used to make a direct relationship of heater voltage to sample holder temperature. In practice, this method was inconsistent and time-consuming, in part because the temperature sensor cannot be used while simultaneously measuring the sample. The second method involves simultaneous FMR measurements of a yttrium iron garnet (YIG) control and relating its resonant field strength to a separate measurement of saturation magnetization vs. temperature. The YIG is placed opposite to the sample on the diamond sample holder. This method is temperature-limited by YIG's $T_C \approx 560\,\mathrm{K}$, and the strong resonance of the YIG must be well-separated (in field) from the resonance of the other sample. If these constraints can be met, then the easily-measured YIG resonance provides an excellent point of reference and sanity check. This is the method chosen for the results presented in Chapter 3.

2.5 Aside: On Yttrium Iron Garnet

Some mention should be made of yttrium iron garnet (YIG, $Y_3Fe_5O_{12}$). YIG is an insulating ferrimagnet (a ferrite) in the family of synthetic garnets with the lowest known damping value. The damping value, on the order of 3×10^{-5}, is two orders of magnitude lower than that in transition metals or alloys such as permalloy (a nickel-iron alloy). This, as well as for being an electrical insulator, has firmly established YIG as the most important material for magnetization dynamics research and applications. YIG is applied in non-reciprocal microwave devices such as circulators, isolators, phase shifters, and resonators. Magnonics devices use YIG because the low damping increases spin wave propagation lengths.

YIG has a complex cubic structure comprised of 160 total atoms (eight formula units) in the unit cell. The magnetization arises from the 40 Fe^{3+} cations that are split 16:24 between octahedral and tetrahedral sublattices. The sublattices have anti-aligned moments (hence, a ferrimagnet), and the net result is 8 Fe^{3+} of $5\mu_B$ each, so $M_s = 40\mu_B$ per unit cell. This is equivalent to $M_s = 196\ \mathrm{kA\,m^{-1}}$ at 0 K for a lattice constant of 12.376 Å. At room temperature, the magnetization is widely accepted as $M_s = 1750$ Oe $= 139\ \mathrm{kA\,m^{-1}}$. The Curie temperature is 560 K [14].

Additionally, YIG has a very small cubic anisotropy with an easy axis in the crystallographic [111] direction, and thin films are usually grown with this direction normal to the surface (out-of-plane). However, since the applied field in experiments is typically much greater than the anisotropy field it is usually considered negligible. YIG can be grown by several methods, including sputtering, pulsed-laser deposition, and liquid-phase epitaxy for thin films, with each method providing relative advantages and disadvantages. Another synthetic garnet, gadolinium gallium garnet (GGG), $Gd_3Ga_5O_{12}$, a paramagnet, is typically used as a substrate material.

Chapter 3. High-Temperature Ferromagnetic Resonance

3.1 Introduction

A spin-transfer-torque (STT) magnetic random-access-memory (MRAM) cell is usually composed of three layers: (1) a free layer, the magnetization of which can be switched by STT between two distinct directions, corresponding to binary values; (2) a reference layer that has fixed magnetization and works as a spin polarizer to produce spin currents for the free layer; and (3) a non-magnetic barrier, such as an MgO layer, that physically separates the free and reference layers [15], [16]. Ideal STT MRAM devices require that (1) the critical current density, J_c, needed to switch the free layer is minimized, and (2) an effective thermal stability parameter, Δ is maximized. In general, J_c is proportional to the product of the free layer thickness t_F, saturation magnetization M_s, and Gilbert damping constant α, i.e., $J_c \propto t_F M_s \alpha$, and Δ scales as the product of M_s, the perpendicular anisotropy field H_u and inverse temperature T, i.e., $\Delta \propto H_u M_s / T$ [17], [18]. One can see that a desired free layer should be thin and have low damping, while simultaneously exhibiting large magnetization and strong anisotropy.

The STT MRAM free layer is often made of a Co-Fe-B/W/Co-Fe-B trilayered structure, where W may be replaced by other metals such as Ta or Mo. The roles of the W layer in this "conventional" free layer are (1) to absorb boron during annealing and thereby ensure solid-phase epitaxy at the Co-Fe-B/MgO interface, and (2) to help realize strong perpendicular anisotropy in the Co-Fe-B layers [19], [20]. However, the W layer unfortunately creates dead layers, which reduce the effective M_s and enhance the damping of the free layer, resulting in a higher J_c. The use of two ultrathin W layers is shown to be a way to improve free-layer properties compared to a single W layer [21], [22]. Santos et al. proposed in 2020 to split the single W layer into two thinner layers and thereby mitigate W-produced damping enhancement and dead layers [22]. Specifically, they fabricated a Co-Fe-B/Co-Fe/Mg/W/Co-Fe/Mg/W/Co-Fe structure with two ultrathin W layers that showed a reduced α, a reduced t_F, and an increased M_s when compared with the conventional free layer with a single W layer. The STT MRAM device built on this low-α free layer showed a lower J_c and a higher Δ than the device made of the conventional free layer [22].

Reported here are comparative studies of high-temperature frequency-dependent ferromagnetic resonance (FMR) in (1) the low-α free layer with split W layers, and (2) the conventional free layer with a single W layer, which are described above. Comphrehensive FMR measurements show that, over the temperature T range from 300 K to 520 K, the damping constant of the low-α free layer is always smaller than that of the conventional free layer. Furthermore, the damping constants in the two samples both increase monotonically with an increase in T, but at very different paces. Specifically, as T varies from 300 K to 520 K, the damping constant in the low-α free layer increases nearly linearly, from about 0.0035 to 0.0079, while the damping constant in the conventional free layer increases nearly exponentially, from about 0.0092 to 0.028. These results can be interpreted in terms of the T dependence of the damping produced by spin-flip magnon-electron scattering [23], [24], [25], [26] and the difference of the Curie temperatures T_C of the two free layers [22]. They clearly establish the advantages of the low-α free layer over the conventional free layer from the perspective of the STT MRAM application.

It should be highlighted that the high-temperature damping properties reported below are of great technological significance because STT MRAM cells operate above room temperature. The temperature dependencies and the differences between the low-α and conventional free layers have important implications for the future design and optimization of STT MRAM free layers. The high-T damping values presented below can also be used as firsthand input damping parameters for industrial modeling and simulations of STT MRAM devices.

3.2 Spin-Transfer Torque

When a current of electrons with unpolarized spins (a charge current) is incident on a ferromagnetic (FM) layer, the FM acts as a filter allowing electrons with magnetic moments aligned with the FM to pass (a spin current). Unaligned moments may be rejected, and those remaining are aligned with the FM. The alignment is due to a torque exerted on the moments by the FM. When the spin-polarized current is incident on a second FM layer, the equal and opposite force exerted by the spin current on the FM is called spin-transfer torque. With a large enough current density, J, the spin-transfer torque can maintain a precession in the FM, called a spin-torque oscillator, or can flip the magnetization. A spin-transfer torque device is therefore a magnetic device with electronic control.

The LLG equation of motion was expanded to show the spin transfer torques:

$$\frac{d\mathbf{M}}{dt} = -\mu_0 \left|\gamma\right| \mathbf{M} \times \mathbf{H} - \frac{\alpha}{M_s}\mathbf{M} \times \frac{d\mathbf{M}}{dt} + \beta\frac{J}{M_s t}\mathbf{M} \times (\mathbf{M} \times \mathbf{m}) + \beta' \frac{J}{M_s t}\mathbf{M} \times \mathbf{m}. \tag{3.1}$$

Capital $\mathbf{M}$ refers to the moment of the FM and lowercase $\mathbf{m}$ refers to the spin current. t is the thickness of the ferromagnet, and β and β' collect constants. This is the LLG-Slonczsewski equation of motion. The first and second terms are the familiar precessional term and Gilbert damping term. The third term is similar in form to the damping term but with opposite sign. The fourth term is similar to the precessional term and additive with it.

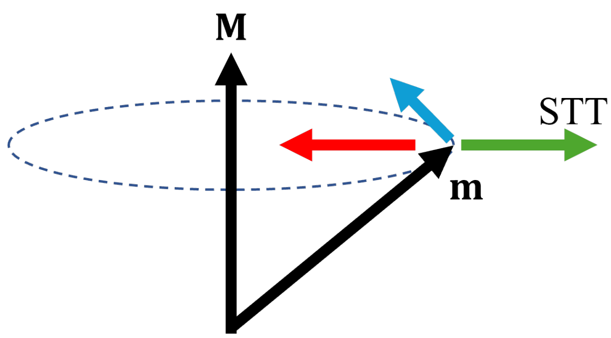

Figure 3.1: Spin-transfer torque due to a spin-polarized current of electrons with magnetic moments $\mathbf{m}$ acting upon a ferromagnetic layer with magnetization $\mathbf{M}$. Blue and red arrows indicate the precessional and damping torques.

Spin-transfer-torque switching as a mechanism for flipping magnetic moments is naturally complemented by measurements of tunnel magnetoresistance (TMR). TMR is present in structures of ferromagnets (FM) separated by a thin nonmagnetic (NM) layer, i.e., FM/NM/FM, called a magnetic tunnel junction (MTJ). A voltage applied across the MTJ creates some current due to electrons that are able to quantum mechanically tunnel through the NM layer. Tunneling is facilitated when the FM layers have aligned magnetizations, and the resistance is low. When the FM magnetizations are anti-aligned, the resistance is high. The TMR ratio, ρ, is

$$\rho = \frac{R_{AP} - R_P}{R_P}, \tag{3.2}$$

where R_{AP} and R_P are the resistances of the anti-parallel and parallel states, respectively. A greater TMR ratio corresponds to a greater sensitivity. Using MgO as the tunneling layer, TMR ratios of hundreds of percent have been measured at room temperature [27] and theory suggests that there is room for significant growth.

STT-MRAM takes advantage of the spin-transfer torque and measurements of TMR for writing and reading, respectively, the free layers that define the state of the memory cell. The application and manufacturing of STT-MRAM is an active topic within the memory industry.

3.3 Free-Layer Samples

Two free layer samples were measured and compared. The low-α free layer sample, referred to as sample A, is a multilayer of CoFeB(0.6)/ CoFe(0.1)/ Mg(0.4)/ W(0.02)/ CoFe(0.32)/ Mg(0.4)/ W(0.02)/ CoFe(0.32), where the numbers indicated layer thickness in nm. The total thickness of samples A is $t_F^A = 1.38\,\text{nm}$. The conventional free layer sample, referred to as sample B, is a multilayer of CoFeB(1.3)/ Mg(0.6)/ W(0.3)/ CoFeB(0.7) with a total thickness $t_F^B = 2.3\,\text{nm}$. Note that sample A has two W layers while sample B has a single W layer. The Mg layers in the samples act as sacrificial layers to protect the CoFeB layers during W deposition and, therefore, are not included in the total film thickness [22], [28]. These free layer samples were fabricated by sputtering in the following sequence on Si/SiO_2 substrates: nonmagnetic seed layer/ MgO /free layer/ MgO/ Ru/ Ta/ Ru. A nonmagnetic seed layer was used instead of a magnetic reference layer to ensure that the only magnetic signal in our detailed magnetic characterization came from the free layer. All details about the fabrication and structural properties of these two samples are provided in reference [22]. The major magnetic properties of the samples are summarized in Table 3.1. The table includes key results, which are discussed in detail in Section 3.6.

Three points should be made about the two samples. First, it is intentional to design sample A and sample B to have large differences in both the W thicknesses and the total free layer thicknesses, which produce significant differences in M_s, T_C, and α. This ensures that the sample properties' temperature dependencies are very different, thus making a more interesting comparison for this study of damping as a function of T. Second, the thicknesses of all the layers were determined according to the sputtering time and the film deposition rate. Third, given that the diameter of a

Table 3.1: Properties of MRAM free layer samples: low-α (sample A) and conventional (sample B). Thicknesses were determined according to the sputtering time and deposition rate. The Curie temperature and saturation magnetization were measured with a physical property measurement system. All other parameters were determined through ferromagnetic resonance measurements.

Property	Sample A	Sample B
Structure	CoFeB/CoFe/W/CoFe/W/CoFe	CoFeB/CoFe/W/CoFe
Thickness t_F (nm)	1.38	2.30
Curie temperature T_C (K)	~ 900	~ 650
Saturation magnetization M_s (emu/cm^3) (300 K)	1680	1033
Interfacial anisotropy constant K_i (erg/cm^2) (300 K)	2.69	1.90
Effective anisotropy field H_{eff} (kOe) (300 K)	2.15 ± 0.12	3.04 ± 0.04
Effective anisotropy field H_{eff} (kOe) (520 K)	0.22 ± 0.07	0.39 ± 0.35
Damping constant α (300 K)	$(3.5 \pm 0.9) \times 10^{-3}$	$(9.2 \pm 1.1) \times 10^{-3}$
Damping constant α (520 K)	$(7.9 \pm 1.2) \times 10^{-3}$	$(28.0 \pm 5.8) \times 10^{-3}$
Inhomogeneous line broadening ΔH_0 (Oe) (300 K)	133.1 ± 8.7	111 ± 11
Inhomogeneous line broadening ΔH_0 (Oe) (520 K)	37.8 ± 12.1	18.9 ± 46.6

W atom is about 0.3 nm, sample B has just a monolayer of W atoms. As such, the W layers do not have enough atoms to establish a crystal structure. Thicker W layers deposited on CoFeB layers have a β phase for thicknesses no larger than about 3.0 nm but have an α phase for thicknesses larger than about 3.0 nm.

3.3.1 Static Magnetic Properties

Magnetic hysteresis loops were measured on samples A and B over a temperature range from room temperature (approximately 300 K) to 600 K. The measurements were carried out using a physical property measurement system (PPMS) with the magnetic field applied in-plane with the sample film surfaces. Error function fits to those hysteresis loops yielded for each sample the saturation magnetization M_s and effective anisotropy field $H_{eff} = H_u - 4\pi M_s$, where H_u is the perpendicular anisotropy field strength. Figure 3.2(a) presents the M_s against T data. One can see that, as T increases from 300 K to 600 K, M_s decreases from 1680 emu/cm^3 to 1300 emu/cm^3 in sample A and from 1030 emu/cm^3 to 500 emu/cm^3 in sample B. These results suggest that sample A will have greater thermal stability Δ than sample B, particularly at high temperature. Figure 3.2(b) gives the H_{eff} against T data. The data show that H_{eff} decreases monotonically in both samples and approaches zero near 575 K; H_{eff} in sample A is smaller than in sample B, but the difference is reduced with an increase in T. The H_{eff} values are positive for the entire T range in both samples. This implies that $H_u > 4\pi M_s$ in both samples, which is a requirement for perpendicular MRAM applications. The decrease of H_{eff} with T indicates that H_u decreases more than $4\pi M_s$ as T increases.

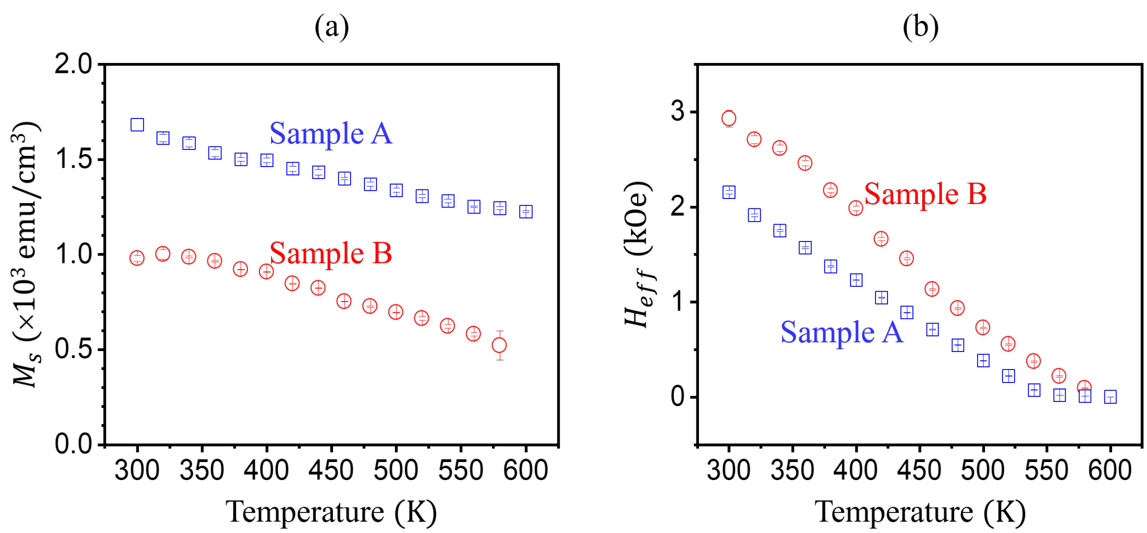

Figure 3.2: Static magnetic properties of Sample A and Sample B. (a) Saturation magnetization M_s as a function of temperature T. (b) Effective anisotropy field $H_{eff} = H_u - 4\pi M_s$ as a function of T, where H_u and $4\pi M_s$ denote the perpendicular anisotropy field and the saturation induction, respectively.

The $M_s(T)$ data in Figure 3.2 also allow for the evaluation of the sample Curie temperatures T_C by fitting the $M_s(T)$ response to the Kuz'min equation [29], [30], [31]:

$$M_s(T) = M_s(0)\left[1 - s\left(\frac{T}{T_C}^{3/2}\right) - (1-s)\left(\frac{T}{T_C}^{5/2}\right)\right]^{1/3} \tag{3.3}$$

where $M_s(0)$ denotes M_s at $T = 0\,\text{K}$ and s is a parameter related to, among other properties, the exchange constant. Fitting the data yields $T_C^A = (900 \pm 100)\,\text{K}$ for sample A and $T_C^B = (650 \pm 25)\,\text{K}$ for sample B. M_s and T_C are both larger in sample A than in sample B, consistent with the previous observation that in free layers with nonmagnetic spaces higher M_s gives rise to higher T_C [32].

Additionally, the $4\pi M_s$ and H_{eff} data in Figure 3.2 determine the interfacial anisotropy constant K_i as

$$K_i = \frac{1}{2} M_s H_{eff} t_F + 2\pi M_s^2 t_F \tag{3.4}$$

K_i for each sample at room temperature are given in Table 3.1.

3.4 Room Temperature Ferromagnetic Resonance

Prior to high-temperature FMR measurements, room temperature measurements were carried out on the samples with two distinct techniques: (1) cavity FMR and (2) vector network analyzer (VNA) FMR. The cavity FMR measurements were conducted with the high-temperature FMR system described in Section 3.5. The measurements used six high-Q cylindrical cavities with resonance frequencies within the K_u band. The VNA FMR experiments involved the measurement of the scattering parameters of a coplanar waveguide and sample structure by a VNA system [33], [34]. All measurements were performed with the magnetic field applied out-of-plane with the sample film.

Table 3.2 presents the measured room-temperature FMR data. The effective anisotropy field, H_{eff}, values were obtained by fitting the FMR field, H_{FMR}, versus microwave frequency, f, data to the Kittel equation:

$$2\pi f = |\gamma| \left(H_{FMR} + H_{eff}\right) \tag{3.5}$$

The Gilbert damping constant α and the inhomogeneous line broadening ΔH_0 were obtained by fitting the FMR linewidth, ΔH, versus f data to the linewidth equation

$$\Delta H = \frac{1}{\sqrt{3}} \left[\frac{2\alpha}{|\gamma|} (2\pi f) + \Delta H_0\right] \tag{3.6}$$

Two remarks should be made about (3.6). First, the linewidth, ΔH , refers to the peak-to-peak linewidth, which is a factor of $\sqrt{3}$ smaller than the full width at half maximum linewidth. Second, ΔH_0 does not represent loss; it is the broadening of the FMR line due to the spatial inhomogeneity of the material properties across the sample, such as the spatial variation of M_s or H_u. For data in the fourth column of Table 3.2, the second value in each cell was measured without the vacuum

Table 3.2: Comparison of room-temperature FMR results for both samples measured with two different techniques: (1) cavity FMR and (2) VNA FMR. For (1), the FMR measurements were carried out with six cylindrical cavities in the Ku band for which the frequency ranged from 12.4 to 18 GHz. For (2), the FMR measurements made use of a coplanar waveguide and a VNA over a frequency range from 13 to 42 GHz. All the measurements were performed under a perpendicular magnetic field.

Property	Sample A		Sample B	
	Cavity FMR	VNA FMR	Cavity FMR	VNA FMR
Effective anisotropy field H_{eff} (Oe)	2150 ± 118	2235 ± 3	3099 ± 75 2970 ± 15	2990 ± 3 2984 ± 3
Damping constant α ($\times 10^{-3}$)	3.5 ± 0.9	3.5 ± 0.2	8.7 ± 2.2 9.7 ± 0.5	11.4 ± 0.2 11.6 ± 0.3
Inhomogeneous line broadening ΔH_0 (Oe)	133.1 ± 8.7	114 ± 4	104 ± 5 118 ± 22	73 ± 4 70.6 ± 5.5

chamber and its associated components and with smaller field steps in comparison with the other values measured by the cavities. The data in the fifth column were obtained on the same samples through two separate measurements.

One can see three major results from Table 3.2. First, the two sets of data measured by the two FMR techniques are fairly consistent with each other. Second, in contrast to the nearly perfect agreement between the two damping values for sample A, the damping values for sample B are slightly different. Possible reasons for this difference include that the FMR signals from sample B are weaker than those from sample A, which is due to the fact that sample B has smaller magnetization and larger damping than sample A. Third, the parameters measured by the cavity technique have larger error bars than those measured by the VNA technique. This is because the cavity technique is limited by the number of microwave cavities available (six cavities) and their total frequency bandwidth (about 5.3 GHz), whereas the VNA FMR technique can measure almost continuously across a much wider frequency range (about 29 GHz). However, the VNA FMR technique is limited to room-temperature measurements. Note that for the room-temperature α values shown in Table 3.1, the one for sample A is the same as the corresponding value in Table 3.2 measured by the cavity technique, while the one for sample B is the average of the two values in Table 3.2 measured by the cavity technique.

3.5 High-Temperature Ferromagnetic Resonance Approach

The high-temperature FMR measurements were carried out with a system that was an adaptation of a fixedfrequency cavity FMR setup [35], [36], [37]. Figure 3.3 shows a schematic diagram of the system. The major components include a diamond rod, a ceramic heater, a cylindrical cavity, and a vacuum chamber. The MRAM free layer sample is adhered with an aluminum nitride adhesive (Aremco Ceramabond 865) to one end of a diamond rod, the other end of which is affixed to a ceramic heater, as illustrated in Figure 3.3. The diamond rod loads the sample into the cavity through a small hole at the center of the bottom of the cavity. The microwave in the cavity is in the TE_{011} mode. The diamond rod is inserted along the central cylindrical axis of the cavity such that the sample is subject to an in-plane microwave magnetic field (h) and receives the maximum magnetic power and minimum electric power from the microwave. To minimize sample degradation and to avoid heat loss to surroundings, the cavity-diamond heater assembly is housed in a chamber that has vacuum on the order of 10^{-5} torr. Although not shown in Figure 3.3,an electromagnet applies a static magnetic field (H) to magnetize the sample along the film normal direction. Data presented below were measured with six K_u-band cylindrical cavities. The resonance frequencies of these cavities are 12.4 GHz, 13.2 GHz, 14.1 GHz, 15.3 GHz, 17.3 GHz and 17.7 GHz; the corresponding unloaded quality factors are 13 100, 15 000, 6500, 9300, 6200 and 17 700, respectively.

For each measurement, the external magnetic field is swept, and the microwave power reflected from the cavity is recorded as a function of the field using a Schottky diode (Herotek DZ1026). The obtained power absorption versus field profile ideally has a Lorentzian shape. However, to increase the signal-to-noise ratio, the measurement uses field modulation and lock-in detection techniques, which means that what is measured is the derivative of the microwave power absorption versus field responses. In other words, each FMR profile measured has a shape of the derivative of a Lorentzian function.

Design considerations of the microwave cavities determine that the temperature of the sample cannot be measured directly. For example, the insertion of a conductive thermocouple into the cavity to measure the temperature would significantly reduce the quality factor of the cavity, and thus, the quality and strength of the FMR signals. The ceramic heater can be calibrated separately from the electric voltage applied to it, but the sample temperature is instead determined in situ by

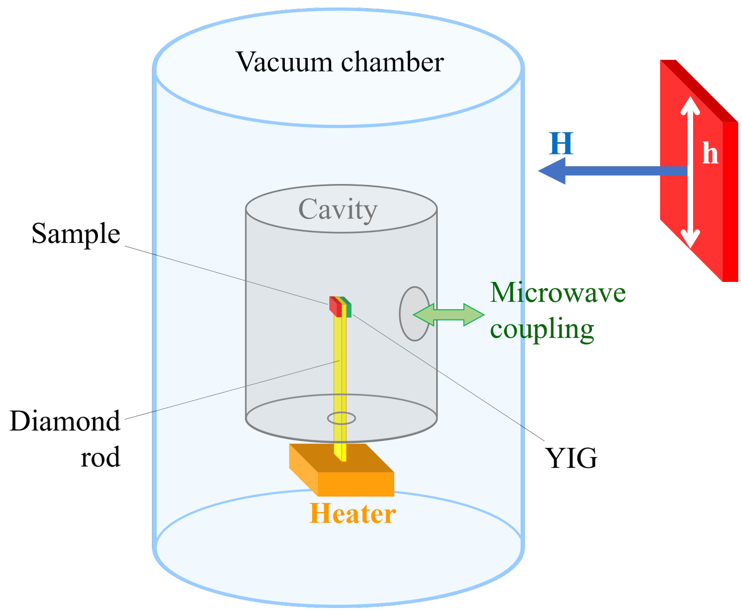

Figure 3.3: Experimental setup for high-temperature ferromagnetic resonance. An MRAM free-layer sample is loaded to a cylindrical cavity via a diamond rod. The diamond rod also transfers heat from a ceramic heater outside the cavity to the sample. The sample is subject to a microwave magnetic field ($\mathbf{h}$) that is along the cavity cylindrical axis (vertical) and an external static magnetic field ($\mathbf{H}$) that is along the film normal direction (horizontal). An YIG thin film is affixed to the diamond rod on the opposite side of the MRAM free-layer sample. The YIG film is measured for temperature determination.

making a second FMR measurement on an yttrium iron garnet (YIG) thin-film element. The YIG film element is a square with a width of about 2 mm. The YIG film is 15.1 µm thick and grown on a single-crystal gadolinium gallium garnet (GGG) substrate by liquid-phase epitaxy. It is attached to the diamond rod on the opposite side of the MRAM free-layer sample, with the film side facing the diamond rod. At equilibrium, the average temperatures of the free layer sample and the YIG film should be approximately the same.

The YIG film has multiple advantages for use as a reference material for temperature determination. It is an insulator that has a low impact on the quality factor of the microwave cavity; it has a strong resonance that is easy to measure, even near T_C, and for a given microwave frequency, the resonant field strength of the YIG film is well separated from that of the free layer sample. Additionally, the YIG film has negligible magnetic anisotropy, so one can directly correlate the FMR field versus temperature data with the saturation induction versus temperature data obtained from the static magnetic measurements. This final point provides a method to effectively determine the sample temperature, as detailed below. One downside of the YIG film is its relatively low T_C, which limits this method to $T_C \approx 560\,\text{K}$.

Figure 3.4 shows how the YIG measurements enable the determination of the sample temperature in the hightemperature FMR measurement. Graph (a) presents an FMR profile measured on the YIG film with the 17.7 GHz cavity at a high temperature, T, to be determined. Graph (b) presents the profile that is the integration of the one in graph (a). Graph (c) gives $4\pi M_s$ versus T data measured by a PPMS. All the measurements were carried out with a perpendicular magnetic field. The multiple resonances shown in graphs (a) and (b) correspond to the standing waves of the forward-volume magnetostatic waves across the lateral dimensions of the YIG film element. The strongest resonance at the high-field side is centered at a field close to the FMR field (H_{FMR}). Data in graph (c) are the $4\pi M_s$ values normalized to the value measured at room temperature. The data indicate $T_C \approx 560\,\text{K}$, which is expected. The nonzero values at $T > 560\,\text{K}$ are associated with the magnetic moments in the paramagnetic GGG substrate.

Temperature determination involves the following major steps:

1. Use the integrated FMR profile to determine H_{FMR}, as indicated in Figure 3.4(b).

2. Use the H_{FMR} value and the Kittel equation, (3.5), to estimate the $4\pi M_s$ value.

3. Normalize the $4\pi M_s$ value from step (2) to the value measured at room temperature.

4. Use the normalized value and the plot in Figure 3.4(c) to determine the temperature, as indicated by the two arrows in Figure 3.4(c).

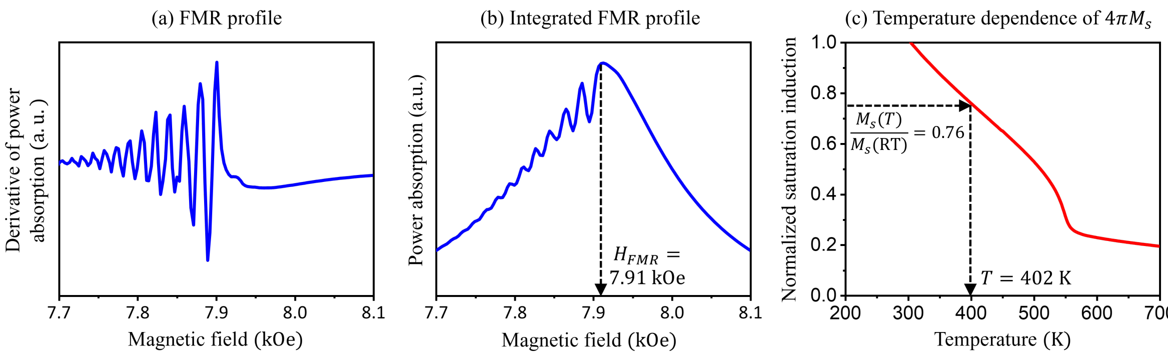

Figure 3.4: Temperature determination through static and FMR measurements of an YIG thin film. (a) High-temperature FMR profile measured on an YIG film. (b) FMR profile after the integration of the profile in (a). (c) Saturation induction $4\pi M_s$ of the YIG film measured as a function of temperature using a physical property measurement system. Values in (c) are normalized to the $4\pi M_s$ value measured at room temperature, namely, $4\pi M_s(RT)$. Temperature determination involves the following major steps: (1) determine the FMR field H_{FMR} as indicated by the vertical arrow in (b); (2) use H_{FMR} and the Kittel equation to determined $4\pi M_s$; and (3) use the $4\pi M_s$ value, indicated by the horizonal arrow in (c), and the $4\pi M_s$ against temperature plot to determine the temperature, indicated by the vertical arrow in (c).

3.6 High-Temperature Ferromagnetic Resonance Results

The high-temperature FMR measurements made use of the six Ku-band cylindrical cavities described in Section 3.5. For each cavity, a sequence of measurements were conducted at different temperatures T that increased from 300 K to 520 K. When switching to a different cavity, a new piece of the free layer sample was used. The upper temperature limit is determined during measurements by the quality of the FMR signals, which tend to weaken and distort as the sample temperature approaches T_C.

Figure 3.5 presents representative FMR profiles measured on sample A, the low-α free layer sample. Data in each row were measured with one and the same microwave cavity, with the cavity resonance frequency indicated on the left side. Data in each column were measured at the same temperature, as indicated at the top of each column. In each graph, the blue dots represent the derivative of the microwave power absorption measured as a function of the magnetic field H, while the red curve is a fit to the derivative of a Lorentzian trial function. The fitting yields the FMR field H_{FMR} and peak-to-peak linewidth ΔH values, which are presented in Figure 3.7.

Three results are evident from the FMR data in Figure 3.5. First, with an increase in temperature, the resonance shifts to a higher magnetic field. This is consistent with the fact that the effectively anisotropy field H_{eff} decreases with temperature, as shown in Figure 3.2(b), and to maintain the FMR at the same frequency a higher field is needed, according to (3.5). Second, with an increase in the cavity frequency, the resonance also shifts to a higher field. This is a reflection of the linear scaling of the FMR frequency with the magnetic field, as shown in (3.5). Third, some of the FMR profiles, such as those in Figure 3.5(a-i) and 3.5(b-ii), do not show the usual antisymmetric responses. These profile distortions are likely due to the mixing of the real and imaginary parts of the complex magnetic susceptibility χ, as discussed in references [38], [39]. For those FMR profiles, the numerical fitting used an equation that had two components: (1) a usual antisymmetric component associated with the imaginary part of χ , and (2) a symmetric component associated with the real part of χ .

Figure 3.6 presents representative FMR profiles measured on sample B, the conventional free-layer sample. Data are presented in the same format as those in Figure 3.5. One observes the same results as those described above for Figure 3.5. There are also quantitative differences in the FMR properties of the two samples, which are discussed shortly. One difference of particular note here is as follows: the derivative lineshape for sample B begins to weaken and become steplike, even at $T = 450\,\mathrm{K}$, whereas sample A maintains a clear derivative lineshape over the entire temperature range. One can attribute this difference to the differences in the Curie temperatures and damping constants of the two samples. As shown in Table 3.1, sample B has a much lower T_C than sample A. As the sample temperature approaches T_C, the magnetic moment becomes small and the measured resonance strength becomes weak. Sample B also has a larger Gilbert damping constant α for all the temperatures, as detailed below, which also contributes to weaker FMR signals.

Turn now to the H_{FMR} and ΔH results obtained from the numerical fitting of the experimental FMR profiles described above. Figure 6 presents the results for sample A. The first row gives H_{FMR} data measured at three different temperatures, as indicated. In each graph, the blue dots show the H_{FMR} values at different frequencies, while the red lines are numerical fits to (3.5). The fitting

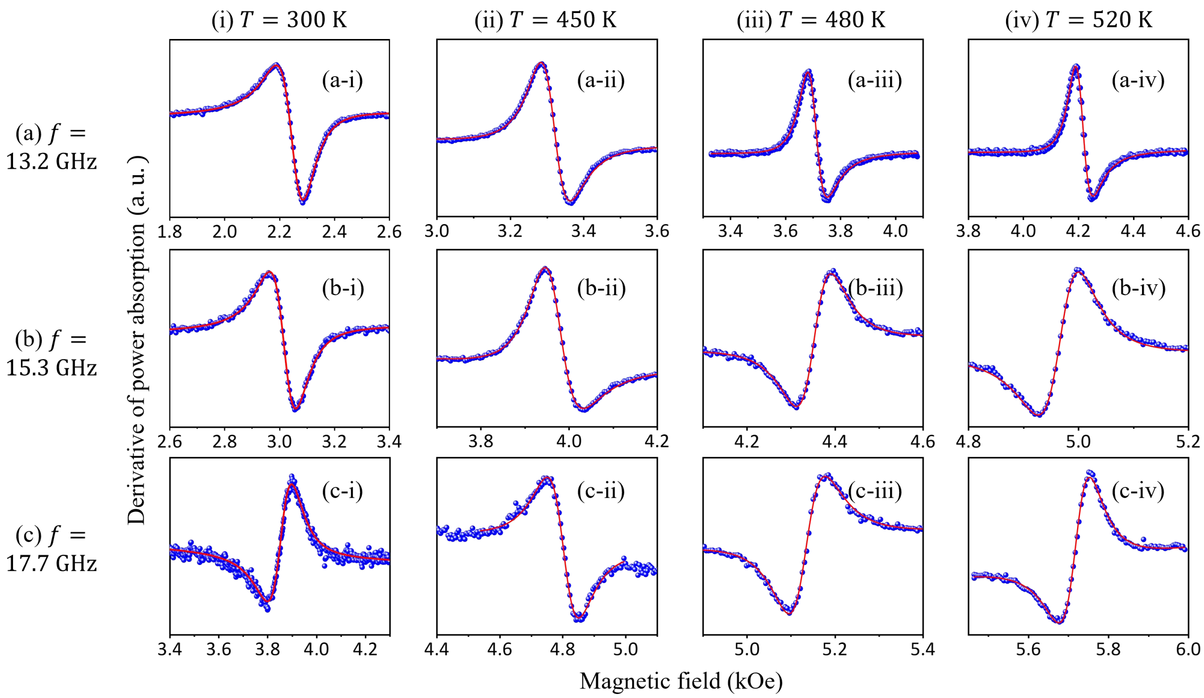

Figure 3.5: Representative FMR profiles measured on sample A. Data in each row were measured with one and the same cavity, with the cavity frequency given on the left side. Data in each column were measured at the same temperature, as indicated at the top. Blue dots show the experimental data points, while the red curves are numerical fits.

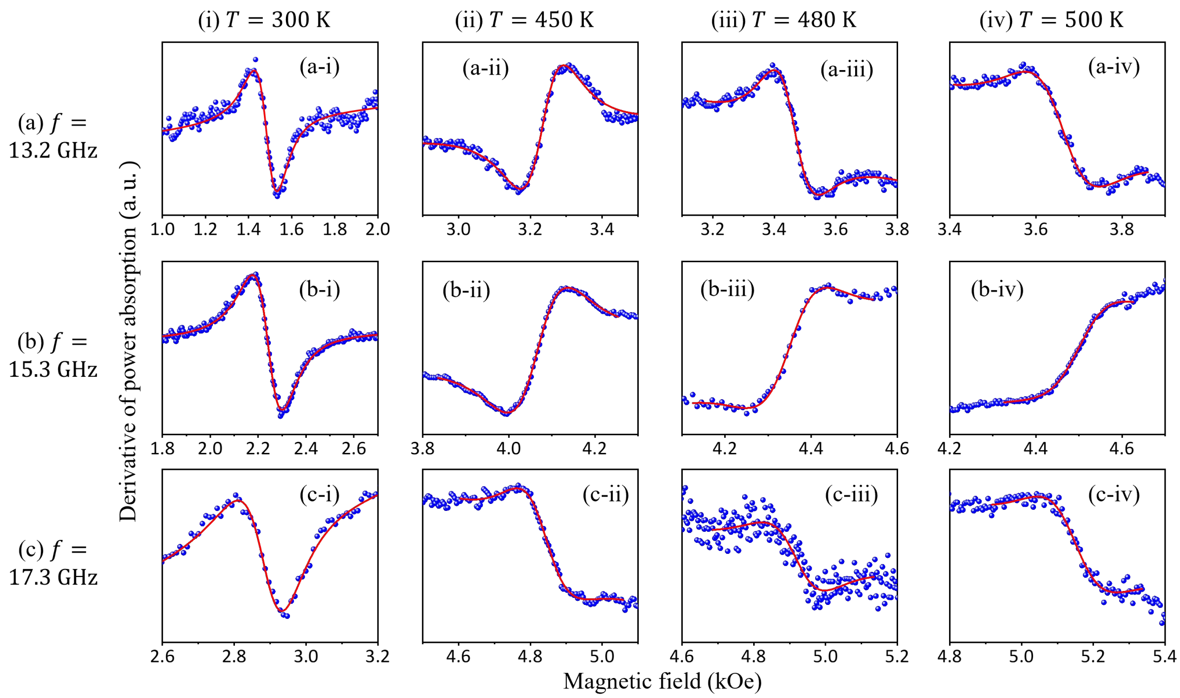

Figure 3.6: Representative FMR profiles measured on sample B. Data in each row were measured with one and the same cavity, with the cavity frequency given on the left side. Data in each column were measured at the same temperature, as indicated at the top. Blue dots show the experimental data points, while the red curves are numerical fits.

yielded effective anisotropy fields H_{eff} and the absolute gyromagnetic ratios $|\gamma|$ are indicated. The second row gives ΔH data that correspond to the H_{FMR} data in the first row. In each graph, the blue dots show the ΔH values at different frequencies, while the red lines are fits to (3.6). The fitting-yielded Gilbert damping constant α and inhomogeneous line broadening ΔH_0 values are indicated in the graphs. Two notes should be made about data in Figure 3.7. First, the multiple data points for a given cavity and a given temperature resulted from repeated measurements. Second, only data from three cavities are presented. This is because the 12.4 GHz cavity had not been fabricated at the time of the measurement of sample A, and the relatively low quality factors of the 14.1 GHz and 17.3 GHZ cavities led to poor FMR signals.

Data in Figure 3.7 show important results on how H_{eff}, α, and ΔH_0 vary with temperature, as discussed shortly. Presented here are a few remarks about the numerical fitting in Figure 3.7. First, data in the first row can be nicely fit. This indicates that the sample temperatures in the three different cavities are equivalent to each other. One can also notice that, in comparison with those in Figure 3.7(a-i) and 3.7(a-ii), the data points in Figure 3.7(a-iii) are slightly more scattered, even though the trend is still well defined. This means that at relatively high temperatures the repeated points have more variance at each frequency. Possible reasons for this include that (1) the accuracy of the temperature determination described in Section 3.5 is reduced as the temperature approaches the Curie temperature of the YIG film, and (2) at high temperature the FMR signals of the free layer samples generally tend to become weaker due to the reduced magnetic moments, as shown in Figure 3.2(a), and the enhanced damping, as shown in Figure 3.9(a). Second, in contrast to data in the first row, the linewidth data in the second row are more scattered, which indicates that the variance in linewidth measurements is more pronounced. Nevertheless, the linewidth data clearly show linearly increasing trends with frequency, as expected according to (3.6). The fitting of data to (3.6) yields α and ΔH_0 values with relatively large uncertainties that are the reflections of the scattering of the data points.

Figure 3.8 presents H_{FMR} and ΔH data and the corresponding fits for sample B, using the same format as that in Figure 3.7. The fitting-yielded results for H_{eff}, α,and ΔH_0 are discussed shortly. Three remarks about these data are as follows. First, the ΔH versus cavity frequency f data in the second row are more scattered than the H_{FMR} versus f data in the first row, similar to data presented in Figure 3.7. Second, the fitting shown in Figure 3.8(b-i) seems to be done with the

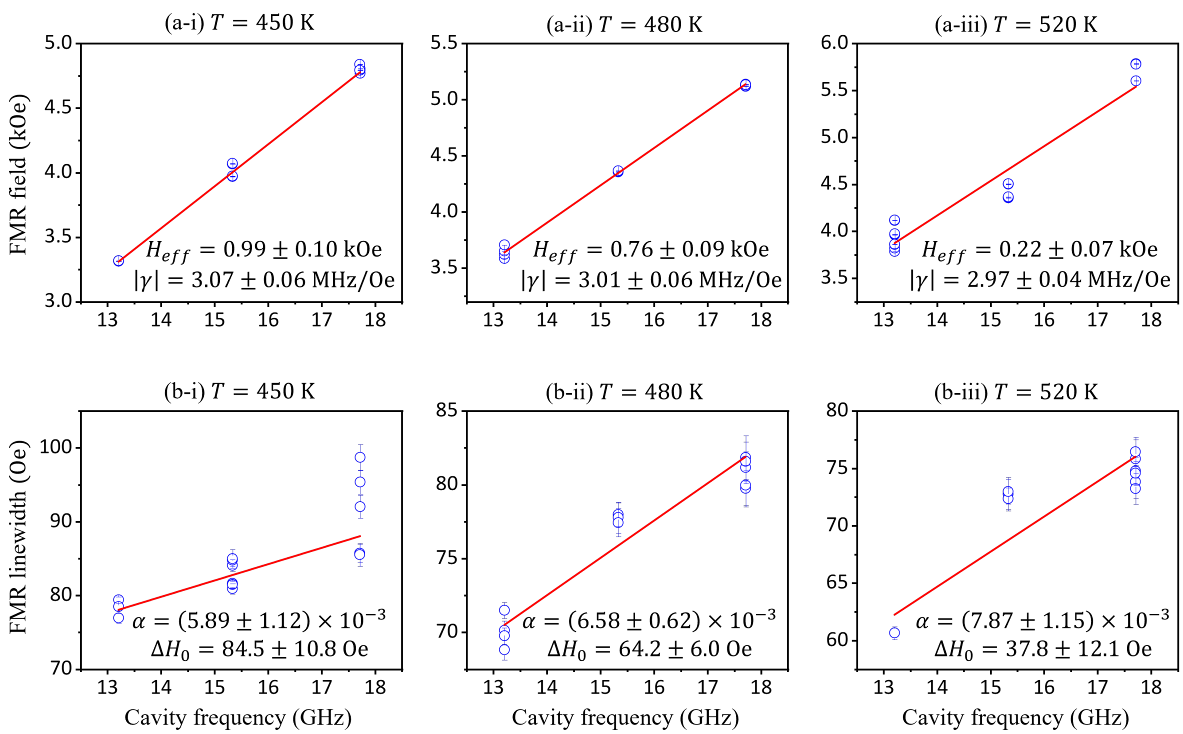

Figure 3.7: FMR properties of sample A at three different temperatures, as indicated. Graphs in the first row show the FMR fields H_{FMR} at different cavity frequencies f. Blue dots show the experimental data, while the red lines are numerical fits to (3.5). Graphs in the second row show the FMR linewidths ΔH at different cavity frequencies. Blue dots show the data and the red lines are fits to (3.6).

17.7 GHz data point excluded, but, in fact, it does include that data point. The fact that the fitting line strongly favors the low-frequency data points is because the uncertainties of the low-frequency points are smaller than the 17.7 GHz data point. This is also true for the fitting in Figure 3.7(b-i). Third, in Figure 3.8(b-ii) there are three data points for 17.3 GHz. The point with the relatively small uncertainty was measured first, while the other two with large uncertainties were collected in the repeated measurements for which the FMR signals were weaker. However, if the two points with large uncertainties were excluded during the fitting process, the resulting fit would not have notable changes.

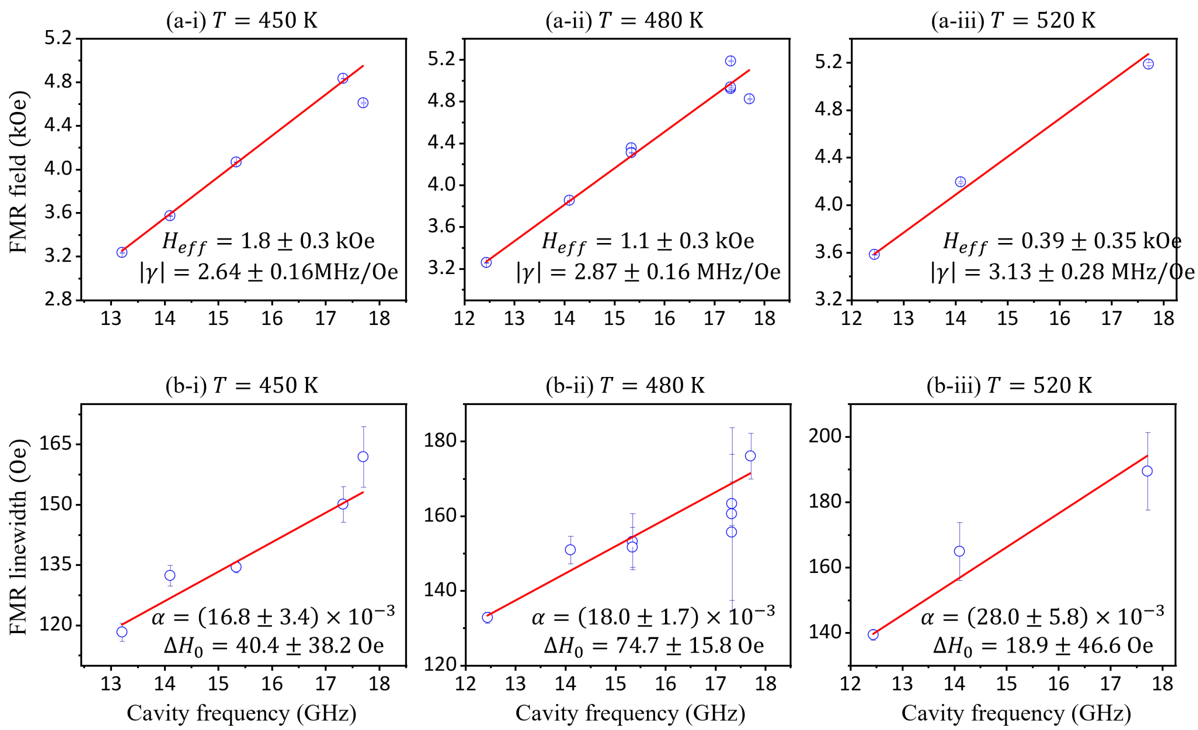

Figure 3.8: FMR properties of sample B at three different temperatures, as indicated. Graphs in the first row show the FMR fields H_{FMR} at different cavity frequencies f. Blue dots show the experimental data, while the red lines are numerical fits to (3.5). Graphs in the second row show the FMR linewidths ΔH at different cavity frequencies. Blue dots show the data and the red lines are fits to (3.6).

It should be mentioned that the absolute gyromagnetic ratios in Figure 3.7 and Figure 3.8 range from 2.64 MHz Oe^{-1} to 3.13 MHz Oe^{-1}. This range appears to be unreasonably wide, but this does not pose a problem because the uncertainties of those $|\gamma|$ values are high. The large uncertainties result mostly from the limited number of frequency points.

Consider now the H_{eff}, α,and ΔH_0 results obtained from the numerical fittings, such as those shown by the red lines in Figure 3.7 and Figure 3.8. Figure 3.9 presents the results. Graphs (a), (b), and (c) show α, H_{eff},and ΔH_0, respectively, as a function of the sample temperature T. In each graph, the blue and red symbols show the results for sample A and sample B, respectively. The values at $T = 300\,\text{K}$ are the same as those presented in Table 3.1 and Table 3.2. The values at $T = 520\,\text{K}$ are also listed in Table 3.1. The two arrows in graph (a) are drawn as guides for the eye to show the overall trends.

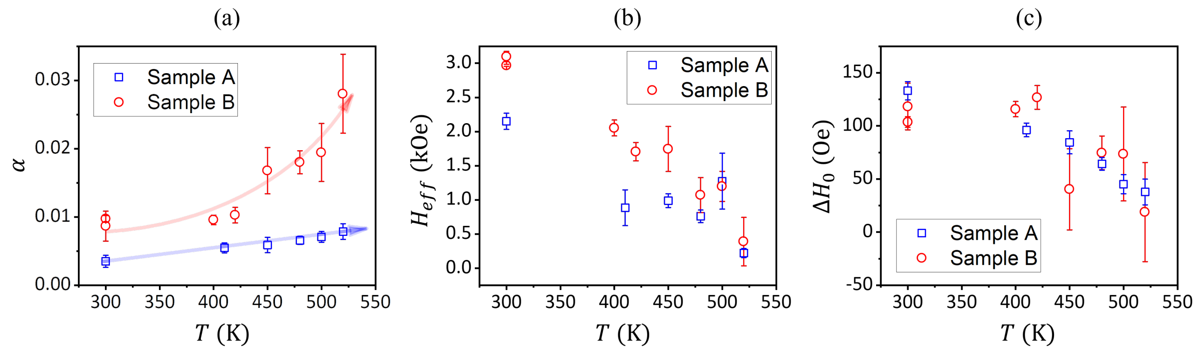

Figure 3.9: High-temperature FMR results of sample A and sample B. Graphs (a)-(c) show the Gilbert damping constant α; the effective anisotropy field H_{eff}; and the inhomogeneous line broadening ΔH_0 respectively, as a function of sample temperature T. Two arrows in graph (a) serve as guides for the eye to show the overall trends.

The damping values in Figure 3.9(a) show three key conclusions of this work: (1) over the entire temperature range, the damping constant, α, of sample A is smaller than that of sample B; (2) α increases with the temperature in both samples; and (3) the increase of α is relatively moderate in sample A but is more pronounced and seems to be exponential in sample B. The first conclusion explains why the switching current in the STT MRAM device made of the low-α free layer is lower than that in the device made of the conventional free layer [8]. As pointed out in Section 3.1, the critical current for switching scales linearly with the damping constant of the free layer; the smaller the damping is, the lower the switching current is. The first and third conclusions together clearly establish the technological advantage of sample A over sample B from the perspective of the STT MRAM application. The third conclusion is technologically important, because the operation of STT MRAM cells usually occurs above room temperature, as noted earlier.

To understand the physics underlying the three conclusions listed above, turn now to a discussion on the possible damping processes in the free-layer samples in this work. Generally speaking, a ferromagnetic thin film can host the following six damping processes: (1) magnonphonon scattering, (2) eddy-current-associated damping, (3) magnon-electron scattering associated with Fermisurface breathing, (4) spin-flip magnon-electron scattering (SF MES), (5) two-magnon scattering, and (6) spin pumping. Processes (1)-(4) are intrinsic, while processes (5) and (6) are extrinsic.

Magnon-phonon scattering occurs in all magnetic materials, but its contribution to the overall damping in a metallic thin film is usually much smaller than the contributions from the magnon-electron scattering processes [40]. The eddy-current-associated damping is nontrivial in relatively thick films [41]. For the free layers in this work, the thicknesses are substantially smaller than skin depth, and eddy-current-produced damping can therefore be neglected. The third damping process on the list is the Fermi-surface-breathing-associated magnon-electron scattering, which is often referred to as the intraband scattering [23], [24], [25], [26]. The damping associated with this scattering increases with a decrease in temperature. As a result, it is usually smaller than the damping produced by the SF MES above room temperature. The fourth one on the list is the SF-MES process, which is often referred to as interband scattering [23], [24], [25], [26]. This process involves both momentum and energy conservation, which can be more easily satisfied at higher temperatures. As such, damping due to the SF-MES process usually increases with an increase in temperature.

The two-magnon scattering, the fifth one on the list, involves the scattering of a uniform magnon to a nonuniform magnon by material imperfection; such imperfection includes grain misalignment, grain boundaries, line cracks, pores, and surface or interface roughness in the films [42], [43], [44], [45], [46]. This process, however, is absent in the free-layer samples in this work because the FMR experiments make use of perpendicular magnetic fields, as illustrated in Figure 3.3. In thin films magnetized perpendicularly, there are no degenerate spin-wave modes at the FMR frequency available for two-magnon scattering.

The spin-pumping process, the last one on the above list, involves the pumping of a pure spin current by the precessing moments in a magnetic thin film into a neighboring nonmagnetic metallic film. This process gives rise to a damping enhancement in the magnetic film, and such an enhancement can be substantial if the nonmagnetic film is made of a material with strong spin-orbit coupling, such as a heavy metal, a topological insulator, or a topological semimetal [47], [48], [49], [50], [51]. The W layers in the samples in this work are a heavy metal, but their thicknesses are substantially smaller than the spin-diffusion length. The nominal thicknesses of the W layers in sample A and sample B are 0.2 Å and 3 Å, respectively, while the spin-diffusion length in W ranges from 21 Å to 35 Å [52]. For this reason, the damping contribution due to spin pumping into the W layers is expected to be weak. Nevertheless, the W layers may produce some damping through enhanced spin-flip scattering at the interfaces; previous work has shown damping enhancement in CoFeB thin films due to neighboring ultrathin Ta films [53].

The above discussion indicates that, above room temperature, damping in the free layers in this work originates mainly from the SF-MES process, while the contributions from the other five mechanisms are either zero or relatively small. As mentioned earlier, the SF-MES process involves energy and momentum conservation, while the latter is easier to satisfy at high temperature. For this reason, the SF-MES-produced damping increases with an increase in temperature. This explains why α increases with T in Figure 3.9(a). The damping increase becomes more pronounced when the temperature is closer to T_C [25]. This justifies the larger increase in α for sample B than that for sample A. The T_C values for sample A and sample B are about 900 K and 650 K, respectively, so, in comparison with sample A, the temperature of sample B is closer to T_C. It is for the same reason that α in sample B is larger than that in sample A, as shown in Figure 3.9(a). The other minor reason for this difference is that in sample B there might be a small damping due to spin pumping from the magnetic layers to the W layer, while in sample A such damping is much smaller because the nominal thickness of the W layer (0.2 Å) is too small to form a continuous monolayer of W. Figure 3.10 shows the data from Figure 3.9(a) normalized to T_C, which emphasizes expected trend in damping due to the SF-MES process.

We turn now to the results presented in Figure 3.9(b) and 3.9(c). Though being scattered slightly, the data points in Figure 3.9(b) clearly show overall decreasing trends. As the sample temperature increases from 300 K to 520 K, the effective anisotropy field H_{eff} decreases from about 2.15 kOe to about 0.22 kOe in sample A and decreases from about 3.04 kOe to about 0.39 kOe in sample B. These values are consistent with those shown in Figure 3.2(b), and this agreement provides strong justification for the high-temperature FMR data. The data in Figure 3.9(c) show that, in both samples, the inhomogeneous line broadening ΔH_0 decreases with an increase in temperature. Since the decrease of the saturation magnetization, M_s, over the same temperature range is relatively moderate, as shown in Figure 3.2(a), the data in Figure 3.9(c) indicate that

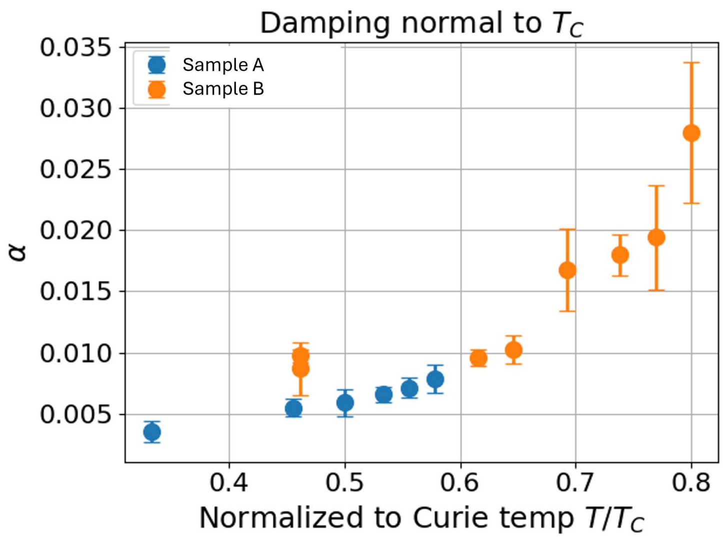

Figure 3.10: Measured α for each sample as a function of T/T_C.

ΔH_0 originates mostly from the spatial inhomogeneity of the anisotropy in the samples, not the inhomogeneity of magnetization.

3.7 Conclusion

With a microwave-cavity-based FMR system, high-temperature frequency-dependent FMR measurements have been carried out on two free-layer samples: a low-α free layer with split W layers and a conventional free layer with a single W layer. The measurements and analyses have yielded the following results for the high-temperature damping properties: (1) the damping constant of the low-α free layer is smaller than that of the conventional free layer over the entire temperature range from 300 K to 520 K; (2) the damping constant increases monotonically with temperature in both the low-α and conventional free layers; and (3) this damping increase is relatively modest and almost linear in the low-α free layer but is more pronounced and nearly exponential in the conventional free layer. These results clearly explain the experimental observation of smaller switching current in the STT MRAM device made of the low-α free layer than in that made of the conventional free layer [22]. They evidently establish the advantages and merits of the low-α free layer over the conventional free layer for the STT MRAM application.

The above-summarized results on damping can be interpreted in terms of the SF MES [23],

[24], [25], [26] and the difference of the Curie temperatures of the two free layers [22] The SF-MES process involves both momentum and energy conservation. Since such conservation is easier to satisfy at higher temperatures, the process becomes stronger and produces larger damping as the temperature is increased towards the Curie temperature. This is why the damping constants in both free layers increase monotonically as the temperature increases from 300 K to 520 K. On the other hand, the Curie temperature in the conventional free layer is much lower than that in the low-α free layer. As such, 520 K, the highest temperature in the FMR experiments, is closer to the Curie temperature in the conventional free layer than in the low-α free layer, and the damping increase in the conventional free layer is therefore more pronounced. This explains why the damping constant in the conventional free layer increases more rapidly and is also larger than in the low-α free layer.

In addition to the above damping results, the high-temperature FMR measurements have also yielded important information about the temperature dependence of the effective perpendicular anisotropy fields and inhomogeneous line broadening. The effective magnetic fields in the two free layers vary with temperature in the same quantitative manner as that found from the static magnetic measurements. This consistency provides clear justification for the high-temperature FMR data. As the temperature increases from 300 K to 520 K, the inhomogeneous line broadening decreases substantially in both free layers. This indicates that line broadening originates mainly from the spatial inhomogeneity of the perpendicular anisotropy in the samples, because magnetization decreases over the same temperature range are modest, according to static magnetic measurements.

Chapter 4. Spin Waves

Ferromagnetic resonance is the uniform mode of a more general phenomena in magnetic media called a spin wave. A spin wave is a propagating excitation of a coupled spin system. The quanta of spin waves are called magnons. Spin waves have appealing properties for fundamental physics, particularly of nonlinear systems, and for computing, where spin-wave logic could be used to complement or as an alternative to existing electronics (a field called spintronics or magnonics).

One appealing property of spin waves is that their dispersion relations are a function of the magnetic environment, and therefore can be precisely tuned. Further tunability is possible with engineered waveguides called magnonic crystals, as will be discussed. Spin waves have a broad bandwidth up to hundreds of THz. Spin wave research has primarily been academic, but has recent attention related to communications and magnonics applications [54]. In rf communications, spin wave devices are a proposed alternative to high-frequency (above 10 GHz) passive devices, with distinct advantages over current surface acoustic wave designs [55].

4.1 Magnetostatic Spin Waves

4.1.1 Walker's Equation

Consider a uniform plane wave propagating through a magnetized ferrite. Maxwell's cross products, (1.3) and (1.4), become

$$\mathbf{k} \times \mathbf{h} = -\omega\varepsilon\mathbf{e}, \tag{4.1}$$

$$\mathbf{k} \times \mathbf{e} = \omega\mu_0(\mathbf{h} + \mathbf{m}). \tag{4.2}$$

This has utilized a time dependece of the form $\exp(i\omega t)$, and a spatial dependence of the form $\exp(i\mathbf{k}\cdot\mathbf{r})$, which allows $\nabla \to i\mathbf{k}$. Further analysis yields three equations of interest:

$$\mathbf{h} = \frac{k_0^2\mathbf{m} - \mathbf{k}\mathbf{k}\cdot\mathbf{m}}{k^2 - k_0^2}, \tag{4.3}$$

$$\mathbf{e} = \frac{\omega\mu_0\mathbf{k}\times\mathbf{m}}{k_0^2 - k^2}, \tag{4.4}$$

$$\nabla\times\mathbf{h} = -\frac{k_0^2\mathbf{k}\times\mathbf{m}}{k_0^2 - k^2}, \tag{4.5}$$

where $k_0^2 = \omega^2\mu_0\varepsilon$ is the free-space wavenumber. For $|k|$ much larger or much smaller than k_0, it is seen that h remains finite, but e and $\nabla\times\mathbf{h}$ go to zero. So, to first order,

$$\nabla\times\mathbf{h} = 0, \tag{4.6}$$

$$\nabla\cdot\mathbf{b} = 0, \tag{4.7}$$

$$\nabla\times\mathbf{e} = i\omega\mathbf{b}. \tag{4.8}$$

These three equations define the magnetostatic approximation to Maxwell's equations. Taking this a step further, we come to a general solution for an arbitrary magnetostatic scalar potential, ψ, called Walker's equation.

$$(1+\chi)\left[\frac{\partial^2\psi}{\partial x^2} + \frac{\partial^2\psi}{\partial y^2}\right] + \frac{\partial^2\psi}{\partial z^2} = 0, \tag{4.9}$$

where

$$\chi = \frac{\omega_0\omega_M}{\omega_0^2 - \omega^2} \tag{4.10}$$

is a component of the susceptibility tensor, $\mathbf{M} = \chi\cdot\mathbf{H}$, when time-varying $\mathbf{m}$ and $\mathbf{h}$ are included. Walker's equation is the base equation for magnetostatic wave modes in homogeneous media. Assuming a scalar potential proportional to a plane wave, the solution is

$$\omega = \sqrt{\omega_0\left(\omega_0 + \omega_M\sin^2\theta\right)}. \tag{4.11}$$

This solution is independent of k without considerations of boundary conditions or the exchange interaction, but it does define via θ an allowed region for spin waves called the spin wave manifold:

$$\omega_H \leq \omega \leq \omega_B, \tag{4.12}$$

where

$$\omega_H = \omega_0 = \mu_0 \left|\gamma\right| H, \tag{4.13}$$

$$\omega_B = \sqrt{\omega_0 \left(\omega_0 + \omega_M\right)} = \mu_0 \left|\gamma\right| \sqrt{H \left(H + M_s\right)}, \tag{4.14}$$

and H is the net strength of the internal static field—usually consisting of the applied dc bias field, the anisotropy field, and the demagnetization field.

4.1.2 Spin Wave Mode Families

The characteristics of a propagating spin wave are dependent on two parameters. The first is the dominating interaction between spin sites. At very low $|k|$, electric and magnetic dipolar interactions are both relevant. At very high $|k|$, exchange interactions dominate. "Magnetostatic waves" typically refer to the middle region, where dipolar interactions dominate, though the magnetostatic approximation may be valid outside of this region. These waves have wavenumbers on the order of hundreds of radians per centimeter,[10] corresponding to wavelengths like hundreds of micrometers.

The second defining parameter is the orientation of an applied dc bias field relative to that of the wave propagation. This parameter categorizes spin wave modes into three distinct mode families with different wave properties. Figure 4.1 plots the dispersion relation against linear frequency of the lowest-order mode for each of these families in a thin film, showing clearly the top-level differences. The waves are differentiated by the sign of the group velocity, $v_g = d\omega/dk$, and the dispersion coefficient, $D = d^2\omega/dk^2$. At high k, each of these modes will show a dramatic upturn.

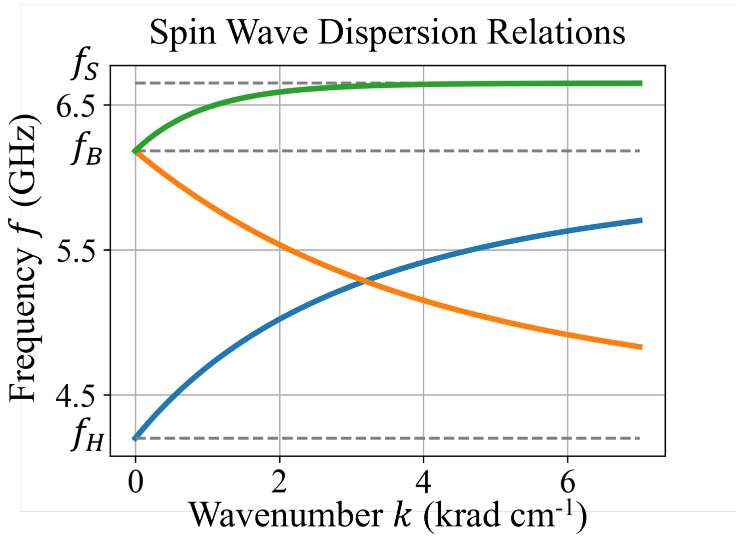

Figure 4.1: Dispersion relations for a thin-film sample with $t = 5\,\mu\text{m}$, $H = 1500\,\text{Oe}$, and $4\pi M_s = 1750\,\text{G}$.

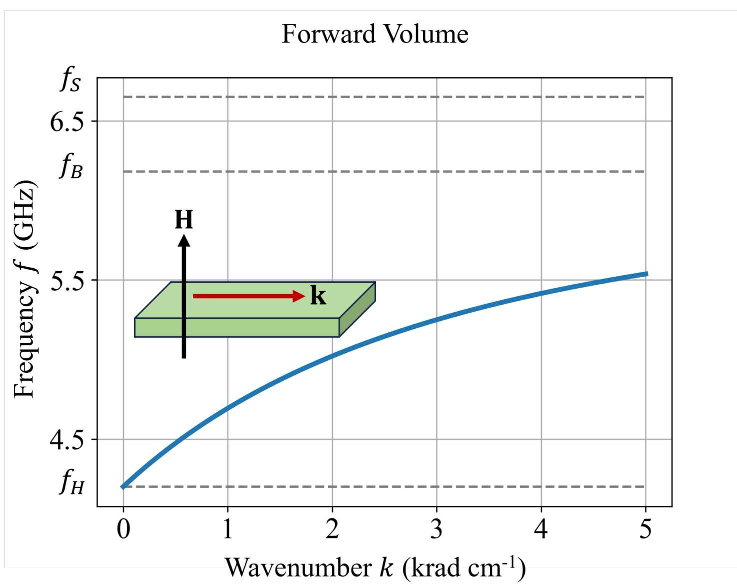

Figure 4.2: Forward-volume magnetostatic spin wave dispersion in a thin film. The applied field is perpendicular to the film surface normal.

Forward Volume Waves

Forward volume magnetostatic spin waves (FVMSW or FVW) are excited when the applied field is perpendicular to the film surface. The group velocity is positive, hence the "forward" label, and the dispersion coefficient is negative. The wave is bound by the spin-wave manifold defined in (4.12). For a thin film, this field orientation includes a demagnetizing field, so the effective field $H = H_0 - M_s$. The wave amplitude is distributed sinusoidally as standing spin wave modes through the film thickness, hence the "volume" label, and higher-order modes (called thickness modes) are defined by higher-order standing waves. The higher-order modes are typically very weak. An appoximation to the lowest-order dispersion relation was derived by Kalinikos [7]:

$$\omega(k) = \sqrt{\omega_H \left[\omega_H + \omega_M \left(1 - \frac{1 - e^{-kt}}{kt}\right)\right]}, \tag{4.15}$$

where the field frequency substitution (2.11) has been used for the applied field, H and saturation magnetization, M_s.

Backward Volume Waves

Backward volume magnetostatic spin waves (BVMSW or BVW) are excited when the applied field is parallel to both the film surface and the direction of propagation. Compared to FVWs, they are bound by the same spin-wave manifold frequencies, but the bounds are reversed for low and high k. The group velocity and dispersion coefficient are also reversed. The "backward" label indicates that the group velocity and phase velocity, $v_p = \omega/k$, are of opposite sign—the wave envelope and wave packet move opposite to each other. Also similar to FVWs, the wave amplitude is distributed sinusoidally through the film thickness, and those sinusoids describe the thickness mode of the wave. An approximation for the lowest-order BVW mode (also from Kalinikos) is:

$$\omega(k) = \sqrt{\omega_H \left[\omega_H + \omega_M \left(\frac{1 - e^{-kt}}{kt}\right)\right]}. \tag{4.16}$$

This orientation has no demagnetizing field, so H is purely from the applied field.

[10] This section will present spin waves using cgs units.

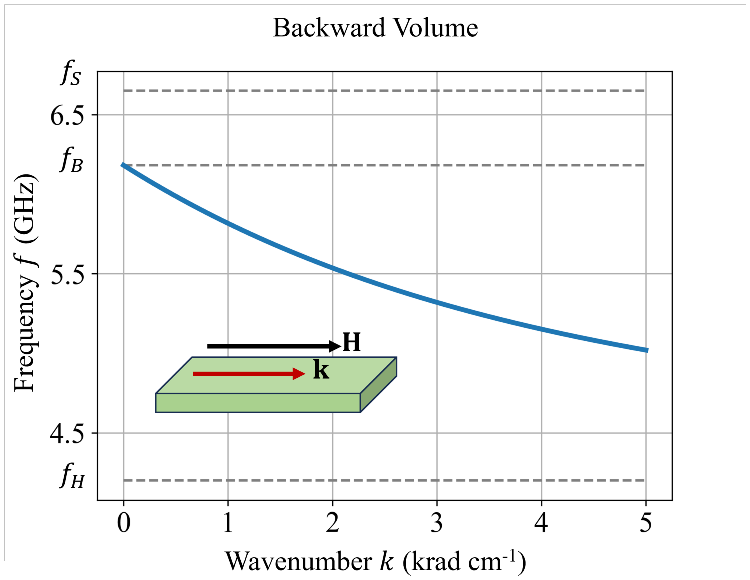

Figure 4.3: Backward-volume magnetostatic spin wave dispersion in a thin film. The applied field is in-plane with the film and parallel to the direction of wave propagation.

Surface Waves

Magnetostatic surface spin waves (MSSW, SSW, or SW) are excited when the applied field is parallel to the film surface and perpendicular to the direction of propagation. The shape of the dispersion curve (and thus v_g and D) is the same as for FVWs; however, the frequency is bound above the manifold as

$$\omega_B \leq \omega \leq \omega_S = |\gamma| \, (H + M_s/2). \tag{4.17}$$

Unlike the volume modes, SSW have only one propagating mode. Its amplitude is a maximum at the film surface and decays exponentially into the bulk of the film. Additionally, the mode is nonreciprocal when the propagation direction is reversed: the mode will propagate on the surface with respect to a right-hand rule around the applied field. The exact dispersion relation is calculated to be [7]

$$\omega(k) = \sqrt{\omega_H \, (\omega_H + \omega_M) + \frac{\omega_M^2}{4} \, (1 - e^{-2kt})}. \tag{4.18}$$

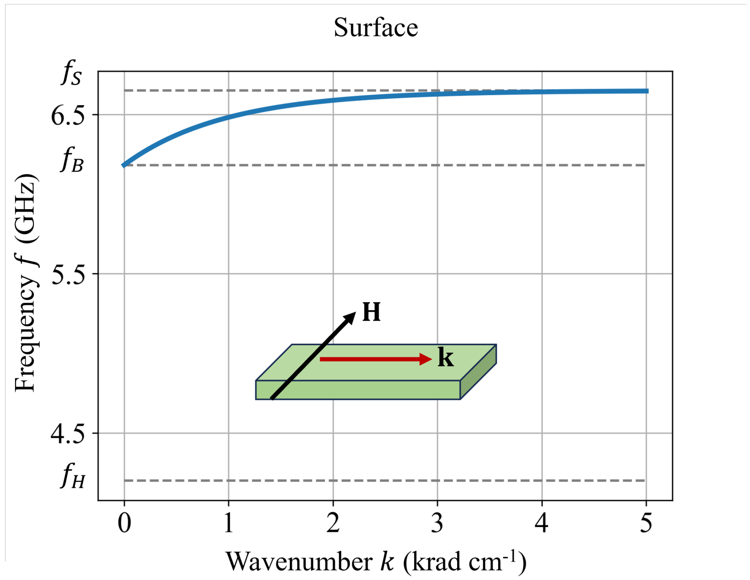

Figure 4.4: Magnetostatic surface spin wave dispersion in a thin film. The applied field is in-plane with the film and perpendicular to the direction of wave propagation.

4.2 Vector Network Analyzer Spin-Wave Measurements

A straightforward method of measuring spin-wave dispersion and propagation is to use a two-port vector network analyzer (VNA) to measure the transmission and phase delay across the spin-wave waveguide. These are the magnitude and phase components of the complex scattering parameter, S, measured across the sample. An illustration of the measurement setup is shown in Figure 4.6. Port 1 (J_1) of the VNA is connected to a transducer antenna, which is separated by a distance s to a receiving transducer connected to port 2 (J_2). The excited wave, $\mathbf{k}$, will travel in the direction from J_1 to J_2. The magnetic sample is placed flip-chip across the two transducers. A dc magnetic field, $\mathbf{H}_0$, is applied and oriented with respect to $\mathbf{k}$ to excite the desired spin wave mode family. An rf signal from the VNA creates a magnetic field around the transducer antenna, exciting the spin wave, and the opposite conversion happens at the other transducer. The measurement at J_2 shows the amplitude and phase difference of the voltage ratio, S_{21} ("at 2 from 1").

The wavenumber in the sample is different than of that in the VNA leads, so the measured phase change across the structure corresponds directly to the wavenumber k of the spin wave as

$$k(f) = \frac{\phi(f) - \phi_0}{s}, \tag{4.19}$$

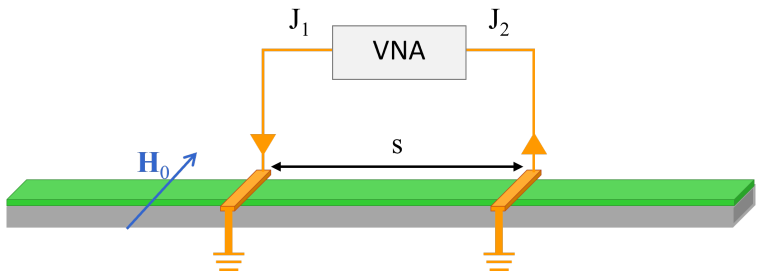

Figure 4.5: Transducer spin-wave measurement setup. The signal from J_1 excites a propagating spin wave that is measured at J_2. The setup is within a uniform applied magnetic field $\mathbf{H}_0$. Its orientation with the film determines the type of spin wave.

where $\phi(f)$ is the phase measured at a frequency f and ϕ_0 is the phase offset at the beginning of the spin wave signal. An example measurement of a surface spin wave is shown in Figure 4.6. Plotted against frequency f is the S_{21} transmission amplitude in blue and the cumulative phase in red. The dashed black line marks f_B, the beginning of the wave, which is determined observationally using a notable change in the phase, the beginning of the jump in transmission amplitude, and against the calculated value for f_H using (4.18). At frequencies below the wave, the signal consists of instrument noise, off-axis modes (i.e., backward volume waves), and/or excitations outside of the magnetostatic approximation.

The decaying spin-wave signal is attributed to two mechanisms. The first is the decay of the spin wave itself, which is proportional to the group velocity and damping. The decay term looks like

$$\exp\left(-\eta s / v_g\right), \tag{4.20}$$

where $\eta \propto \alpha\omega$. The second source of decay is the filtering effect of the transducers, which is a function of transducer width, w. A Fourier transform of the field strength in space shows that in k-space the field is zero at $k = \pi/w$. For $w = 50\,\mu\mathrm{m}$, this corresponds to $k \approx 600\,\mathrm{rad\,cm^{-1}}$.

4.3 Magnonic crystals

A magnonic crystal[11] is a periodic multilayered magnetic structure, where the different layers have different magnetic properties, i.e., magnetizations. Spin-wave transmission through magnonic crystals is modified by these variations, resulting in unique dispersion curves compared to in uniform

[11]The term "magnonic crystal" is in analogy with photonic crystals, which have varying indices of refractivity.

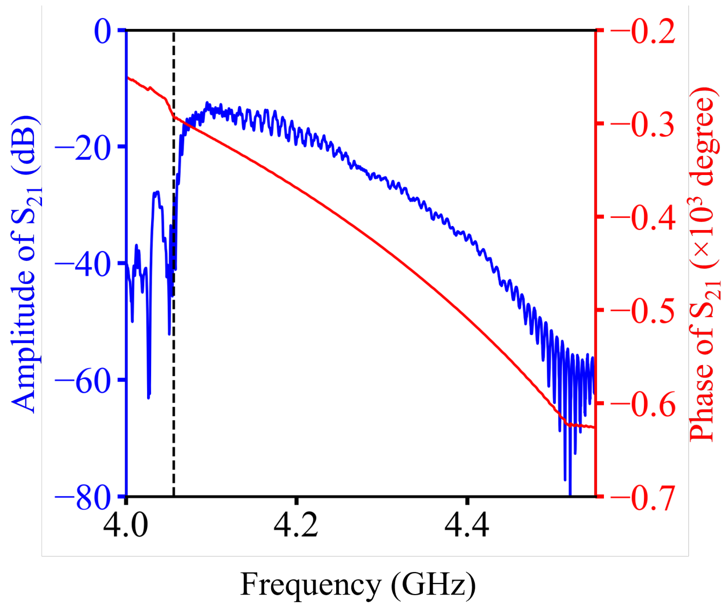

Figure 4.6: A transducer measurement of a magnetostatic surface spin wave. The dashed black line denotes the beginning of the wave, f_B. The blue line (left axis) is the amplitude in decibels of the complex transmission S_{21}, and the red line (right axis) is the cumulative phase in thousands of degrees.

media. Most immediately relevant is the introduction of band gaps at frequencies/wavenumbers where the spin wave is forbidden to propagate, due to destructive reflective interference. The simplest application of a magnonic crystal is as a spin-wave filter, taking advantage of that interference, but magnonic crystals constitute a key element in spintronic devices [56] and in nonlinear spin-wave research [14].

The periodicity defining a magnonic crystal can be realized in numerous ways. One can physically remove material from a uniform material by mechanical or chemical means, introduce additional fields via contact with current-carrying wires or other materials, or create a bona fide multilayer structure. The devices constructed in Chapter 5 are chemically etched to remove material from YIG thin films. More detail about the process is contained in that chapter.

The design of magnonic crystals in one dimension is well-documented. Previous work by Chumak [57] and Qin [58], among others, characterize the pass band and rejection band signals for different lattice spacings and groove dimensions. The results from the referenced publications are summarized in Table 4.1. One key takeaway from the data is the feasibility of miniaturized magnonic crystals, facilitating their integration with existing electronics.

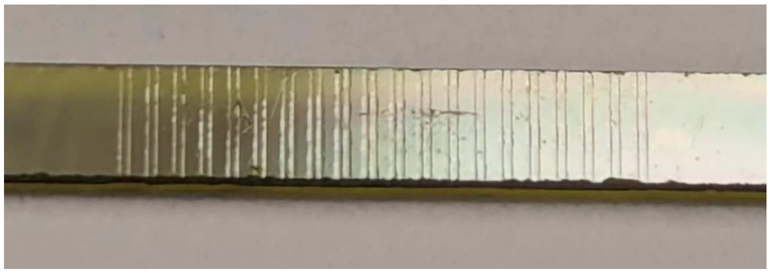

Figure 4.7: A magnonic crystal made from etching grooves into a YIG thin film. Each line across the strip is a groove.

Table 4.1: Summarized, quantitative results from work by Chumak [57] and Qin [58] exploring the parameter space of magnonic crystals. The effect of increasing the parameter in the leftmost column is indicated by arrows, where up/down arrows represent an increase/decrease in the column value. The number of arrows represent the magnitude of change from slight (one arrow) to great (three arrows). The rightmost column specifies the type of spin wave that was measured.

Increased parameter	Loss of rejection band	Signal of passband	Width of rejection band	Wave measured
Lattice spacing	↓↓	↑↑	↓↓	SSW
Film thickness	—	↑↑	↑↑	BVW, SSW
Relative groove depth	↑↑	↓	↑	BVW
Groove width	↑↑↑	↓↓	↑	BVW
Number of grooves	↑↑	↓	↑	BVW
CoFeB filled grooves	—	—	↑↑	SSW

Chapter 5. Spin Wave Propagation in Magnonic Crystals

5.1 Introduction

A magnonic crystal is an engineered magnetic material with periodically modulated magnetic properties. These spatial periodic variations give rise to Bragg reflections or scattering and thereby create band gaps for spin waves in the material. These band gaps occur at frequencies corresponding to the Bragg wavenumbers—the wavenumbers at which Bragg reflection occurs. The rich features associated with these band gaps have facilitated the study of intriguing physics that are otherwise inaccessible with spin waves in continuous media. Examples include the experimental observation of spin-wave soliton fractals in one-dimensional (1D) magnonic crystals [59] and the theoretical prediction of topological magnons in two-dimensional (2D) magnonic crystals. [60], [61]

Previous work on 1D magnonic crystals has predominantly focused on structures with single periodicity. [59], [62], [63], [64], [65], [66], [67], [68] The bandgaps in such materials exhibit similar properties, as expected according to Bragg's law. In an effort to develop strategies for tailoring band gaps, this study examines the band gap properties in a 1D magnonic crystal with double periodicity. A long and narrow yttrium iron garnet (YIG, $Y_3Fe_5O_{12}$) thin film strip is etched with an array of transverse line grooves whose separation alternates between a_1 and $a_2 = 2a_1$. This double periodicity in the spatial domain translates into dissimilar transmission dips in the frequency domain, with the third and sixth transmission dips being broader and deeper than others. These results indicate that every third band gap is more pronounced. The underlying reason is that the wavenumbers corresponding to those band gaps simultaneously satisfy the Bragg conditions for the periods a_1, a_2, and $a_1 + a_2$. The experimental observations are reproduced by simulations using a transfer matrix method. The experimental and numerical results together demonstrate an effective strategy for creating magnonic crystals with desired band properties for both fundamental research and device applications. From a fundamental perspective, for example, magnonic crystals with broad band gaps ease the experimental investigation of in-gap modes. Practically, magnonic

Table 5.1: Properties of three samples: a uniform YIG thin film strip, a singly periodic YIG-based magnonic crystal, and a doubly periodic YIG-based magnonic crystal.

Properties	Uniform YIG strip	Singly periodic magnonic crystal	Doubly periodic magnonic crystal
Sample width (mm)	1.91	1.99	1.98
Sample length (mm)	17.4	17.8	22.6
Film thickness (µm)	10.5	12.7	4.2
Groove count	–	31	40 (20 pairs)
Groove spacing (µm)	–	400 ± 4	$a_1 = 149 \pm 10$ $a_2 = 300 \pm 12$
Groove depth (µm)	–	1.16 ± 0.02	0.84 ± 0.03
Groove width - top (µm)	–	103 ± 2	65 ± 15
Groove width - bottom (µm)	–	42 ± 2	27 ± 1
Saturation induction (G)	1898	1926	1790

crystals with varying band gaps can enable easy switching between different types of microwave filtering operations.

5.2 Sample Preparation

This study made use of three samples: (1) an un-patterned or uniform YIG thin film strip, (2) a singly periodic magnonic crystal, and (3) a doubly periodic magnonic crystal. The magnonic crystals were created through etching arrays of transverse line grooves on the top surfaces of long and narrow YIG thin film strips. For all the samples, the YIG films were grown on (111)-oriented single-crystal gadolinium gallium garnet (GGG, $Gd_3Ga_5O_{12}$) substrates by liquid phase epitaxy. The fabrication of the line grooves involved pattern formation through a laser writing-based lithography process (using AZ 1512 photoresist) and the chemical etching of exposed YIG surfaces by hot acid.

The exposed sections of the YIG strips were chemically etched by submerging the samples in hot H_3PO_4. The etching rate is controlled by varying the acid temperature and was approximately 10 nm/s at 160 °C, which is comparable with values reported previously. [64], [67] The temperature uniformity of the acid is critical for an even etching. To ensure good temperature uniformity, the beaker was submerged in a bead bath of alumina pellets. After etching, samples were cut to desired dimensions using a diamond wire saw and the photoresist was then removed in an acetone bath using an ultrasonic cleaner. Fuller details on the etching process are provided in Appendix 8.

Table 5.1 lists the properties of the three samples. The groove properties were determined through surface profile measurements using a Bruker Dektak XT stylus profilometer. Figure 5.1 shows a portion of the surface profile together with an optical microscope image for each magnonic crystal sample. The singly periodic sample has a lattice constant $a = 400\,\mu m$ that is defined as the distance between the falling edge of one groove to the falling edge of the next. There are 31 identical grooves in total, spanning a total length of 12.1 mm. Each groove is wider at the top than at the bottom, as can be seen in Fig. 5.1(a), with the top width of about 103 um and the bottom width of about 42 µm. The average groove depth is about 1.16 µm.

As shown in Figs. 5.1(b) and 5.1(c), the doubly periodic sample has alternating groove separations: $a_1 = 149\,\mu m$ and $a_2 = 300\,\mu m$, which are also measured from falling edge to falling edge. There are 40 grooves in total, spanning a length of 8.7 mm. Each groove is about 65 µm wide across the top and 27 µm wide across the bottom. The slope of the falling and rising edges of the grooves is about 0.054, according to Fig. 5.1(c). The average groove depth is about 0.84 µm. This sample could be equivalently defined by a "super-lattice" of grooves, where two lattices, each with a lattice constant $a_3 = a_1 + a_2$, are offset by a distance equal to a_1.

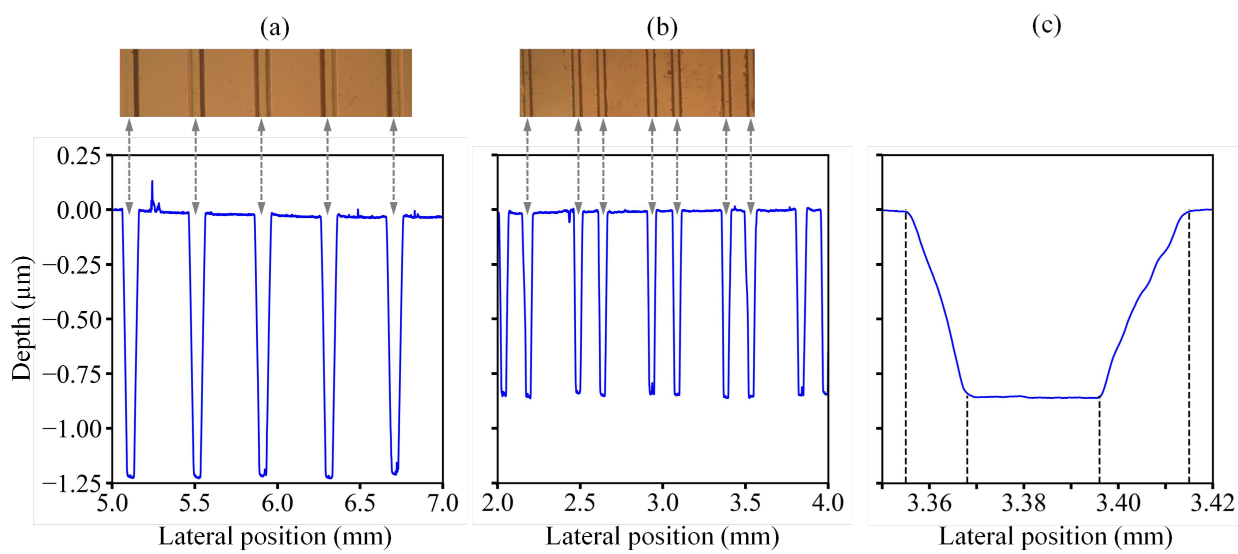

Figure 5.1: Profilometer measurements of the two etched YIG strips across a length of 2.0 mm. (a) Depth profile of a singly periodic magnonic crystal that shows five grooves with depths of about 1.16 µm. The slight slope of the top surface is due to a small misalignment of the profilometer stage. (b) Depth profile of a doubly periodic magnonic crystal that shows five pairs of grooves with depths about 0.84 µm. The images on the top are the corresponding microscope pictures of the samples. (c) Expanded view of the 7th groove in (b).

The film thicknesses (t) listed in Table 5.1 were determined through scanning electron microscopy (SEM) measurements using a ThermoFisher "Scios 2 DualBeam" system. The saturation induction ($4\pi M_s$) values were determined through the numerical fitting of the experimentally measured spin wave dispersion curves to the theoretical dispersion relation. Such fitting is described in Section 5.3.

5.3 Experiment and Analysis Approaches

The spin-wave experiments on each sample were carried out through the placement of two microstrip transducers on the sample and the measurement of the transmission coefficient S_{21} across the two transducers by a vector network analyzer (VNA), as illustrated schematically in Fig. 5.2(a). Each transducer is a $50\,\Omega$ wide, end-shorted strip line with a nominal impedance of $50\,\Omega$. The separation of the two transducers, denoted by l, is less than the full span of the grooves. The sample is magnetized to saturation by an external magnetic field (H_0) that is applied in the plane of the YIG film or the magnonic crystal and is perpendicular to the sample length direction. This field configuration supports the propagation of magnetostatic surface waves (MSSWs) within the sample. For all the data presented below, the field direction was set to ensure that spin waves travel on the top surfaces of the samples. This means that, for the magnonic crystal samples, the waves propagate along the YIG surfaces etched with grooves, rather than the surfaces interfacing with the GGG substrates. Reversing the field direction would result in spin-wave propagation along the surfaces interfacing with the GGG substrates, consistent with the chirality of the MSSWs. [69], [70], [71] This reversed configuration produces notably weaker and noisier S_{21} responses.

The amplitude and phase of the complex transmission coefficient S_{21} are both measured. The phase (ϕ) measured as a function of frequency (f) can be expressed as $\phi(f) = k(f)l + \phi_0$, where k is the wavenumber of the spin wave, $k(f)l$ denotes the phase of the spin wave accumulated during its propagation from the excitation transducer to the detection transducer, and ϕ_0 is the phase associated with the electric components, such as the microwave cables and the connectors. As such, the measurement of $\phi(f)$ allows for the determination of the dispersion $k(f)$ of the spin wave as

$$k(f) = \frac{\phi(f) - \phi_0}{l}. \tag{5.1}$$

Note that the wavenumber is taken to be positive, which may require taking the absolute value of the numerator in (5.1) depending on how the VNA measures the phase.

The theoretical dispersion for an MSSW in a thin film takes the form [69], [72]

$$f(k) = \frac{|\gamma|}{2\pi}\sqrt{H_0\left(H_0 + 4\pi M_s\right) + \frac{1}{4}\left(4\pi M_s\right)^2\left(1 - e^{-2kt}\right)}, \tag{5.2}$$

where $\frac{|\gamma|}{2\pi} = 2.8\,\mathrm{MHz/Oe}$ is the absolute gyromagnetic ratio, $4\pi M_s$ is the saturation induction, and t is the film thickness. According to (5.2), the $f(k)$ curve increases monotonically between the bounds $f_B = \frac{|\gamma|}{2\pi}\sqrt{H_0\left(H_0 + 4\pi M_s\right)}$ and $f_S = \frac{|\gamma|}{2\pi}\left(H_0 + \frac{1}{2}4\pi M_s\right)$, where f_B and f_S are the frequencies in the limits of $k = 0$ and $k \to \inf$, respectively. Note that f_B is the Kittel equation describing the ferromagnetic resonance (FMR) frequency of the film under an in-plane field. In practice, with an increase of f, the spin-wave signal measured by the detection transducer will have decayed to the noise floor at a frequency below f_S. The primary source of this decay is associated with the spin-wave group velocity defined as $v_g = \frac{d(2\pi f)}{dk}$. In a simplified picture, one can express the spin-wave decay factor as $e^(-\eta l v_g)$, where the decay rate η scales with the Gilbert damping constant: a dimensionless parameter measuring magnetic relaxation in a material. As f is increased towards f_S or k approaches infinity, v_g approaches zero according to (5.2) and $e^(-\eta l v_g)$ therefore also approaches zero. A second source is from the filtering effect of the microstrip transducers: the excitation and detection efficiencies of the transducers are relatively high at low k but decrease with an increase in k. [73]

In this work, (5.1) is used to determine the experimental dispersion curve, and (5.2) is then used to fit it. The numerical fitting yields an effective $4\pi M_s$ value for the sample. Such values are presented in the last row of Table 5.1.

To demonstrate this analysis process, Figures 5.2(b) and 5.2(c) show experimental data and numerical fitting for the uniform YIG strip. Figure 5.2(b) presents the S_{21} data measured as a function of f under a magnetic field of $H_0 = 782\,\mathrm{Oe}$. The blue and red profiles show the amplitude and phase of S_{21}, respectively. The vertical dashed line marks the FMR frequency, indicated by f_B which is defined above. One can see that as f increases, the S_{21} amplitude decays, as explained earlier.

Figure 5.2(c) shows the spin-wave dispersion. The solid blue curve is the experimental dispersion

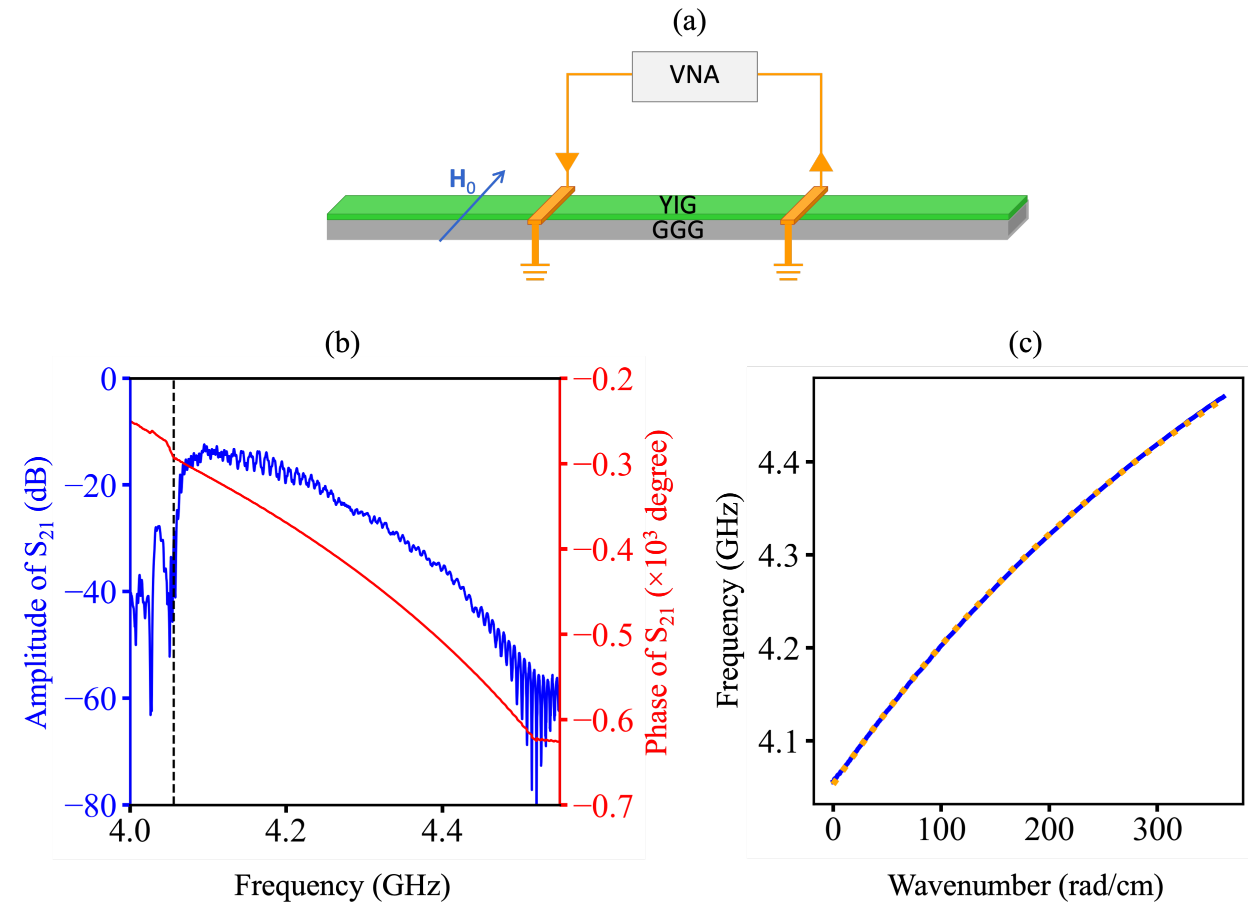

Figure 5.2: Spin waves in a uniform YIG film strip. (a) Experimental configuration. (b) Transmission coefficient S_{21} of a transducer/YIG/transducer structure measured under a magnetic field of $H_0 = 782\,\mathrm{Oe}$ applied in the film plane and perpendicular to the YIG strip length. The blue and red profiles show the amplitude and phase of S_{21}, respectively, as a function of frequency. The dashed black line marks the FMR frequency. (c) Dispersion relation of the spin wave. The solid blue curve shows the dispersion obtained from the phase profile in (a), while the dotted orange curve is a numerical fit to (5.2).

curve obtained from the phase profile in Fig. 5.2(b) by the use of (5.1). One can see that f increases with k monotonically with a negative curvature, as expected. [72] The dotted orange curve is a fit to (5.2) using Python and the "curve_fit" method in the SciPy library. The fitting yields an effective saturation induction of $4\pi M_s = (1897.7 \pm 0.1)$ G and a film thickness of $t = (9.607 \pm 0.003)$ µm. The thickness value here is slightly smaller than the value in Table 5.1 (10.5 µm) which was obtained from the SEM measurement. This difference is likely due to the uncertainty of the thickness measurement associated with the quality of the SEM image. If the film thickness is kept constant at 10.5 µm and $4\pi M_s$ is the only free parameter, the fitting yields a similar curve with $4\pi M_s = (1881.0 \pm 0.2)$ G which is slightly smaller and suggests that the thickness parameter is relatively insensitive to the order of a micrometer.

5.4 Experimental Results

Figures 5.3 and 5.4 present the main experimental data of this work. Figure 5.3 fives the S_{21} data in (a) and (b), the dispersion data in (c), and the Bragg wavenumbers in (d) for the singly periodic magnonic crystal. The format of Fig. 5.3(a) is the same as that of Fig. 5.2(b)—the blue and red profiles show the amplitude and phase, respectively, of S_{21} measured as a function of f. Figure 5.3(b) presents the same data as Fig. 5.3(a) but provides a zoomned-in view over a narrow frequency range around the third dip in Fig. 5.3(a). The format of Fig. 5.3(c) is the same as that of Fig. 2(c)—the blue solid curve shows the dispersion obtained from the phase data in Fig. 5.3(a) using (5.1), while the orange dotted curve shows the numerical fit to (5.2). The insert in Fig. 5.3(c) gives a zoomed-in view of the dispersion near the frequency of the third dip in Fig. 5.3(a). In contrast to the data presented in Figs. 5.2(b) and 5.2(c) for the uniform YIG strip, the data in Figs. 5.3(a), 5.3(b), and 5.3(c) show characteristic dips in the amplitude profile, as indicated by the vertical arrows, and phase and dispersion jumps exactly at the center frequencies of the dips.

The transmission dips and the corresponding phase and dispersion jumps shown in Figs. 5.3(a), 5.3(b), and 5.3(c) are indications of the formation of the band gaps for the spin waves in the magnonic crystal. The wavenumbers associated with the centers of the band gaps satisfy the Bragg condition

$$k_n a = n\pi \tag{5.3}$$

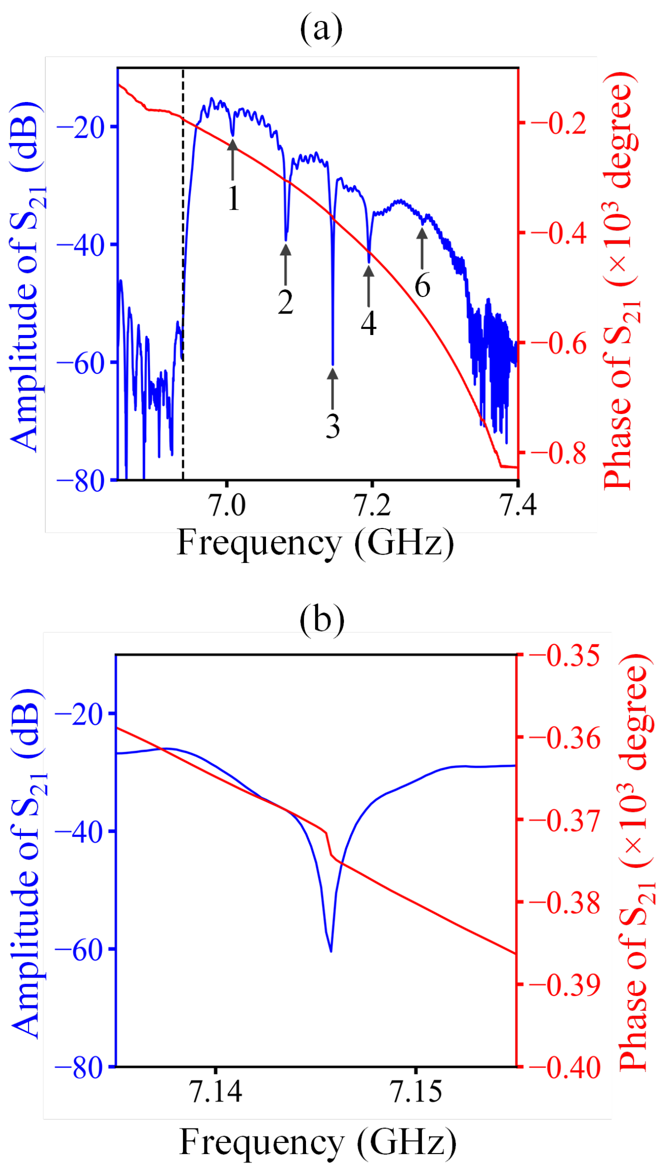

Figure 5.3: Spin waves in a singly periodic magnonic crystal, with a period of $a = 400\,\mu$m. (a) Transmission coefficient S_{21} of the magnonic crystal measured under a field of $H_0 = 1690$ Oe applied in the sample plane and perpendicular to the sample length direction. The blue and red profiles show the amplitude and phase of S_{21}, respectively, as a function of frequency. The dashed black line marks the FMR frequency. The short vertical arrows point to the centers of the band gaps. (b) Zoomed-in view of (a) near the third band gap. (c) Dispersion curve. The blue curve shows the measured dispersion response while the orange dotted curve is a numerical fit. (d) Measured Bragg wavenumbers (blue points) compared to calculated Bragg wavenumbers (red squares).

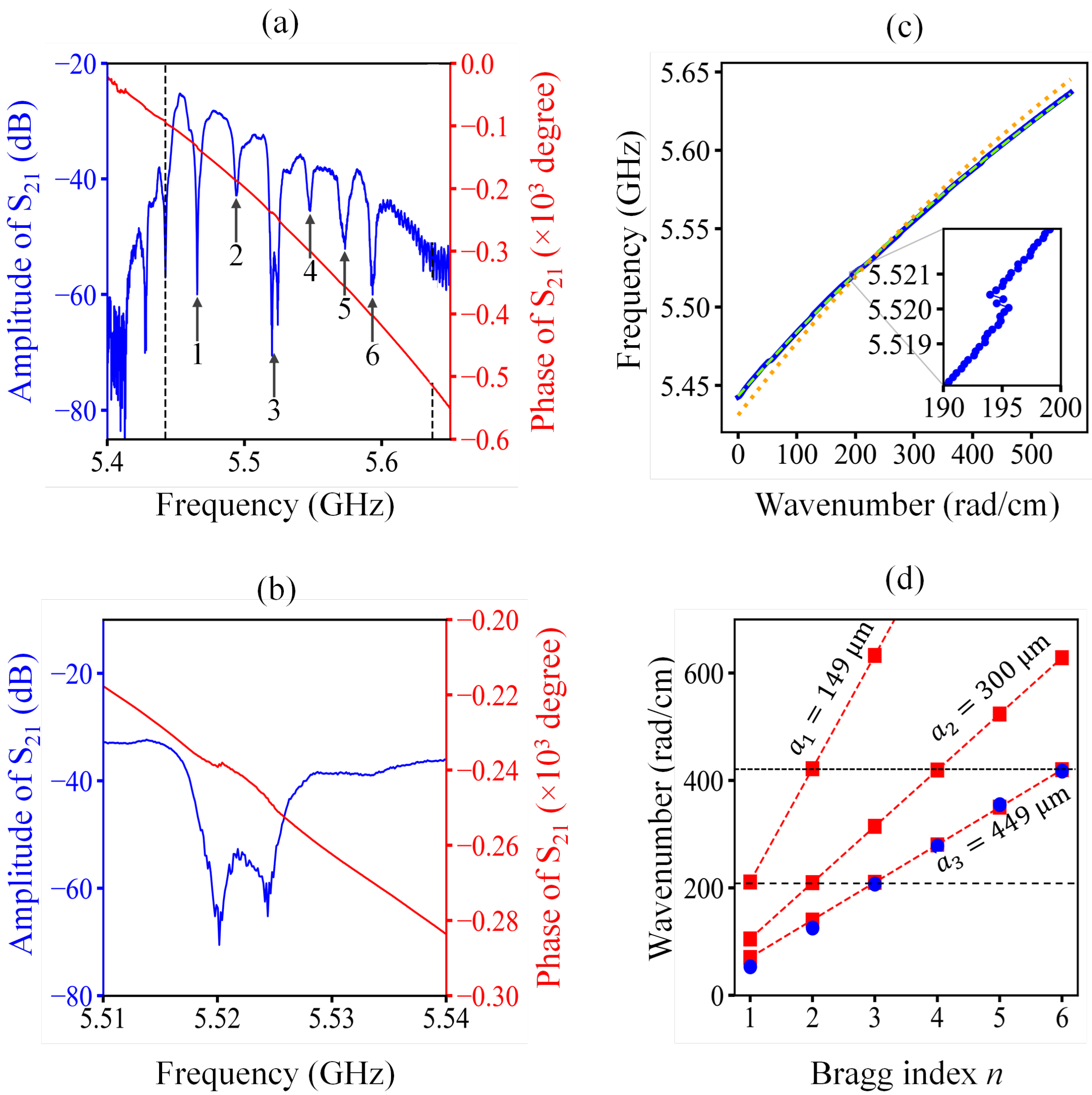

Figure 5.4: Spin waves in a doubly periodic magnonic crystal, with $a1 = 149\,\mu\mathrm{m}$ and $a2 = 300\,\mu\mathrm{m}$. (a) Transmission coefficient S_{21} of the magnonic crystal measured under a field of $H_0 = 1240\,\mathrm{Oe}$ applied in the sample plane and perpendicular to the sample length direction. The blue and red profiles show the amplitude and phase of S_{21}, respectively, as a function of frequency. The dashed black line marks the FMR frequency. The vertical arrows point to the centers of the band gaps. (b) Zoomed-in view of (a) near the third band gap. (c) Dispersion curve. The solid curve shows the measured dispersion response while the dotted and dashed curves are numerical fits. (d) Measured Bragg wavenumbers (blue points) compared to calculated Bragg wavenumbers (red squares).

where $a = 400\,\mu\text{m}$ is the groove period or lattice constant of the magnonic crystal and $n = 1, 2, \ldots$ is the Bragg index. k_n in (5.3) is referred to as Bragg wavenumber in the following discussion.

Based on the measured dispersion curve and the transmission dips, five Bragg wavenumbers are identified, which are shown by the blue points in Fig. 5.3(d). According to (5.3), one can readily calculate the Bragg wavenumbers for $n = 1, 2, \ldots, 6$. These calculated wavenumbers are presented as the red points in Fig. 5.3(d). One can see a good agreement between the measured and calculated Bragg wavenumbers. This agreement justifies that the experimentally observed transmission dips are indeed the indications of the band gaps. Further justifications are presented in Section 5.5. However, the comparison in Fig. 5.3(d) clearly indicates the absence of k_5 in the experimental data. This is discussed briefly in Section 5.5. Note that a fitting of the experimental data point in Fig. 5.3(d) against (5.3) yields $a = ((378 \pm 17)\,\mu\text{m})$, which is slightly smaller than the period $((400 \pm 4)\,\mu\text{m})$ determined through the surface profile measurements.

Further, the data in Figs. 5.3(a) and 5.3(b) also show that the transmission dips appear similar in the sense that they have similar shapes and linewidths. They do exhibit different depths, as explained in the following. In an idealized single-periodic magnonic crystal, one might expect all Bragg modes to exhibit similar or uniform reflection characteristics, giving rise to similar transmission dips. However, in real systems, the reflection behavior of each mode is influenced by its unique spin-wave profile and boundary condition configuration. These factors lead to variations in the depth of transmission dips. As shown in Fig. 5.3(a), the third dip exhibits the greatest depth. This pronounced feature can be attributed to the $n = 3$ mode experiencing the strongest constructive interference; the alignment of its nodes and antinodes with the grooves effectively enhances reflection at the corresponding frequency of the third dip. Additionally, wavenumber-dependent properties, such as group velocity and two-magnon scattering, further disrupt the theoretical uniformity of reflection features, causing certain modes to stand out more prominently than others.

Turn now to the data presented in Fig. 5.4 for the doubly periodic magnonic crystal. To ease the comparison, the data in Fig. 5.4 are presented in the same format as those in Fig. 5.3. When compared to the S_{21} data in Fig. 5.3, the data in Fig. 5.4 show two major differences: (1) the third dip from the left is much broader and (2) the sixth dip is significantly more pronounced. Further, when compared with other dips in the same transmission profile, one can see that (1) the third dip is the strongest and (2) the sixth dip is stronger than both the fourth and fifth dips. These observations together suggest that every third dip represents a special condition when compared with the other dips.

Figure 5.4(d) presents the experimental Bragg wavenumbers in blue points and three sets of calculated Bragg wavenumbers in red squares. From top to bottom, those three sets of Bragg wavenumbers were calculated for lattice constants $a_1 = 149\,\mu\text{m}$, $a_2 = 300\,\mu\text{m}$, and $a_3 = a_1 + a_2 = 449\,\mu\text{m}$, respectively, as indicated. The comparison of the measured and calculated Bragg wavenumbers gives two important results. First, there is a good agreement between the experimental values and the values calculated with a lattice constant of $a_3 = a_1 + a_2 = 449\,\mu\text{m}$. This means that the six dips in the transmission profile correspond to six band gaps that are formed due to the Bragg reflection at $k_n(a_1 + a_2) = n\pi$ where $n = 1, 2, \ldots, 6$. Second, for the third dip, the Bragg wavenumber simultaneously satisfies three Bragg conditions, as indicated by the horizontal dashed line. Those three conditions are $k_3a_3 = 3\pi$ for the lattice constant $a_3 = 449\,\mu\text{m}$, $k_2a_2 = 2\pi$ for the lattice constant $a_2 = 300\,\mu\text{m}$, and $k_1a_1 = \pi$ for the lattice constant $a_1 = 149\,\mu\text{m}$. For the sixth dip, the Bragg wavenumber also simultaneously satisfies three Bragg conditions, as indicated by the horizontal dotted line. This result indicates that the formation of every third band gap involves triple Bragg reflections. This clearly explains why the third and sixth dips are more pronounced.

Three notes should be made about the experimental data presented above. First, the spin waves shown by the data in Figs. 5.2, 5.3, and 5.4 have different frequencies which are due to the use of different magnetic field strengths (H_0) during the measurements. Adjusting the field strength would shift the S_{21} responses along the frequency axis, but this would not affect the qualitative results described above.

Second, for $f < f_B$, the S_{21} amplitude vs. frequency profiles reveal some non-trivial responses above the noise level. These responses are particularly noticeable in Fig. 5.2(b) and Fig. 5.4(a). The presence of such responses is associated with the fact that the YIG waveguide in this study is not exactly one-dimensional and spin waves along the field direction are therefore not completely absent. Spin waves propagating along an in-plane field are classified as backward volume waves whose frequencies are below f_B. [69], [72] Further, in the $f < f_B$ regime shown in Fig. 5.4(a), the S_{21} amplitude also shows a dip at about 5.43 GHz. This dip may be associated with one of the width modes across the YIG sample width, and one may confirm this association by examining how the dip varies as the field is rotated in-plane.

Third, the orange dotted curves in Fig. 5.3(c) and Fig. 5.4(c) show a noticeable mismatch with the experimental dispersion curves. This discrepancy arises because the fitting process treated the film thickness t as a constant and varied only the saturation induction $4\pi M_s$ as the fitting parameter. The t values used were derived from the SEM measurements, as mentioned earlier, and the fitting-yielded $4\pi M_s$ values are given in Table 5.1. However, allowing both t and $4\pi M_s$ to vary as free parameters results in nearly perfect fits to the experimental dispersion curves. This improved fit is demonstrated by the green dashed curve presented in Fig. 5.4(c). The fitting yielded $t = 3.6\,\mu\text{m}$, which is smaller than the value ($4.2\,\mu\text{m}$) from the SEM measurement, and $4\pi M_s = 1801\,\text{G}$, which is slightly larger than the value (1790 G) obtained with $4\pi M_s$ as the sole fitting parameter. The notable difference in film thickness likely stems from errors in the SEM-based measurement, though this does not significantly impact the analysis in this work since the focus is on surface spin waves rather than volume spin waves.

5.5 Numerical Simulations

To further support the above explanation of the experimental observations, numerical simulations were carried out in Python using the transfer matrix method (TMM), a well-established technique for analyzing spin-wave propagation. [64], [68], [74], [75], [76] In this approach, a transfer matrix A transforms the state of the spin wave across a potential interface by enforcing the continuity of the wavefunction and its derivative:

$$\begin{pmatrix} \psi_1 & \psi_2' \end{pmatrix} = A_2^1 \begin{pmatrix} \psi_1 & \psi_2' \end{pmatrix}, \tag{5.4}$$

where ψ_1 and ψ_2 represent the wavefunction within the regions on either side of the interface and the primed variable ψ' denotes the spatial derivative. The transfer matrix A_2^1 is explicitly constructed from the wavenumbers k_1 and k_2 within the respective regions by taking the assertion of continuity in (5.4) and rearranging for the outgoing signal in terms of the incoming signal. [77] The result is

$$A_2^1 = \begin{bmatrix} \frac{1}{2}\left(1+\frac{k_1}{k_2}\right) & \frac{1}{2}\left(1-\frac{k_1}{k_2}\right) \\ \frac{1}{2}\left(1-\frac{k_1}{k_2}\right) & \frac{1}{2}\left(1+\frac{k_1}{k_2}\right) \end{bmatrix}. \tag{5.5}$$

To simulate the experimental configuration composed of multiple interfaces, the full potential profile of the magnonic crystal samples is discretized into regions each associated with its own transfer matrix. The wavenumber within each region is a function of the sample thickness at that position x:

$$k(x) = k_0 \frac{t}{t - D(x)}, \tag{5.6}$$

where t is the uniform film thickness and $D(x)$ is the groove depth. The flat regions corresponding to the uniform sections and the bottoms of grooves are represented by individual transfer matrices, while the sloping regions in between are divided into N potential steps. Convergence is ensured by choosing N sufficiently large such that the difference between results for N and $N/2$ is less than 10^{-10}.

The simulations use the measured sample properties presented in Table 5.1 and the applied field strengths (H_0) as used in Section 5.4. For each initial wave number, the transfer matrix for each region is computed and the transmittance and reflectance are derived. This process is repeated for all wavenumbers corresponding to the frequencies measured in the experiment. The transfer matrix (5.5) does not account for any lossy interactions, so the simulation takes spin-wave decay into account with a factor e^{-ak+b} to represent the physical decay term $e^{(}-\eta l/v_g)$ discussed in Section 5.3 and scale the simulation amplitude to the experiment. This factor provides a better visual comparison to the experimental results without affecting the location of the Bragg reflections, but it was not rigorously determined.

Figure 5.5 compares the simulated transmission profiles (blue) with the experimental profiles (red). The profiles in (a) and (b) are for the singly and doubly periodic magnonic crystals, respectively. The comparison gives three important results. First, the transmission dips in the simulated profiles align with those in the experimental profiles. Second, for the profiles in Fig. 5.5(a), the relative strengths (depths) of the simulated dips agree with those of the experimental dips. These two results together clearly show the accuracy of the numerical simulations. Finally, the numerical profiles in Fig. 5.5(b) evidently confirm the experimental observation that for the doubly periodic magnonic crystal, the third and sixth dips are more pronounced than other dips.

To confirm the interpretation of the strong third and sixth dips given in the last section, Figure 5.6 compares two numerical transmission profiles. The blue profile, which is the same as in Fig.

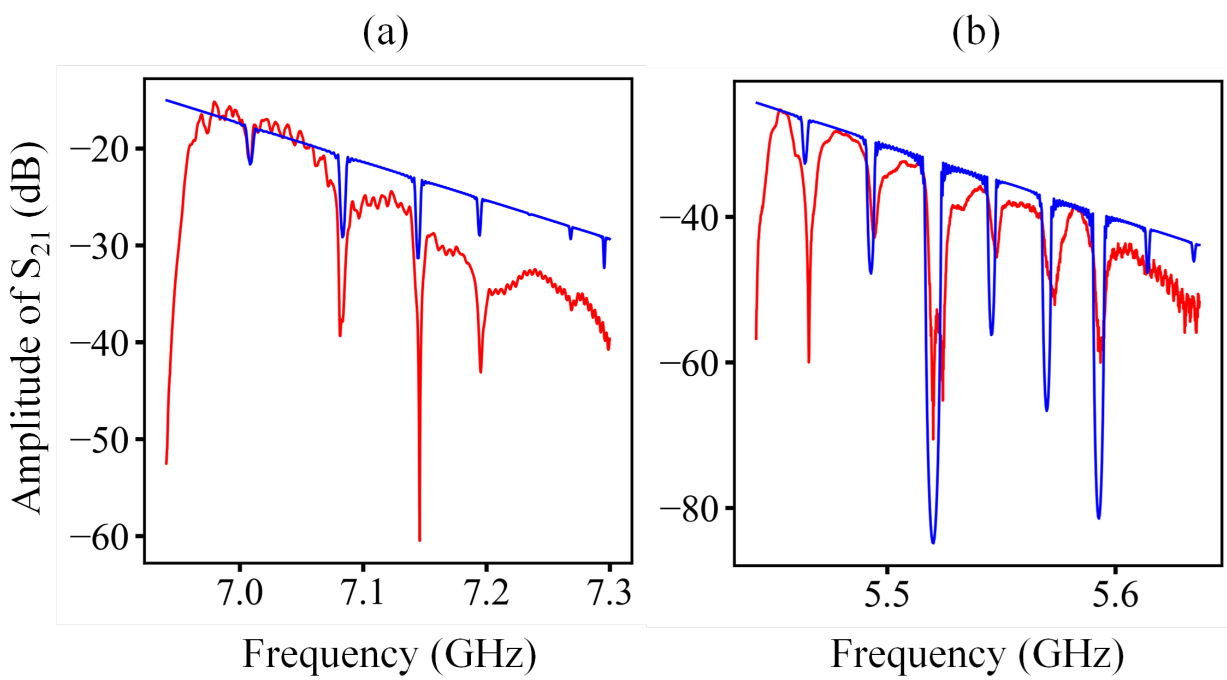

Figure 5.5: Comparison of experimental (red) and simulated (blue) transmission profiles in (a) the singly periodic magnonic crystal and (b) the doubly periodic magnonic crystal.

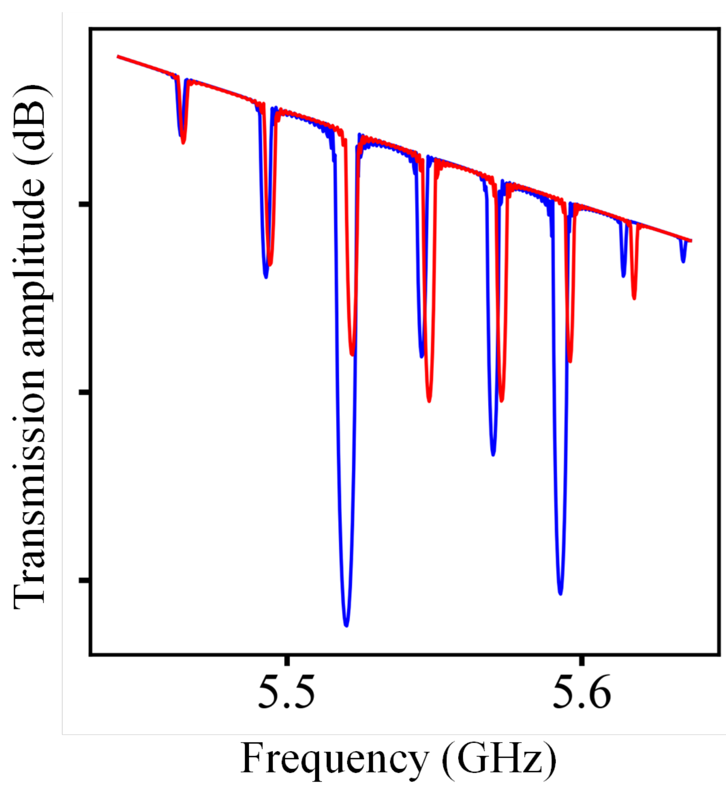

Figure 5.6: Simulated transmission profiles of the doubly periodic magnonic crystal with $a_1 = 149\,\mu\text{m}$ and $a_2 = 300\,\mu\text{m}$ (blue) and a magnonic crystal with a single periodicity $a_3 = a_1 + a_2$ (red).

5.5(b), is the simulation of the doubly periodic magnonic crystal using the dimensions as measured and shown previously, while the red profile is the simulation of a magnonic crystal with a single period equal to $a_1+a_2 = 449\,\mu\mathrm{m}$. The simulations used the same magnetic field as in the experiment, which is $H_0 = 1240\,\mathrm{Oe}$. These simulations explicitly show the effect on the transmission dips due to the second period and thereby confirm that the pronounced dips result from multiple Bragg reflections associated with the double periodicity.

Additionally, the numerical profile in Fig. 5.5(a) reveals a very tiny dip at about 7.235 GHz, which is the fifth dip from the left. This explains why the fifth dip is not visible in the transmission profile in Fig. 5.3(a) and the k_5 point is missing in Fig. 5.3(d). As discussed earlier, the reflection behavior of each mode is influenced by its unique spin-wave profile and boundary condition configuration. For the $n = 5$ mode, the specific configuration results in a minimal transmission dip. This finding has been verified by additional simulations. For instance, increasing the groove width by about 50 % significantly enhances the depth of the fifth dip, making it even deeper than the fourth dip, while maintaining the same dip locations.

5.6 Conclusion

In conclusion, this work explored the effects of double periodicity on the band gaps of spin waves in a 1D magnonic crystal. Transverse line grooves were chemically etched into a long and narrow YIG thin film strip to create a magnonic crystal with alternating lattice constants $a_1 = 149\,\mu\mathrm{m}$ and $a_2 = 300\,\mu\mathrm{m}$. The propagation of spin waves in this doubly periodic magnonic crystal was measured experimentally using a VNA and simulated numerically using a transfer matrix method. The experimental and numerical results show that the third and sixth band gaps are more pronounced than the other band gaps; the underlying physics is that the wavenumbers associated with those band gaps satisfy simultaneously triple Bragg conditions for periods $a_1 = 149\,\mu\mathrm{m}$, $a_2 = 300\,\mu\mathrm{m}$, and $a_3 = a_1 + a_2 = 449\,\mu\mathrm{m}$. These results indicate that the introduction of a secondary periodicity into a magnonic crystal represents an effective strategy for tailoring band gap properties in magnonic crystals. Future work that explores in-gap magnonic states or nonlinear spin-wave dynamics in similar doubly periodic magnonic crystals is of great interest. It is also of great interest to examine spin-wave dynamics in doubly periodic magnonic crystals where the two periods a_1 and a_2 are incommensurable.

It is worth noting that finite-size effects and mode hybridizations might also play a role in enhancing the third and sixth band gaps. However, these contributions are believed to be minimal for the following reasons. First, multiple reflections of spin waves from the two ends of the YIG waveguides could produce a Fabry-Pérot-like effect, which might enhance the observed band gaps. Nonetheless, this effect is expected to be weak, as the YIG sample lengths (e.g., 22.6 mm for the doubly periodic sample) in this study are substantially larger than the transducer separations (e.g., 7.4 mm for the doubly periodic sample). As a result, the spin waves reflected from the sample ends undergo significant attenuation, especially when considering the non-reciprocal nature of the MSSWs. Additionally, the numerical simulations in this study were deliberately designed to exclude explicit boundary reflections, effectively mimicking an infinite magnonic crystal without a Fabry-Pérot cavity. These boundary-free simulations reproduced the enhanced third and sixth dips at precisely the same frequencies observed experimentally. This strong correspondence suggests that the observed band-gap enhancements are an intrinsic consequence of the double periodicity rather than artifacts of finite sample length.

The geometry and magnetic field configuration used in this study predominantly excited the fundamental surface wave mode, while higher-order modes (i.e., thickness modes) were minimally populated during measurements. As a result, there was no significant mode hybridization with higher-order modes. Additionally, each etched groove in the magnonic crystal could potentially host localized states or defect modes. If such modes are coupled strongly with traveling spin waves, they might produce additional gaps or sidebands. However, the primary transmission dips observed coincide with the triple Bragg condition predicted by the TMM model, indicating that these features are not due to localized modes.

Finally, a note on the phase analysis is warranted. In this work, the extraction of spin-wave dispersion from the experimentally measured phase data assumed that the spin waves in the magnonic crystals behave as plane waves, even though the periodic structure inherently supports Bloch-type spin waves. Two factors justify this approximation. First, the measured S_{21} phase primarily reflects the phase accumulation between the excitation and detection transducers. While the grooves introduce periodic perturbations, the net phase shift measured by the VNA effectively represents an average of the local wavevector along the entire propagation path. Consequently, the total phase accumulation can be approximated by an effective wavevector. Second, while the TMM model accurately describes Bloch-like wave propagation through a discretized stack of grooves, the calculated band-gap frequencies align closely with those inferred from the simpler plane-wave phase data. This alignment suggests that small deviations from the plane-wave approximation do not significantly affect the principal spin-wave dispersion in the magnonic crystals studied here.

Lastly, it should be noted that the YIG films in the three samples used in this study have varying thicknesses. However, these differences do not substantially impact the main conclusions, as all measurements were performed in a surface wave configuration. Thus, the dynamics examined are primarily confined to the top surfaces of the films, rather than spanning their entire thickness.

Chapter 6. Passive Microwave Remote Sensing

6.1 Introduction

Remote sensing scientists are motivated to use microwave frequencies because, at these frequencies, there is minimal scattering due to the atmosphere and thin clouds, and because measurements are independent of the time of day. Active microwave remote sensing, i.e., radar, uses a separate transmitter and receiver to send a signal and measure its reflection. Passive microwave remote sensing, called radiometry, eschews the transmitter and measures the small amount of electromagnetic energy that is emitted and scattered by all objects. A microwave radiometer is a highly sensitive receiver for measuring these low levels of microwave radiation.

Microwave radiometers were initially developed and applied in the 1930s and 1940s to measure the cosmos. In 1963, the Mariner 2 satellite flew past Venus to measure its atmosphere and temperature [78]. In 1978, the Nimbus 7 satellite carried the Scanning Multichannel Microwave Radiometer (SMMR) to an altitude of nearly 950 km. SMMR was the first multi-frequency, dual-polarization radiometer to passively measure the Earth from orbit, and the data it collected throughout its lifetime (operations ended in 1987) were widely applied [79]. SMMR was succeeded by a number of instruments that today include the Advanced Microwave Sounding Unit (AMSU) and the Special Sensor Microwave Imager / Sounder (SSMIS).

6.1.1 Aside: On Spectrum

Because microwave radiation is weakly attenuated in the atmosphere, microwave technologies have become the backbone of over-the-air communications and connectivity that define the modern era. Although it spans multiple orders of magnitude in frequency, the microwave spectrum is a shared and finite resource with an enormous and increasing number of users. Greater available bandwidth is universally beneficial for increased data throughput (for data transfer and supporting a large number of devices), or if only to help isolate one's application from nearby signals (desirable for both scientific research and communications).

In the United States, the Radio Act of 1912 was the first policy addressing the idea of spectrum management. Today, management is overseen by the Federal Communications Commission (FCC) for commercial and university users, and by the National Telecommunications and Information Association (NTIA) for federal users. Other nations have their own similar regulatory bodies. The International Telecommunications Union (ITU) is a United Nations (UN) agency[12] focused on worldwide spectrum concerns, which are reviewed at World Radiocommunication Conferences on a roughly four-year cadence.

In the United States, portions of the spectrum are allocated or reserved, and others are leased in Congressional auctions. The graphic in Figure 6.1 is a portion of the United States frequency allocation chart published by the NTIA in 2025 [80], illustrating the density of services.

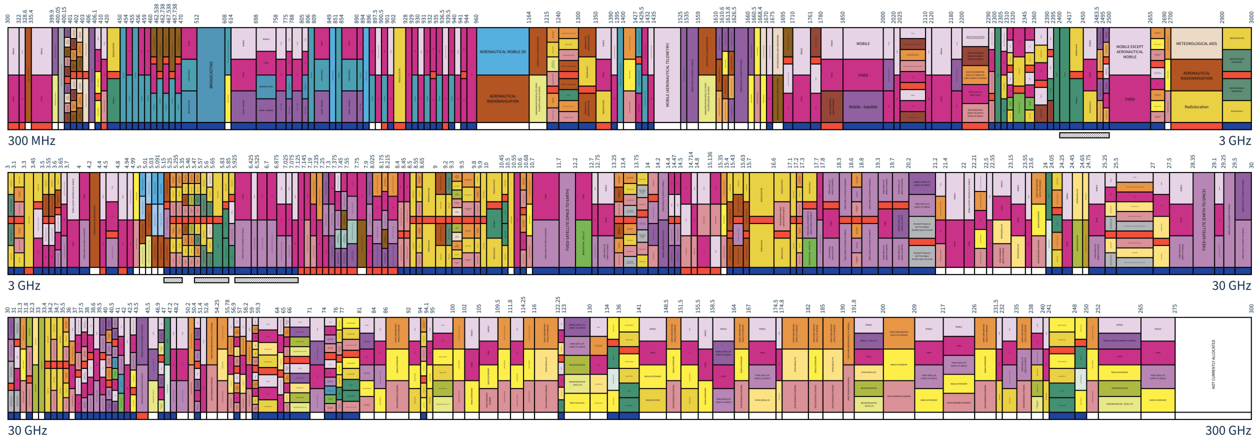

Figure 6.1: Frequency allocations in the United States as of September 2025, cropped from the full image to illustrate the density of services solely within the frequency range of 300 MHz–300 GHz. The full image is provided by the NTIA and is available online [80].

This aside intends to bring attention and consideration to the idea of spectrum as a resource and form of infrastructure, and of spectrum management as an urgent and global concern. Conflicts in spectrum access can and do exist among industry, government, and research users. Additional context may be found by exploring "dynamic and reconfigurable" technologies, which facilitate the broader idea of spectrum sharing.

[12] The ITU (1865) predates the UN (1945) by eighty years.

6.2 Blackbody Emission

Any object above 0 K emits energy into its environment in the form of electromagnetic radiation. At thermal equilibrium, conservation of energy requires that the energy emitted by the object is equal to the energy absorbed. A blackbody is a theoretical object that perfectly absorbs all incident radiation, and correspondingly has idealized emissive properties. Classical models attempting to characterize a blackbody were unsuccessful. In 1901, Max Planck published a model considering the radiated energy as discretely-valued and proportional to the frequency times a constant, $E = hf$, which was the first quantum theory in physics. Planck's solution is

$$L_f(f;T) = \frac{2hf^3}{c^2}\left[\exp\left(\frac{hf}{kT}\right) - 1\right]^{-1}, \tag{6.1}$$

where $L_f(f;T)$ $[\mathrm{W\,sr^{-1}\,m^{-2}\,Hz^{-1}}]$ is the spectral radiance at a frequency, f, and absolute temperature (in Kelvin), T, c is the speed of light in vacuum, $h = 6.626 \times 10^{-34}\,\mathrm{J\,Hz^{-1}}$ is the Planck constant, and $k = 1.381 \times 10^{-23}\,\mathrm{J\,K^{-1}}$ is the Boltzmann constant.[13] (6.1) is plotted in Figure 6.2 for three temperatures that have maximum radiance near the visible spectrum. The total radiance increases with increasing temperature, and the maximum value is blue-shifted to higher frequencies.

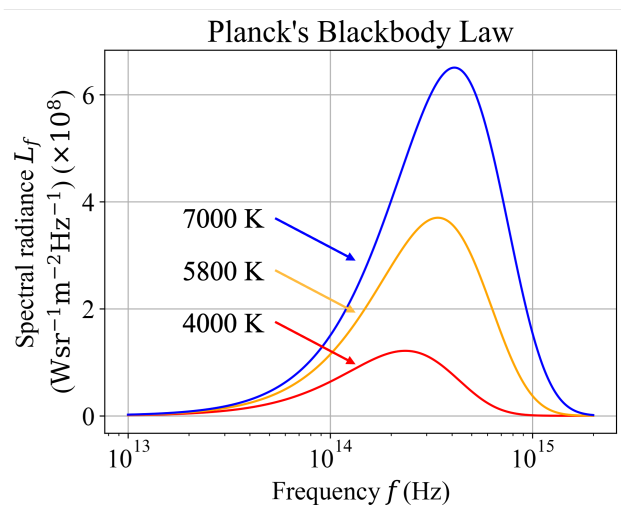

Figure 6.2: Spectral radiance at three absolute temperatures described by Planck's law. The total emitted power is increased with increasing temperature, and the frequency of maximum radiance is shifted to higher frequency.

[13] c, h, and k are three of the seven fundamental SI constants referrred to in Chapter 1.

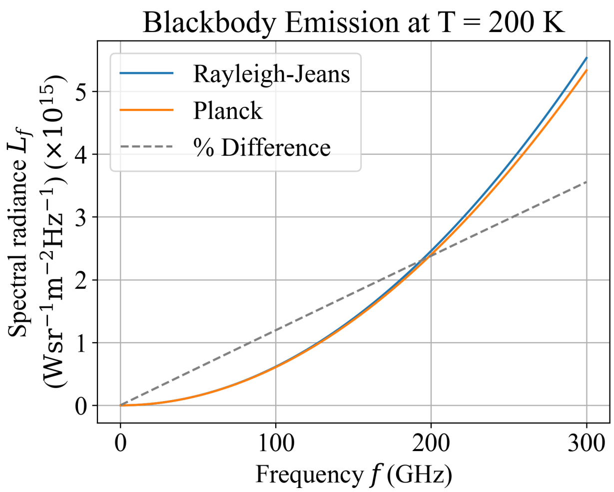

Figure 6.3: Spectral radiance up to 300 GHz for a blackbody with physical temperature $T = 200\,\mathrm{K}$, calculated with Planck's Law (6.1) (orange) and the Rayleigh-Jeans approximation (6.3) (blue). The approximation deviates from Planck's law at high frequencies and/or low temperatures, predicting greater values. The percent difference is plotted as a dashed line using the same y-axis values.

A useful approximation at microwave frequencies is made by considering $hf/kT \ll 1$ and expanding the second term as a Taylor series. Then,

$$\exp\left(\frac{hf}{kT}\right) - 1 \approx \frac{hf}{kT} \tag{6.2}$$

and (6.1) becomes

$$L_f(f;T) = \frac{2kTf^2}{c^2}. \tag{6.3}$$

This is the Rayleigh-Jeans approximation, which was separately derived using a classical approach before Planck's publication. The Rayleigh-Jeans approximation is very accurate for microwave frequencies and typical Earth temperatures, as shown in Figure 6.3, and is typically used for microwave calculations.

The power, P_{bb}, emitted by a blackbody and measured by an antenna is determined as

$$P_{bb} = \int_B A\Omega L_f df, \tag{6.4}$$

where A is receiving area, Ω is the solid angle subtended by the blackbody, and B is the measurement bandwidth. A linearly polarized antenna measures one of two orthogonal polarizations, so the received power is at most half of what is emitted. The directivity of the antenna is considered for Ω via its pattern $F(\theta, \phi)$ integrated over a sphere. So,

$$P_{bb} = \frac{1}{2} A \int_B \iint_{4\pi} L_f F(\theta, \phi) d\Omega df. \tag{6.5}$$

L_f can be considered to be constant for a narrow bandwidth, i.e., $B \ll f$, so the integral over frequency is simply B. Substituting L_f using (6.3):

$$P_{bb} = \frac{1}{2} AB(2kTf^2c^{-2}) \iint_{4\pi} F(\theta, \phi) d\Omega. \tag{6.6}$$

The remaining integral defines the antenna pattern solid angle, $\Omega_p = c^2 f^{-2}/A$. With this substitution, (6.4) is reduced to

$$P_{bb} = kTB \tag{6.7}$$

This result shows the direct, linear relationship between physical temperature and power, which is a fundamental relationship in passive microwave remote sensing.

Real objects, however, are not blackbodies, so the measured power will always be less than that of P_{bb}. Real objects are sometimes referred to as graybodies, and a graybody's emissivity, e, is defined as the ratio of real measured power, P, compared to that of a blackbody at the same physical temperature:

$$e = \frac{P}{P_{bb}} = \frac{T_B}{T} \leq 1. \tag{6.8}$$

$T_B = eT$ is the blackbody-equivalent radiometric temperature called the brightness temperature. Brightness temperature is the unit of measurement for radiometric systems: it is directly proportional to power, as shown, and is generally simpler to use and discuss because of the direct relation to physical, or thermodynamic, temperature.

6.3 Microwave Radiometry for Measurements of the Atmosphere

The Earth's atmosphere is characterized in part by its temperature, T, pressure, P, and humidity, ρ. Within microwave radiometry, the so-called forward problem takes these properties as inputs to predict the brightness temperature observed by a radiometer, and the inverse problem starts with radiometric data to determine T, P, and ρ. Standard models of the atmosphere such as the International or U.S. standard atmospheres provide reference values of T and P as functions of altitude. *In situ* measurements of T, P, and ρ are performed by small, disposable devices called radiosondes. Hundreds of radiosondes are launched from the ground daily across the globe and can reach altitudes above 30 km, and the data are shared by international agreement [81]. Figure 6.4 is a map provided by the National Oceanographic and Atmospheric Administrations (NOAA) showing the radiosonde launch sites across the world.

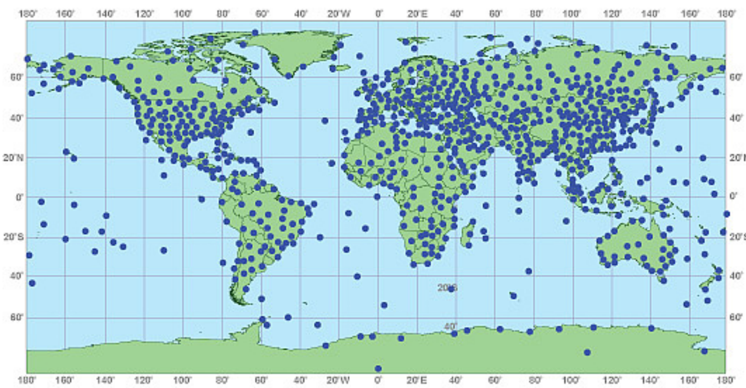

Figure 6.4: Map of radiosonde launch sites around the world, provided by NOAA [81].

The temperature of the atmosphere follows a predictable pattern with altitude, which is used to designate vertically-stratified regions called layers. Nearly all weather phenomena and mass of the atmosphere are contained within and shortly beyond the layer closest to the surface, called the troposphere. The troposphere is defined by a linear decrease in temperature with altitude according to a lapse rate of approximately $-dT/dz = 6.5\,\mathrm{K/km}$. The top of the troposphere is called the tropopause and is defined by dT/dz abruptly becoming zero. The tropopause is at an altitude somewhere between 10 km and 20 km; it is higher at the equator and lower at the poles. T increases within the next layer, called the stratosphere, which extends to $\sim$50 km.

The pressure of the atmosphere can be modeled in general by a decaying exponential, with weather and location having relatively small impacts. Standard models assume the case of an ideal gas to define the pressure as

$$P(z) = P_0 e^{-z/7.7}, \tag{6.9}$$

where z is the altitude in km and $P_0 = 1013.25\,\mathrm{mbar}$ is the standard atmospheric pressure at sea level. Water vapor content (humidity) is much more variable, depending on weather, location, time of day, and temperature.

The atmospheric constituents with significant absorption (and, therefore, emission) at microwave frequencies are oxygen (O_2) and water vapor (H_2O). Planck showed that the transition between energy levels is quantized, such that

$$\Delta E = hf, \tag{6.10}$$

where ΔE is the energy difference between the initial and final states. A single atom has only electronic transitions between energy levels E_e on the order of 2 eV to 10 eV. A molecular structure introduces vibrational states with $E_v \approx 0.2\,\mathrm{eV}$ to 2 eV and rotational states with $E_r < 5 \times 10^{-2}\,\mathrm{eV}$. The energy of any particular state is thus $E = E_e + E_v + E_r$. Transitions in the microwave region are purely between rotational states.

Molecular oxygen has a permanent magnetic dipole moment. An absorption spectrum exhibits a single line at 118.75 GHz, and a group of thirty-seven lines between 50 GHz to 69 GHz. This group is referred to as the 60 GHz oxygen complex. The water vapor molecule is polar, so it has a permanent electric dipole moment. Electromagnetic interactions with the moment create absorption lines at 22.235 GHz and 183.31 GHz. Additional absorption lines above 300 GHz contribute to the overall microwave absorption profile. O_2 and H_2O are measured to determine the temperature and humidity of the atmosphere, respectively.

The absorption (emission) spectrum of a static and isolated molecule would consist of zero-width absorption lines at the transition frequencies, as shown in red in Figure 6.5. In the atmosphere, particles move, collide, and interact, and the net effect is that the transition linewidths are increased to nonzero values, as shown in blue in Figure 6.5. This phenomenon is called pressure broadening. Due to pressure broadening, the transition linewidths are a function of the temperature and pressure of the atmosphere. Altitudinal weighting functions are used to characterize the linewidths and determine T and ρ.

Frequency regions between absorptions are called window regions. For downward-looking radiometers, window regions provide a relatively unobstructed view of the Earth's surface. Spaceborne radiometers commonly use a frequency near 90 GHz as one window channel.

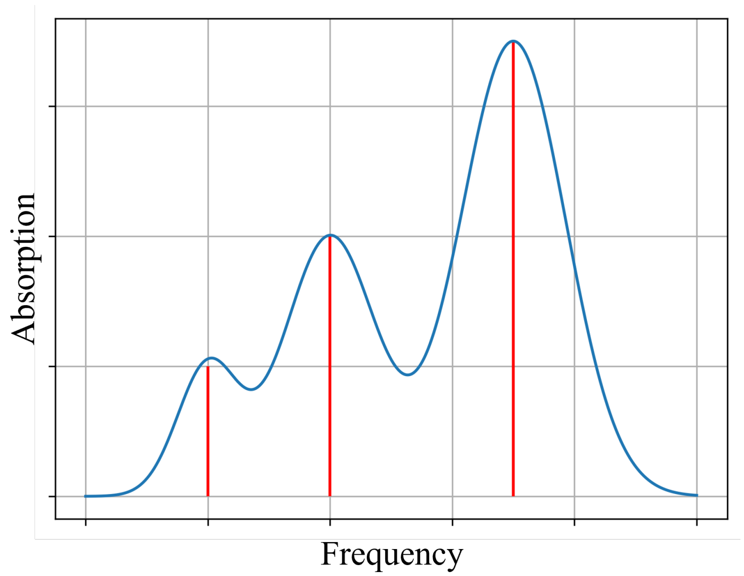

Figure 6.5: Example of an absorption spectrum. The theoretical absorption lines (red) are at precise frequencies. Due to pressure broadening, the absorption lines are spread out and overlap to create a continuum (blue).

6.4 Microwave Radiometers

A microwave radiometer is a highly-sensitive receiver used to measure passively-emitted graybody radiation. Radiometers in the context of atmospheric and climate studies are used to infer from measurements the temperature and humidity as functions of altitude, to determine wind speed and direction over oceans, record ice and snow coverage, etc.

The simplest design for a radiometer is that of a total-power radiometer, illustrated in Figure 6.6. As previously derived, the microwave receiver measures power equal to

$$P = GkT_A B, \tag{6.11}$$

where k is the Boltzmann constant, B and G are the bandwidth and gain, respectively, of the receiver, and T_A is the antenna temperature. However, the system temperature, T_{sys}, also includes a noise power contribution from the receiver itself, T_{rec}. The most impactful source of noise power is thermal and due to the motion of electrons. In 1928, Nyquist showed that the thermal noise power has a physical temperature dependence identical to that of the blackbody power, i.e., $P_N = kTB$ [82]. Using this result, a noisy microwave circuit can be modeled as a noise-free circuit with an equivalent noise source at the input. The noise temperature of the equivalent noise source for the radiometer is T_{rec}.

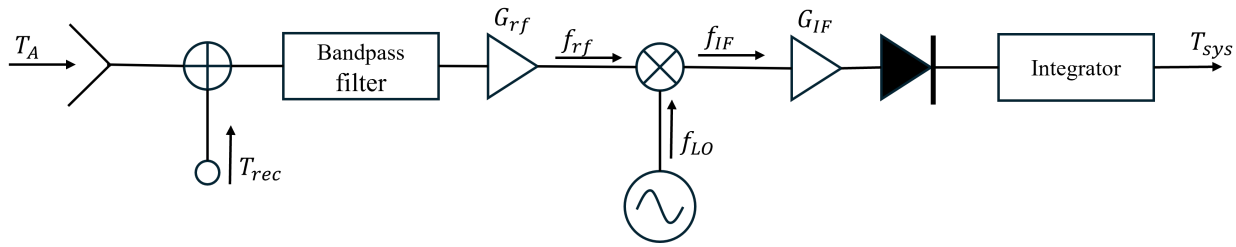

Figure 6.6: Illustrative design of a total-power radiometer.

Returning to Figure 6.6, a bandpass filter is used to restrict the signal to a bandwidth, B. A low-noise amplifier amplifies the signal by a factor G_{rf}. It is critical that this amplifier has a low noise figure because the first amplifier in a cascade has the greatest impact on the total noise figure. The radiometer in the figure shows a superheterodyne design, meaning that the signal is converted to an intermediate frequency (IF) for further amplification (and possibly filtering) before detection. The detector is a square-law detector, so the output voltage is proportional to input power. Finally, the signal is integrated for some time interval, τ.

A radiometer must be able to discern the low-level graybody signal from the inherent system noise, which may be significantly larger. The radiometric resolution (or sensitivity) of a radiometer due to receiver noise, ΔT_N, is a function of T_{sys}, B, and τ. The result is

$$\Delta T_N = \frac{T_{sys}}{\sqrt{B\tau}} = \frac{T_A + T_{rec}}{\sqrt{B\tau}}. \tag{6.12}$$

However, the detected voltage is also related to the total system gain, G, which may also fluctuate in time. A root-mean-squared value of ΔG would produce an uncertainty

$$\Delta T_G = T_{sys}\left(\frac{\Delta G}{\bar{G}}\right), \tag{6.13}$$

where $\bar{G}$ is the mean. Since T_N and T_G are independent, they add in quadrature:

$$\Delta T = \sqrt{\Delta T_N^2 + \Delta T_G^2} \tag{6.14}$$

$$= T_{sys}\sqrt{\frac{1}{B\tau} + \left(\frac{\Delta G}{\bar{G}}\right)^2}. \tag{6.15}$$

Uncertainty in the total-power radiometer is often dominated by gain variations. These can be reduced with frequent calibrations and by minimizing thermodynamic temperature variations at the amplifier and power supply.

A Dicke radiometer reduces the effect of gain fluctuations by modulating the input signal at a rate faster than that of gain fluctuations, typically between 1 ms to 20 ms. A switch (called the Dicke switch) at the antenna alternates the measurement between T_A and a reference load at known temperature T_{ref}, and a synchronized demodulator after the detector alternates the sign of T_A and T_{ref}. The result is that the output is proportional to $T_A - T_{ref}$, and the sensitivity is

$$\Delta T = \left[\frac{2(T_A + T_{rec})^2 + 2(T_{ref} + T_{rec})^2}{B\tau} + (T_A - T_{ref})^2\left(\frac{\Delta G}{\bar{G}}\right)^2\right]^{1/2}. \tag{6.16}$$

In practice, the Dicke radiometer has significantly reduced ΔT compared to a total-power radiometer. A so-called balanced Dicke radiometer is realized when $T_A = T_{ref}$, at which point the gain fluctation term is removed entirely and $\Delta T = \sqrt{2}\Delta T_N$. Feedback configurations can be used to maintain a balanced Dicke radiometer. The balanced condition highlights the tradeoff of the Dicke radiometer, which is that the sensitivity without gain variations is greater by a factor of $\sqrt{2}$. This can be addressed by reducing the integration time by a factor of 2, which is generally undesireable.

6.5 Radiometer Calibration

Calibrating the radiometer is required to determine antenna temperature from the detected quantity, which may be a voltage (considered in this discussion), a current, or digital counts. The square-law detector relates the measured voltage linearly to the antenna temperature as

$$V = aT_A + b, \tag{6.17}$$

where a and b are unknown constants. a may be referred to as the gain coefficient, and $b = V_0$ as the offset due to noise temperature. Calibrations are made using measurements of two targets with known temperature outputs, T_{hot} and T_{cold}. One calibration point may be sufficient if the noise temperature is well known [79], [83], [84], or to maintain a previous calibration [85]. A more stable linear fit is achieved when T_{hot} and T_{cold} are as widely separated as possible; a common practice is for T_{hot} to be the ambient temperature and for T_{cold} to be maintined by liquid nitrogen(LN2), which has a nominal boiling temperature of 77 K. Hot and cold calibration measurements yield

$$a = \frac{V_{hot} - V_{cold}}{T_{hot} - T_{cold}}. \tag{6.18}$$

Engineered calibration targets include noise-source diodes and microwave absorbers, which are typically measured at ambient temperature. Noise-source diodes are common in systems where they can be recalibrated, but long-term stability is a concern in spaceborne systems [86]. Microwave absorbers are materials that approximate the properties of a blackbody, so their measured brightness temperature is nearly equal to their physical temperature. Their effectiveness as a calibration target is determined by the accuracy of this approximation, generally quantified as absorptivity in decibels. For example, if the absorber is cooled using LN2 and the ambient temperature, $T_{amb} = 310\,\mathrm{K}$, then reflections of T_{amb} will cause the measured T_B to differ from T_{LN2} by

$$\Delta = (T_{amb} - T_{LN2})(1 - e) \tag{6.19}$$

$$= 233(1 - e). \tag{6.20}$$

An absorptivity of 20 dB corresponds to $e = 0.99$ and $\Delta = 2.33\,\mathrm{K}$, which is typically not satisfactory. A common target for absorbers is an absorptivity of 30 dB, which yields another factor of 10: $e = 0.999$ and $\Delta = 0.233\,\mathrm{K}$.

State-of-the-art absorbers used in spaceborne radiometer systems are made from ferrite-loaded epoxies that are arranged as arrays of pyramids coating a thermally-conductive base [87]. These have excellent absorptivity on the order of 35 dB [79], and are measured at ambient temperature to provide the T_{hot} calibration point. However, these devices are relatively bulky and thermal gradients exist from the base to tip of the pyramids. The thermal gradients are a source of uncertainty in the absorber temperature that is complicated to address [88], [89], [90], [91]. Chapter 7 discusses microwave absorbers based on metamaterials, which have a two-dimensional design that addresses both of these shortcomings.

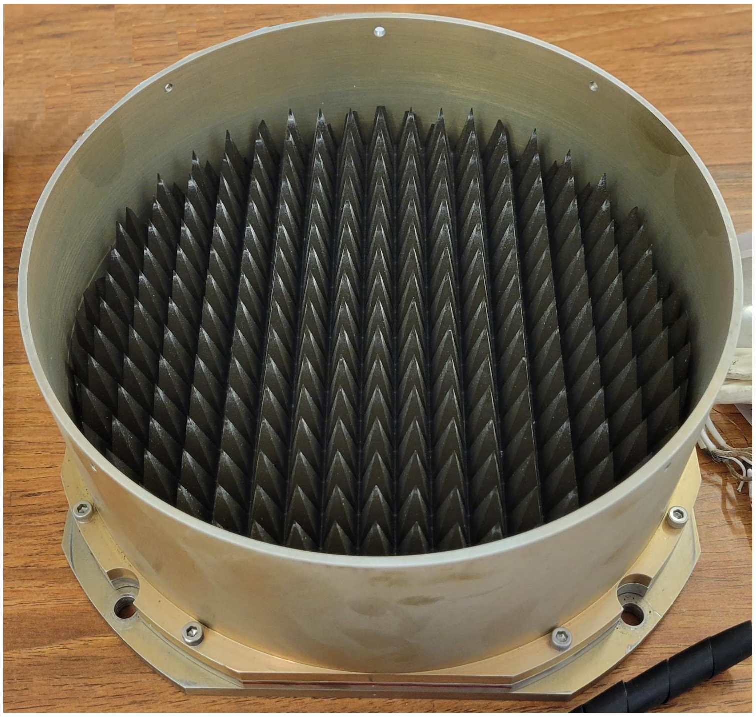

Figure 6.7: A ferrite-loaded epoxy absorber for use in a spaceborne microwave radiometer. The diameter is approximately 18 cm (= 7 in).

The cosmic microwave background (CMB) can also be used as a calibration target, particularly for spaceborne systems that are above the atmosphere. The CMB is remanent microwave radiation from the Big Bang. At microwave frequencies it can be considered as homogeneous and isotropic with a brightness temperature $T_{CMB} = 2.73\,\mathrm{K}$ [92], [93].

Ground-based radiometers can measure the CMB by means of a tipping-curve measurement. This is performed by measuring T_B as a function of the number of air masses, n_{atm}, where n_{atm} represents the number of atmospheres contributing to the observation. The radiometer pointed at zenith measures one atmosphere, $n_{atm} = 1$. The number of atmospheres as a function of the angle from zenith, θ, is $n_{atm} = \sec\theta$ for a horizontally-stratified model of the atmosphere. From the surface, the stratified model is valid at least to 70° [84] The intercept at $n_{atm} = 0$ represents a measurement with no contribution from the atmosphere.

Chapter 7. Novel Calibration Targets for Earth Remote Sensing

7.1 Introduction

Passive microwave Earth sensors in low Earth orbit (LEO), such as the Global Precipitation Measurement Microwave Imager (GPM-GMI), Advanced Microwave Sounding Unit (AMSU), Special Sensor Microwave Imager/Sounder (SSMIS), and the Advanced Technology Microwave Sounder (ATMS), provide remote observations of the atmosphere that are invaluable for numerical weather prediction. These instruments measure microwave emission near frequencies of absorption by atmospheric constituents; in particular, measurement of molecular oxygen (O_2) and water vapor (H_2O) provide information about the vertical distribution of temperature and humidity, respectively, based on the broadening of absorption lines due pressure as a function of altitude (a technique called "sounding"). The aforementioned instruments provide measurements at multiple frequencies—on the order of ten—to better characterize the vertical temperature and humidity profiles. Absorption lines for water vapor occur at 22.235 GHz and 183.31 GHz, and for oxygen there is a family of thirty-seven lines around 60 GHz (the "oxygen complex") and a single line at 118.75 GHz. Each instrument also measures so-called "window channels" of relative atmospheric transparency between absorption lines, which allow for information about surface characteristics, such as ocean wind vectors, from space, and for determining corrections to radar altimetry measurements [94].

The signals measured by passive Earth remote sensing instruments are due to Planck blackbody emission, which has a noise-like power spectrum, and include noise-power contributions from the hardware itself, which is typically double or more than that of the desired signal. The measurement resolution of a radiometer is proportional to the sum of these signals, meaning that, for example, a resolution of 1 K in a 300 K scene will require calibration accurate to one part in a thousand. As such, sensors require frequent and precise calibrations to avoid overwhelming measurement uncertainty, and these calibration sources must be stable over long periods of time (years to decades, in spaceborne instruments). A common approach used by spaceborne scanning radiometers is to perform a two-point calibration alongside each measurement of the scene. This is performed by measuring two sources that are widely separated in radiometric brightness temperature, T_B, to define a linear relationship between T_B and measured power [84]. T_B of a material is related to its physical temperature, T_p, by the material's emissivity, $e = T_B/T_p$. Effective targets for calibration need to emulate a blackbody: a hypothetical perfect absorber and emitter defined by $e = 1$. For a cold target, LEO radiometers often take advantage of the cosmic microwave background, or "cold space," as a very stable blackbody target with a homogeneous brightness temperature of 2.73 K [92]. The hot target is typically an on-board calibration target at the ambient temperature of the instrument, referred to as an "ambient load." State-of-the-art blackbody targets are arrays of metal pyramids covered in ferrite-loaded epoxy absorbing material. Applications typically demand "three nines" of performance, or $e \geq 0.999$, to meet the previous example of one part in a thousand accuracy. However, the geometry of these targets means that thermal gradients across the sample in three dimensions become a notable source of calibration uncertainty. A great deal of work has been performed to address this non-trivial problem [88], [89], [90], [91]. Additionally, the substantial mass and volume of these targets can complicate their integration for instruments with size, weight, and power constraints.

A potential alternative to pyramidal epoxy absorbers is a design based on metamaterial absorbers (MMAs). An electromagnetic metamaterial is an array of subwavelength elements with a precisely determined electric permittivity and magnetic permeability that result in desired macroscopic electromagnetic properties. Metamaterial designs are geometrically scalable, so they have found broad application across much of the electromagnetic spectrum [95], [96]. An MMA functions as a theoretically-perfect absorber—and, equivalently per Kirchhoff's law, a perfect emitter—at the designed frequency. MMAs can be constructed using well-established nanofabrication methods, including on printed circuit boards, and are effectively planar. An MMA calibration target could therefore dramatically reduce the temperature gradient uncertainty of current state-of-the-art absorbers. Absorption frequencies can be precisely tuned during the design process, and multiple frequencies can be incorporated to efficiently target distinct radiometer channels. As an added benefit, the reduced mass and height of MMAs compared to pyramidal absorbers make them appealing candidates for CubeSat or SmallSat instruments such as TROPICS, TEMPEST-D, and NEON SMBA, that take advantage of miniaturized modern hardware for lower-cost alternatives to traditional missions like those previously mentioned [89], [97], [98].

This chapter details the design and characterization of MMA calibration targets at four frequency bands, chosen for their relevance to atmospheric remote sensing. Section 7.2 describes the design and fabrication of MMA targets. Emissivity performance was measured in two ways: using a monostatic reflection experiment, Section 7.3, and using a radiometer at frequencies near the 183.31 GHz water vapor absorption line, Section 7.4.

7.2 Metamaterial Absorber Design and Fabrication

MMAs were designed and simulated using an electromagnetic simulation tool to demonstrate at least 30 dB of absorption, equivalent to an emissivity of 0.999, at the desired frequency. Four frequency bands, referred to as bands A, B, C, and D, were chosen for their relevance to Earth remote sensing and precedent use in existing radiometers (at least two frequency bands are present in each of the spaceborne microwave radiometers previously listed). Band A targets a center frequency of $f_A = 54.9$ GHz, which is within the oxygen complex and used to determine a vertical profile ("sounding") of atmospheric temperature. Band B targets $f_B = 90.3$ GHz, a window channel of relative transparency. In clear skies, this channel provides temperature and emissivity data from the Earth's surface [99], [100], and in cloudy skies, this channel is sensitive to precipitation mixtures of snow and ice [101] and can be used for wet-tropospheric radar altimetry calibration. Band C targets $f_C = 121.9$ GHz, which is above the oxygen resonance line at 118.75 GHz and is also used for temperature sounding. Band D targets $f_D = 179.1$ GHz, which is below the water vapor resonance line at 183.31 GHz and is used for humidity sounding.

The absorber elements for each metamaterial target follow a square resonator design with four "fins" approaching the center. This design is illustrated in Figure 7.1, with the conducting material colored yellow and the dielectric material colored green. The resonator unit cells are arranged in a grid pattern to constitute the MMA target. Single-band and multi-band MMA targets for bands A and B were created using standard methods for commercially fabricated printed circuit boards (PCBs), using copper as the conductive material and FR-4 as the dielectric material. The multi-band targets follow the same gridded layout, alternating the band A and band B absorber elements to create a 2×2 "supercell" and achieve absorption at two distinct frequencies. The designed and measured dimensions for the resonator elements at each band are collected in Table 7.1.

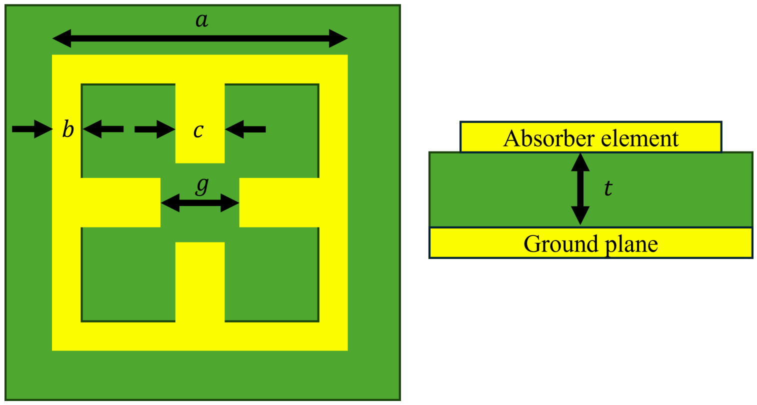

Figure 7.1: Illustrative diagram of an MMA resonator element viewed from the top (left), and side (right). The yellow regions are conductive, and the green regions are dielectric. The frequency of maximum absorption is tunable by adjusting the labeled dimensions.

PCB fabrication for designs targeting bands C and D was found to be challenging for two reasons. The first is the tolerances and minimum feature size of the metal traces in PCB fabrication. The shorter dimensions in the C and D designs (see Table 7.1) approach these tolerance limits, and the associated shifts in the metamaterial resonances as a consequence of dimensional mismatches of the metal trace lengths are more pronounced at the higher frequencies of the C and D bands. The second reason is the uncontrolled composition and lack of broadband characterization of FR-4 dielectric materials from commercial vendors. Significant discrepancy was observed between simulation and reflectivity experiments (Section 7.3) at frequencies between 100–200 GHz, even after performing sample metrology and updating the electromagnetic simulations. A constant dielectric permittivity and loss tangent for FR-4 was assumed based on published values from the vendor, which are only available up to 10 GHz. It is likely that these values differ at higher frequencies and require major effort to accurately characterize. FR-4 is a woven fiberglass cloth stabilized by an epoxy resin. Resin content and weave pattern can vary considerably between different FR-4 constructions, which impact the dielectric permittivity and loss. For these reasons, a nanofabrication approach using conventional photolithography was instead used to produce a calibration target covering bands C and D.

In place of FR-4, SU-8 2050 was found to be a suitable dielectric layer for the metamaterial design, due to both comparable loss values to FR-4 in the millimeter wave range as well as compatibility with standard photolithography processes. The SU-8 preparation recipe was optimized for spin coating thicknesses in the range of 70–80 um used in the C and D designs. The metamaterial elements were then patterned on the continuous SU-8 layer using a standard mask-based photolithography and metal lift-off process. To account for slight variability in the fabrication tolerances and SU-8 dielectric properties, several test arrays of scale factors up to ±4% of the base metamaterial designs were fabricated. One of the final metamaterial targets for the C and D designs is shown in Figure 7.2. While the nanofabrication approach produces targets with highly accurate and repeatable metamaterial features, it can produce minor flaws not typically seen in commercial PCB fabrication. These flaws include edge-beading of the SU-8 during spin coating, and regions of imperfect lift-off, highlighted in Figure 7.2. However, with further recipe optimization, these extrinsic effects can often be significantly reduced or eliminated. Results presented in the following sections demonstrate that both commercial PCB processing and nanofabrication can be used to fabricate MMA targets, with each approach offering respective advantages in terms of cost, throughput, and accuracy depending on the desired frequency range.

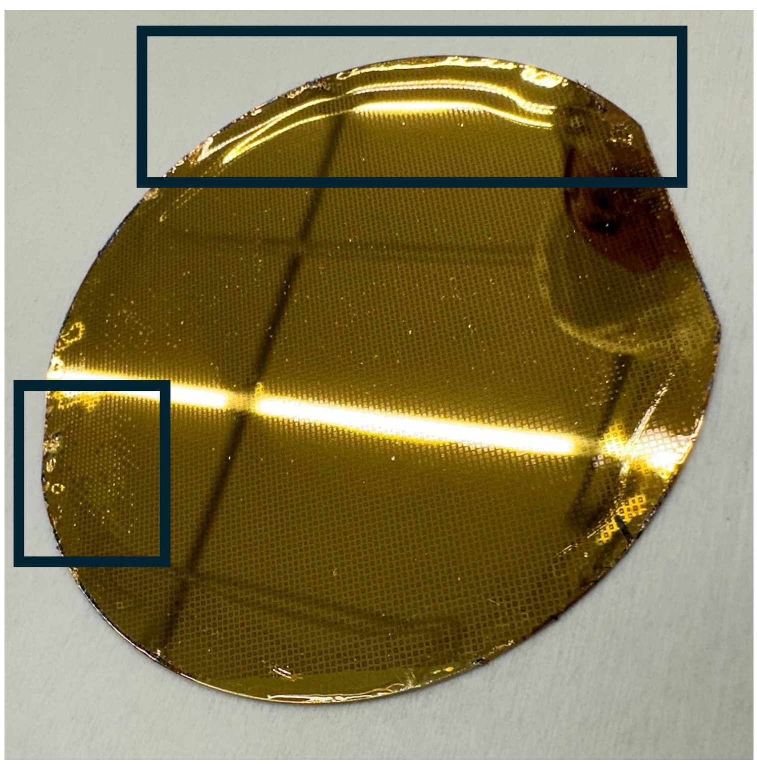

Figure 7.2: Nanofabricated metamaterial calibration target for bands C and D produced by Duke University. The top boxed area highlights the edge bead due to spin coating. The left boxed area contains a region of poor liftoff. The sample is highly reflective at optical wavelengths.

Table 7.1: Designed (measured) dimensions of the absorber elements for each frequency band.

Dimension (μm)	Band A	Band B	Band C	Band D
Side a	920 (886)	604 (608)	507 (508)	364 (366)
Perimeter width b	100 (77)	84 (83)	90 (89)	75 (76)
Fin width c	120 (102)	88 (100)	90 (89)	75 (76)
Center separation g	240 (270)	218 (230)	181 (181)	126 (127)
Dielectric thickness t	195	203	77	77

7.3 Monostatic Reflectivity Measurement

The absorptivity and, equivalently, the emissivity of the MMA targets were measured using the monostatic reflectivity experiment detailed in [102] and [103]. The experimental setup illustrated in Figure 7.3 was performed within an anechoic chamber providing at least 100 dB of isolation from DC to 220 GHz. The experiment, summarizing [103], is performed as follows. An antenna is placed at normal incidence at a distance, x_0, from the MMA such that x_0 is within the far-field region of the antenna. A source signal, a_0, is generated by a vector network analyzer (VNA) at a frequency f (using a high-frequency extension head, if necessary), and a returned signal, b_0, at f is measured. The target is translated in steps along $\hat{x}$, which extends the reference plane and enables finding the magnitude and phase of complex Γ. The full frequency bandwidth is measured at each step. The two signals are related by the scattering properties of the target and of the antenna, taking the form

$$\frac{b_0}{a_0}(x, f) = S_{00} - \Delta\Gamma \frac{e^{ik(x+x_0)}}{(x+x_0)^2}, \tag{7.1}$$

where $k = 2\pi f/c$ is the wavenumber, S_{00} is the complex antenna feed reflection, and Δ is a complex constant (units of m^2) collecting systematic terms including antenna receiving and transmitting properties [104]. Δ and S_{00} remain identical between calibrated measurements, meaning that a numerical fit determining $\Delta\Gamma$ for the MMA can be compared to that of a reflection standard with known $\Gamma_{ref} = -1$ to determine Γ. A reflection standard was made by cutting a sheet of polished aluminum to match the dimensions of the MMA wafer. The dimensions need to be matched so that each target occupies the same subtended angle within the antenna beam profile and Δ remains constant.

Figure 7.4 shows a measurement at a single frequency near f_D, with the voltage ratio measured

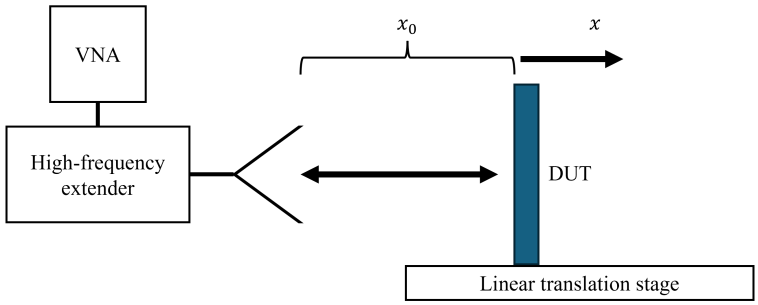

Figure 7.3: Monostatic reflection experimental setup. The experiment is performed in an anechoic chamber. The starting distance x_0 is within the far-field region of the antenna. Measurements are performed by a VNA across a desired frequency bandwidth for each step of distance in x.

by the VNA plotted versus the antenna-target distance minus $x_0 \approx 1\,\mathrm{m}$. The MMA is shown in red, and the reflection standard in blue. Crosses represent the measured data, and the solid lines are a numerical fit of those data to (7.1). The effect of energy absorption by the MMA is observed as the reduced voltage ratio amplitude. Γ is determined as a function of frequency by repeating this process for each frequency measured by the VNA.

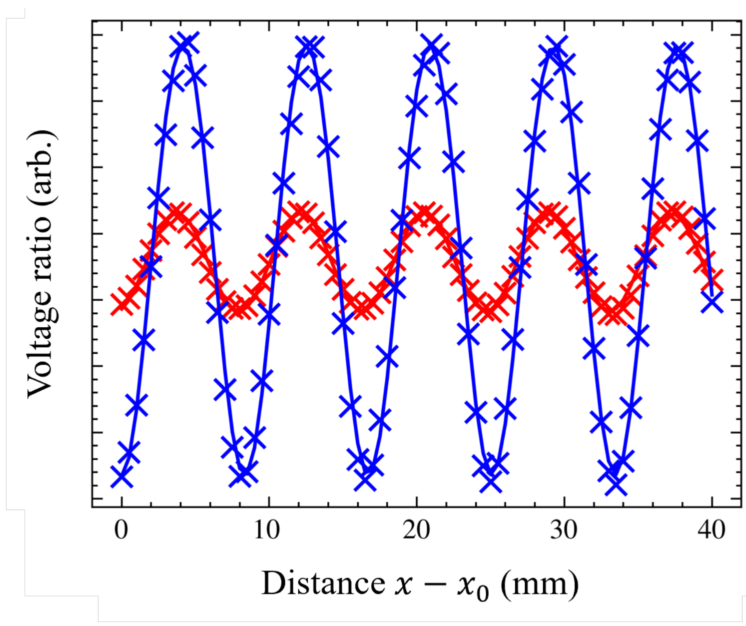

Figure 7.4: Monostatic reflectivity data measured by a VNA (crosses) and numerical fits to that data using Equation 7.1 (solid lines) for a single frequency near f_D of an MMA (red) and a reference standard of polished aluminum (blue), plotted versus the antenna-target distance relative to the starting point.

The measured absorption (return loss) in decibels, calculated as $L = -20\log_{10}|\Gamma|$, for each MMA frequency band is shown in Figure 7.5, and the results are collected in Table 7.2. Table 7.2

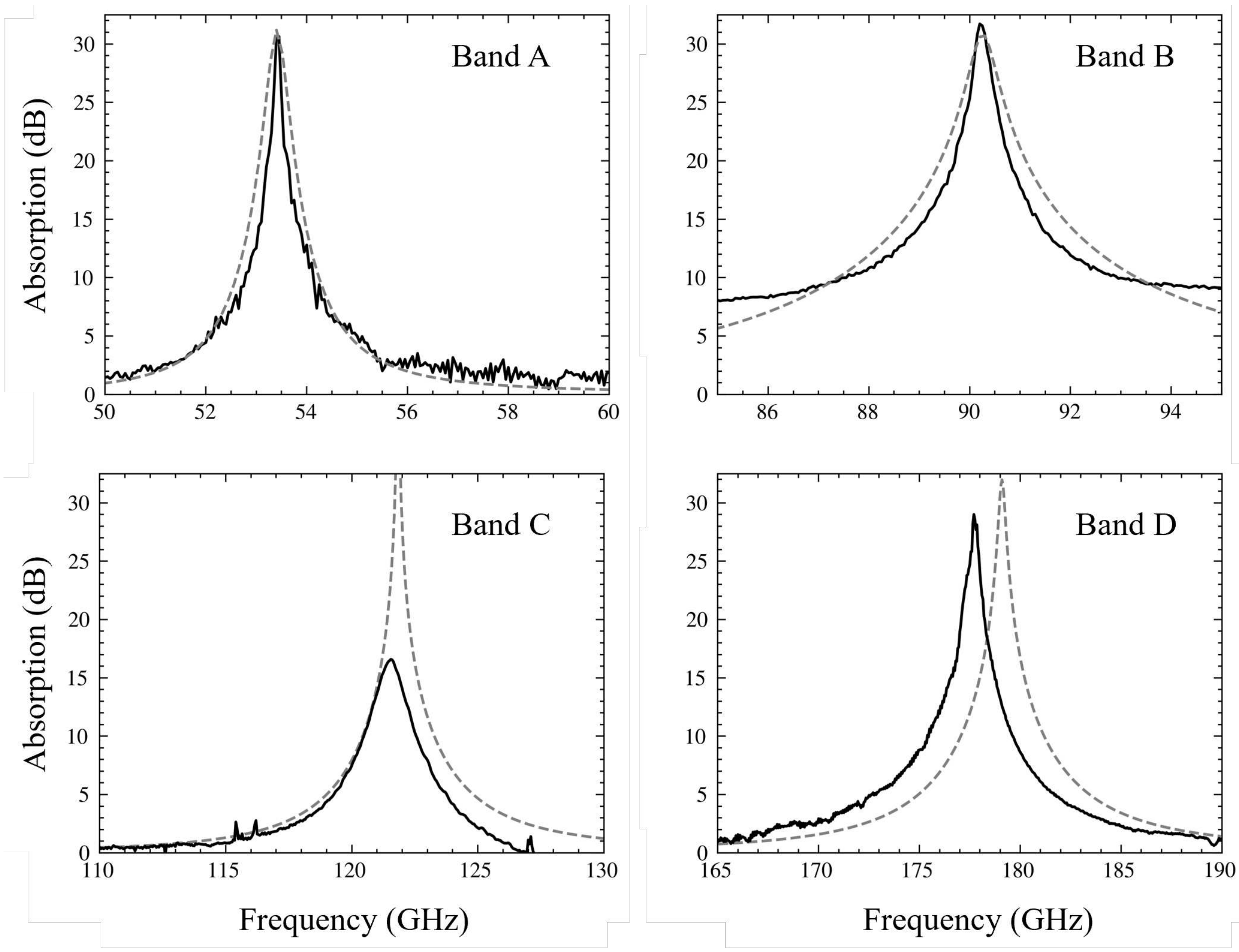

Figure 7.5: Absorption (return loss) plotted against frequency for MMA bands A, B, C, and D. Dashed gray lines show the result simulated in software, and solid black lines show the result from monostatic reflectivity measurements.

also includes the derived emissivity, calculated as

$$e = 1 - 10^{-L/10} = 1 - |\Gamma|^2 \,. \tag{7.2}$$

Dashed gray lines show the response simulated in software, and solid black lines show the experimental result. It is evident that there is excellent agreement between the two for the amplitude and frequency of maximum absorption ("center frequency") for bands A and B. Band C shows good agreement between simulated and measured center frequencies, but the measured absorption is less than predicted by nearly half; also, a negative return loss is observed at frequencies below 130 GHz. These can possibly be explained by regions of poor liftoff and/or edge-beading, as discussed

Table 7.2: Results of the monostatic reflection measurement.

MMA Frequency Band	Center Frequency (Simulated) (GHz)	Center Frequency (Measured) (GHz)	Absorption (Measured) (dB)	Emissivity (Derived)
A (Oxygen complex)	54.9	53.5	30.64	0.9991
B (Window channel)	90.3	90.2	31.72	0.9993
C (Oxygen line)	121.9	121.5	16.59	0.9781
D (Water vapor line)	179.1	177.7	29.00	0.9987

in Section 7.2. Regions of poor liftoff would be reflective, reducing total absorption. Edge-beading may introduce off-normal reflections that result in more energy directed to the antenna compared to the reflector standard. Band D is exhibits 29 dB of absorption, equal to an emissivity of 0.9987, but the center frequency is 1.4 GHz below the simulation, a shift of 0.8%. This is likely due to the absorber element dimensions, indicative of the tight tolerance requirements at higher frequencies. Table 7.1 shows that the measured dimensions are slightly greater than the design, and greater than 0.8%. Aligning the center frequencies reveals that the profiles are otherwise very similar, but the Band C discussion may still be relevant.

7.4 Radiometric Brightness Temperature

The High-frequency Airborne Microwave and Millimeter-wave Radiometer (HAMMR) is a cross-track scanning remote sensing instrument designed and fabricated by Colorado State University and the NASA/Caltech Jet Propulsion Laboratory for the NASA Instrument Incubator Program 2010 [105] that has a successful record of airborne measurement campaigns [85], [105]. HAMMR provides a remote sensing instrument that is directly relevant to the potential application of MMA-based calibration targets in Earth remote sensing radiometers, so a simple experiment was designed using HAMMR to determine emissivity. An outline is as follows. The MMA is placed inside of the antenna chamber of HAMMR (Figure 7.6) to reduce environmental influence, and calibrated measurements of the brightness temperature are performed. Platinum resistance thermometers (PRTs) are used to record the physical temperature of the MMA, which is controlled with a silicone heater. The brightness temperature and physical temperature data are used to determine emissivity according to the definition.

The HAMMR antenna chamber consists of three feedhorn antennas, a pair of mirrors, and an ambient load. The receiver antennas are for microwave, millimeter-wave, and sounding channels. The scene to be measured is reflected towards the feedhorn antennas by the mirrors: first by an ellipsoidal flat scanning mirror (major axis = 57.58 cm, minor axis = 40.64 cm) that rotates once per second, then by a fixed offset paraboloidal mirror. The calibration target is a layer of aluminum fins covered with absorptive material and angled at about 60 degrees. While HAMMR is taking measurements, the ambient load is used as a reference during each cycle of the rotating mirror. More complete details about HAMMR's design are provided in [85], [105], [106]. Measurements are made at twenty-five frequency channels between 18.7 GHz and 182.31 GHz. Due to physical constraints and the limited availability of the instrument, only band D was analyzed, using the eight frequency channels at and below 182.31 GHz.

The measured target was comprised of four layers: a thermal insulator (G-10), a silicone heater, an aluminum heat spreader, and the MMA. Polished aluminum was used to frame the circular MMA on the square target and was chosen so that measured brightness temperature would show a clear distinction between the hot MMA and cooler reflected environment. The target was placed at HAMMR's zenith position, normally incident via the mirrors to the feedhorn antennas, and on top of the existing calibration target, separated from it by the thermal insulator. PRTs were attached to the face of the MMA and abutting its side, and within the ambient load. The PRTs were connected to a temperature monitor, and a script was written to record and timestamp readings once per second. The timestamps were used to synchronize the PRT data with the data recorded and timestamped by HAMMR.

Calibrating HAMMR is detailed in [85] and summarized here. The process begins with two-point calibration measurements performed before and after the experiment. The cold load is an external calibration target cooled by liquid nitrogen (LN2). The two-point measurements create the following model of the receiver noise temperature:

$$T_{rec} = \frac{T_{amb} - T_{LN2}}{V_{amb} - V_{LN2}} V_{amb} - T_{amb}. \tag{7.3}$$

T_{amb} is measured by temperature sensors within the ambient load, and T_{LN2} is the boiling tem-

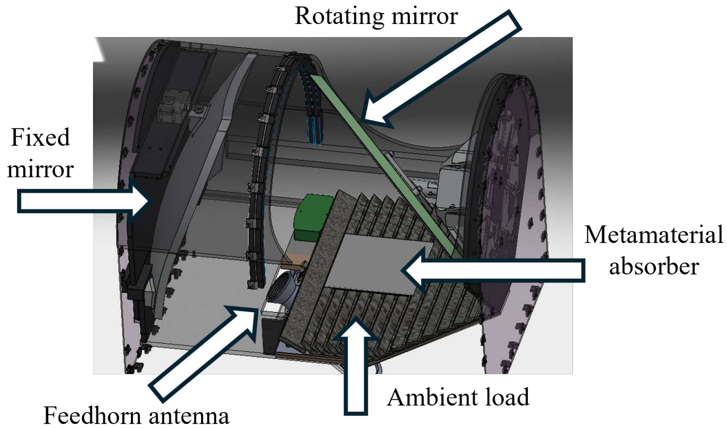

Figure 7.6: CAD drawing of the experimental setup for measuring the MMA using HAMMR. Pictured is the antenna cavity of HAMMR, containing an ambient load, two collection mirrors, and three feedhorn antennas. The MMA is mounted at the zenith-facing position. PRTs monitoring the physical temperature of the MMA are not pictured.

perature of LN2[14]. V_{amb} and V_{LN2} are the voltages measured by the radiometer. The cold and ambient temperatures should be as distant from each other as possible, and should ideally fully encompass the dynamic range of the intended measurement. During the experiment, the antenna calibration gain, G, is determined at each revolution of the scanning mirror from single-point calibration measurements of the ambient load and the physical temperature of the receiver by using the relation

$$T_{amb} = GV_{amb} - T_{rec}. \tag{7.4}$$

Radiometric measurements of the MMA were performed while increasing the MMA physical temperature, T_p, from ambient by using the heater. T_p was determined as the average of PRT readings from the four sensors on and abutting the MMA. Measurements were performed at 5 K intervals in T_p from 300 K to 345 K. The brightness temperature, T_B, was recorded in each frequency channel as a function of the motor angle and extracted using the mean of the first four rotations to reduce convective cooling effects from the rotating mirror. Figure 7.7 shows the resulting plot of T_B vs. T_p for the frequency channel at 179.31 GHz. The dashed line is a visual aid representing a perfect emitter with $T_B = T_p$.

The emissivity, e, of the MMA at each frequency is determined by using a numerical fit of the

[14]The LN2 boiling temperature was determined to be 76 K at local temperature and pressure using online tools [107], [108].

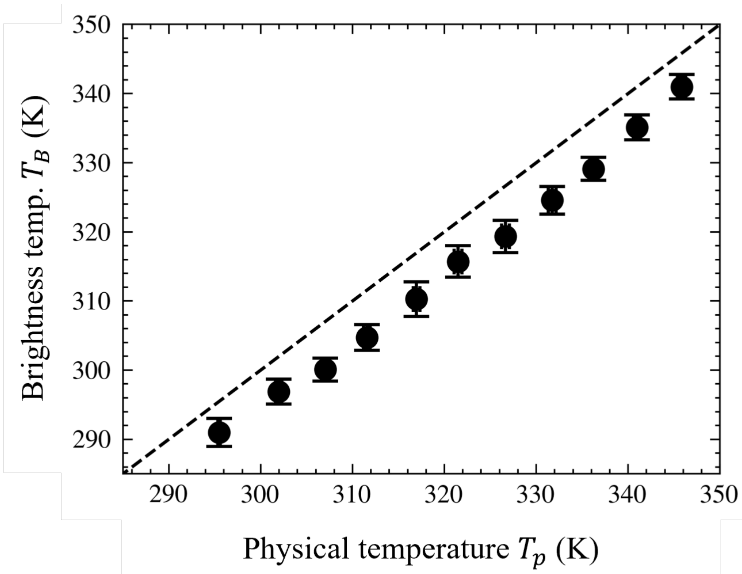

Figure 7.7: Brightness temperature T_B vs. physical temperature T_p of the MMA measured in one of HAMMR's frequency channels, f = 179.31 GHz. The dashed line represents a perfect emitter with $T_B = T_p$.

temperature data to the equation

$$T_B = eT_p + (1 - e)T_a + c, \tag{7.5}$$

where T_a is the ambient temperature as measured by a PRT in HAMMR's existing ambient load (approximately 300 K), and c is a mathematical offset for fitting that considers off-normal contributions. The second term on the right-hand side of (7.5) considers reflections of the environment from an imperfect emitter. Fitting for each of HAMMR's eight frequency channels yields the MMA emissivity as a function of those discrete frequencies. The results are collected in Table 7.3.

Table 7.3: Fitting results of measured data to (7.5).

Frequency f (GHz)	Emissivity e	Offset c
182.31	0.8883 ± 0.0289	-6.85 ± 0.76
181.31	0.9391 ± 0.0259	-7.13 ± 0.79
180.31	0.9703 ± 0.0212	-6.40 ± 0.55
179.31	0.9901 ± 0.0198	-5.95 ± 0.54
178.31	0.9952 ± 0.0188	-5.85 ± 0.50
177.31	0.9805 ± 0.0207	-5.24 ± 0.48
176.31	0.9310 ± 0.0133	-5.73 ± 0.33
175.31	0.9026 ± 0.0118	-5.62 ± 0.32

Figure 7.8 presents the emissivity results from the reflection measurement (blue points), radiometric measurement (black points), and simulation (red dashed line). As discussed in Section 7.3, the reflection measurement is offset from the simulation by -1.4 GHz, which is reasonable according to the measured dimensions of the sample. The radiometric result shows emissivity values comparable to the other data, but the bandwidth is greater than expected. There are three details of the experiment that could contribute to this measurement. First, the 3 dB footprint of the receiver antenna main lobe is approximately 8 mm at the MMA; by comparison, the reflectivity measurement places the sample entirely within the 3 dB footprint. A smaller antenna footprint would help to reduce edge beading and liftoff effects, which could show slightly increased emissivity and bandwidth. Second, emissivity could be systematically increased by possible errors in the two-point calibration that result in greater-than-actual T_B. This is suggested by the fitting offset values, c, and could be improved with additional calibration points and/or with a value of T_{hot} greater than the maximum T_p. Third, bandwidth could be increased by contributions from the ambient load via reflections or from antenna sidelobes. This could be reduced by better isolating the metamaterial sample from its surroundings.

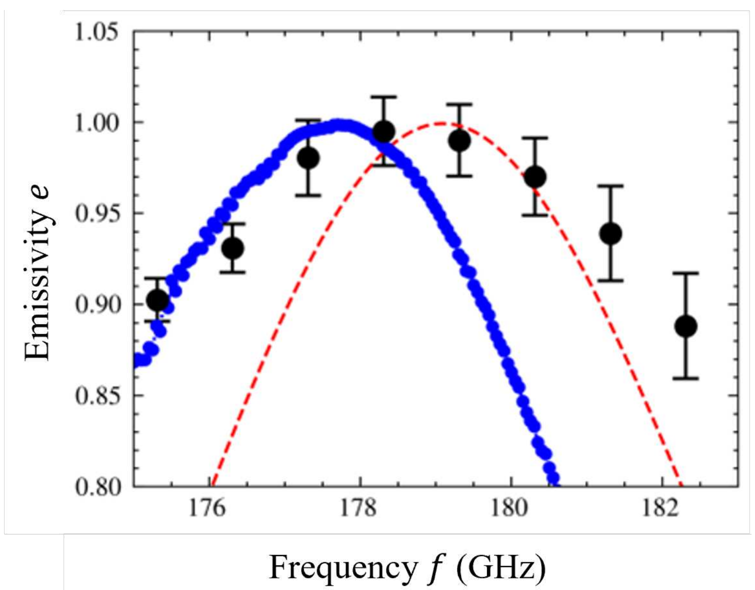

Figure 7.8: Emissivity of an MMA target in band D determined from the radiometric measurement (black points), monostatic reflectivity measurement (blue points), and simulation (dashed red line).

7.5 Conclusion

Blackbody calibration targets based on metamaterial absorbers (MMAs) provide a calibration reference standard that has significant advantages over current state-of-the-art targets used in passive microwave Earth remote sensing. The planar construction of MMAs mitigates uncertainties introduced by temperature gradients within traditional calibration targets, and the reduced mass and volume are well-suited for instruments with size, weight, and power constraints, such as SmallSats or CubeSats. MMAs can be fabricated with commercial printed-circuit board processing or standard photolithography, and can be designed to accomodate multiple frequencies of absorption. We have presented the design and emissive performance of MMA calibration targets at four frequency bands relevant to passive microwave remote sensing of the Earth's atmosphere. A monostatic reflectivity experiment shows that the MMA targets demonstrate emissivity values acceptable for remote sensor calibrations, and this result is corroborated at the highest frequency band with microwave radiometric measurements.

Chapter 8. Conclusion

This thesis has presented the work and results of three microwave studies performed at Colorado State University. Chapter 2 introduced magnetics and ferromagnetic resonance (FMR) as the phenomenon fundamental to the field of magnetization dynamics. Chapter 3 presented measurements of FMR at high temperatures to characterize the switching efficiency of materials being proposed as candidates for free layers in spin-transfer torque magnetostatic random-access memory (MRAM). High-temperature measurements of FMR have generally been desirable for hardware such as MRAM, and particularly for temperatures above 400 K. The interest was chiefly driven by research towards the development of heat-assisted magnetic recording (HAMR) devices. Creating the materials and technologies for HAMR has proven to be quite challenging. Seagate released HAMR drives for consumers in 2024, over five years after their first publicly-stated release target. Western Digital appears on track to release consumer drives in 2027, and released a statement in early 2026 discussing the cost and complexity of HAMR drives [109].

Chapter 4 expands the concept of FMR to non-uniform magnetic modes called spin waves, which have appealing properties for fundamental research on nonlinear waves and as information carriers complementary to existing electronics. To this end, Chapter 5 discusses the design and fabrication of passive devices called magnonic crystals, which manipulate the dispersion relation of propagating spin waves. The chapter considers a crystal with two periodicities as a straightforward evolution of the common singly-periodic design. Magnonic crystals provide a rich and still relatively-unexplored platform for studying spin waves. The magnetization dynamics lab, now at Northeastern University, will explore increasingly complex magnonic crystal designs as an experimental platform for fractional calculus.

Chapter 6 introduces radiometry as a method of determining atmospheric temperature and humidity from the microwave radiation that is passively-emitted by oxygen and water vapor. To accurately discern the low-power signals from system noise, radiometers rely on calibration targets with near-perfect absorption characteristics. Typical pyramidal targets have uncertainty introduced across their height, which is addressed by novel calibration targets based on planar metamaterial absorbers presented in Chapter 7. There are two active projects at Colorado State that continue the work in this chapter. In the first, the metamaterial absorber is being applied as the canvas of a radiometric scene generator. Localized heating of the metamaterial is used to "paint" an analog scene for a radiometer. This could provide complex, real-data test-cases for instruments and a method for comparing datasets between them. The second is a hyperspectral overhaul of the HAMMR instrument. Hyperspectral radiometry takes advantage of improvements in microwave hardware to provide digital channelization, enabling a huge increase in the number of measureable frequencies. HAMMR-HD is expected to perform airborne campaigns in mid-2026.

Bibliography

[1] D. M. Pozar, *Microwave Engineering*, Fourth. John Wiley & Sons, Inc., 2012, ISBN: 978-0-470-63155-3.

[2] J. D. Jackson, *Classical Electrodynamics*, 3rd ed. John Wiley & Sons, Inc., 1999.

[3] E. I. Green, "The story of q," *American Scientist*, vol. 43, pp. 584–594, Oct. 1955.

[4] R. B. Goldfarb, "Magnetic measurement techniques for materials characterization," in V. Franco and B. Dodrill, Eds. Springer Nature Switzerland AG, 2021, ch. Units for Magnetic Quantities, pp. 3–11.

[5] D. B. Newell, E. Tiesinga, et al., "The international system of units (si)," *NIST Special Publication*, vol. 330, no. 1, 2019.

[6] N. W. Ashcroft and N. D. Mermin, *Introduction to Solid State Physics*.

[7] D. D. Stancil and A. Prabhakar, *Spin Waves: Theory and Applications*. Springer US, 2009, ISBN: 978-0-387-77864-8 978-0-387-77865-5.

[8] K. Premasiri and X. P. Gao, "Tuning spin–orbit coupling in 2d materials for spintronics: A topical review," *Journal of Physics: Condensed Matter*, vol. 31, no. 19, p. 193 001, 2019.

[9] T. Gilbert, "A phenomenological theory of damping in ferromagnetic materials," *IEEE Transactions on Magnetics*, vol. 40, no. 6, pp. 3443–3449, Nov. 2004, ISSN: 1941-0069. DOI: 10.1109/TMAG.2004.836740.

[10] B. Heinrich, "Spin relaxation in magnetic metallic layers and multilayers," in *Ultrathin Magnetic Structures III: Fundamentals of Nanomagnetism*, J. Bland, C. Anthony, and B. Heinrich, Eds. Berlin, Heidelberg: Springer Berlin Heidelberg, 2005, pp. 143–210, ISBN: 978-3-540-27163-5. DOI: 10.1007/3-540-27163-5_5. [Online]. Available: https://doi.org/10.1007/3-540-27163-5_5.

[11] S. Technology. "What is mozaic 3+, how does it work, and what can it do for my data center? "[Online]. Available: https://www.seagate.com/resources/what-is-mozaic-3plus-how-does-it-work-and-what-can-it-do-for-my-data-center/.

[12] D. Richardson et al., "Near-tc ferromagnetic resonance and damping in fe pt-based heat-assisted magnetic recording media," *Physical Review Applied*, vol. 10, no. 5, p. 054 046, 2018.

[13] D. Richardson et al., "Interlayer exchange coupling in magnetic hard-soft bilayered structures," *Physical Review Applied*, vol. 11, no. 4, p. 044 016, 2019.

[14] M. Wu, "Solid state physics, vol. 62," in R. E. Camley and R. L. Stamps, Eds. Elsevier Inc., 2011, ch. Nonlinear Spin Waves in Magnetic Film Feedback Rings, pp. 163–224.

[15] K. C. Chun, H. Zhao, J. D. Harms, T.-H. Kim, J.-P. Wang, and C. H. Kim, "A scaling roadmap and performance evaluation of in-plane and perpendicular mtj based stt-mrams for high-density cache memory," *IEEE Journal of Solid-State Circuits*, vol. 48, no. 2, pp. 598–610, 2013. DOI: 10.1109/JSSC.2012.2224256.

[16] B. Tudu and A. Tiwari, "Recent developments in perpendicular magnetic anisotropy thin films for data storage applications," *Vacuum*, vol. 146, pp. 329–341, 2017, ISSN: 0042-207X. DOI: https://doi.org/10.1016/j.vacuum.2017.01.031. [Online]. Available: https://www.sciencedirect.com/science/article/pii/S0042207X17300155.

[17] R. Sbiaa, H. Meng, and S. N. Piramanayagam, "Materials with perpendicular magnetic anisotropy for magnetic random access memory," *physica status solidi (RRL) – Rapid Research Letters*, vol. 5, no. 12, pp. 413–419, 2011. DOI: https://doi.org/10.1002/pssr.201105420. eprint: https://onlinelibrary.wiley.com/doi/pdf/10.1002/pssr.201105420. [Online]. Available: https://onlinelibrary.wiley.com/doi/abs/10.1002/pssr.201105420.

[18] A. V. Khvalkovskiy et al., "Basic principles of stt-mram cell operation in memory arrays," *Journal of Physics D: Applied Physics*, vol. 46, no. 7, p. 074 001, Jan. 2013. DOI: 10.1088/0022-3727/46/7/074001. [Online]. Available: https://dx.doi.org/10.1088/0022-3727/46/7/074001.

[19] H. Sato, M. Yamanouchi, S. Ikeda, S. Fukami, F. Matsukura, and H. Ohno, "Perpendicular-anisotropy cofeb-mgo magnetic tunnel junctions with a mgo/cofeb/ta/cofeb/mgo recording structure," *Applied Physics Letters*, vol. 101, no. 2, p. 022 414, Jul. 2012, ISSN: 0003-6951. DOI: 10.1063/1.4736727. eprint: https://pubs.aip.org/aip/apl/article-pdf/doi/10.1063/1.4736727/13164620/022414_1_online.pdf. [Online]. Available: https://doi.org/10.1063/1.4736727.

[20] S. Couet et al., "Impact of ta and w-based spacers in double mgo stt-mram free layers on perpendicular anisotropy and damping," *Applied Physics Letters*, vol. 111, no. 15, p. 152 406, Oct. 2017, ISSN: 0003-6951. DOI: 10.1063/1.5000992. eprint: https://pubs.aip.org/aip/apl/article-pdf/doi/10.1063/1.5000992/13157538/152406_1_online.pdf. [Online]. Available: https://doi.org/10.1063/1.5000992.

[21] J. Chatterjee et al., "Reduced thermal variation of perpendicular magnetic anisotropy in magnetically stiffened dual-w composite storage layer for spin-transfer-torque magnetic random-access memory," *Phys. Rev. Appl.*, vol. 12, p. 044 043, 4 Oct. 2019. DOI: 10.1103/PhysRevApplied.12.044043. [Online]. Available: https://link.aps.org/doi/10.1103/PhysRevApplied.12.044043.

[22] T. S. Santos et al., "Ultrathin perpendicular free layers for lowering the switching current in stt-mram," *Journal of Applied Physics*, vol. 128, no. 11, p. 113 904, Sep. 2020, ISSN: 0021-8979. DOI: 10.1063/5.0022576. eprint: https://pubs.aip.org/aip/jap/article-pdf/doi/10.1063/5.0022576/13372944/113904_1_online.pdf. [Online]. Available: https://doi.org/10.1063/5.0022576.

[23] J. Kune š and V. Kamberský, "First-principles investigation of the damping of fast magnetization precession in ferromagnetic 3*d* metals," *Phys. Rev. B*, vol. 65, p. 212 411, 21 Jun. 2002. DOI: 10.1103/PhysRevB.65.212411. [Online]. Available: https://link.aps.org/doi/10.1103/PhysRevB.65.212411.

[24] V. Kamberský, "Spin-orbital gilbert damping in common magnetic metals," *Phys. Rev. B*, vol. 76, p. 134 416, 13 Oct. 2007. DOI: 10.1103/PhysRevB.76.134416. [Online]. Available: https://link.aps.org/doi/10.1103/PhysRevB.76.134416.

[25] K. Gilmore, Y. U. Idzerda, and M. D. Stiles, "Identification of the dominant precession-damping mechanism in fe, co, and ni by first-principles calculations," *Phys. Rev. Lett.*, vol. 99, p. 027 204, 2 Jul. 2007. DOI: 10.1103/PhysRevLett.99.027204. [Online]. Available: https://link.aps.org/doi/10.1103/PhysRevLett.99.027204.

[26] T. Qu and R. H. Victora, "Effect of substitutional defects on kambersky damping in l1 magnetic materials," *Applied Physics Letters*, vol. 106, no. 7, p. 072 404, Feb. 2015, ISSN: 0003-6951. DOI: 10.1063/1.4909510. eprint: https://pubs.aip.org/aip/apl/article-pdf/doi/10.1063/1.4909510/14467167/072404_1_online.pdf. [Online]. Available: https://doi.org/10.1063/1.4909510.

[27] S. Ikeda et al., "Tunnel magnetoresistance of 604% at 300k by suppression of ta diffusion in cofeb/ mgo/ cofeb pseudo-spin-valves annealed at high temperature," *Applied Physics Letters*, vol. 93, no. 8, 2008.

[28] J. Swerts et al., "Beol compatible high tunnel magneto resistance perpendicular magnetic tunnel junctions using a sacrificial mg layer as cofeb free layer cap," *Applied Physics Letters*, vol. 106, no. 26, p. 262 407, Jul. 2015, ISSN: 0003-6951. DOI: 10.1063/1.4923420. eprint: https://pubs.aip.org/aip/apl/article-pdf/doi/10.1063/1.4923420/14467957/262407_1_online.pdf. [Online]. Available: https://doi.org/10.1063/1.4923420.

[29] M. D. Kuz'min, "Shape of temperature dependence of spontaneous magnetization of ferromagnets: Quantitative analysis," *Phys. Rev. Lett.*, vol. 94, p. 107 204, 10 Mar. 2005. DOI: 10.1103/PhysRevLett.94.107204. [Online]. Available: https://link.aps.org/doi/10.1103/PhysRevLett.94.107204.

[30] M. D. Kuz'min, M. Richter, and A. N. Yaresko, "Factors determining the shape of the temperature dependence of the spontaneous magnetization of a ferromagnet," *Phys. Rev. B*, vol. 73, p. 100 401, 10 Mar. 2006. DOI: 10.1103/PhysRevB.73.100401. [Online]. Available: https://link.aps.org/doi/10.1103/PhysRevB.73.100401.

[31] S. Srivastava et al., "Effect of $(\mathrm{Co}_x\mathrm{Fe}_{1-x})_{80}\mathrm{B}_{20}$ composition on the magnetic properties of the free layer in double-barrier magnetic tunnel junctions," *Phys. Rev. Appl.*, vol. 10, p. 024 031, 2 Aug. 2018. DOI: 10.1103/PhysRevApplied.10.024031. [Online]. Available: https://link.aps.org/doi/10.1103/PhysRevApplied.10.024031.

[32] J. M. Iwata-Harms et al., "High-temperature thermal stability driven by magnetization dilution in CoFeB free layers for spin-transfer-torque magnetic random access memory," *Scientific Reports*, vol. 8, no. 1, p. 14 409, Sep. 2018, ISSN: 2045-2322. DOI: 10.1038/s41598-018-32641-6.

[33] J. Ding et al., "Nanometer-thick yttrium iron garnet films with perpendicular anisotropy and low damping," *Phys. Rev. Appl.*, vol. 14, p. 014 017, 1 Jul. 2020. DOI: 10.1103/PhysRevApplied.14.014017. [Online]. Available: https://link.aps.org/doi/10.1103/PhysRevApplied.14.014017.

[34] D. Richardson, K. Srinivasan, S. Katz, and M. Wu, "Quantification of intergranular exchange coupling in coptcr-based perpendicular recording media via ferromagnetic resonance measurements," *Applied Physics Letters*, vol. 111, no. 18, p. 183 506, Nov. 2017, ISSN: 0003-6951. DOI: 10.1063/1.4990949. eprint: https://pubs.aip.org/aip/apl/article-pdf/doi/10.1063/1.4990949/13923307/183506_1_online.pdf. [Online]. Available: https://doi.org/10.1063/1.4990949.

[35] D. Richardson et al., "Near-tc ferromagnetic resonance and damping in FePt-based heat-assisted magnetic recording media," *Phys. Rev. Appl.*, vol. 10, p. 054 046, 5 Nov. 2018. DOI: 10.1103/PhysRevApplied.10.054046. [Online]. Available: https://link.aps.org/doi/10.1103/PhysRevApplied.10.054046.

[36] D. Richardson et al., "Interlayer exchange coupling in magnetic hard-soft bilayered structures," *Phys. Rev. Appl.*, vol. 11, p. 044 016, 4 Apr. 2019. DOI: 10.1103/PhysRevApplied.11.044016. [Online]. Available: https://link.aps.org/doi/10.1103/PhysRevApplied.11.044016.

[37] C. Liu et al., "Ferromagnetic resonance in fept thin films at elevated temperatures," *Journal of Magnetism and Magnetic Materials*, vol. 563, p. 169 988, 2022, ISSN: 0304-8853. DOI: https://doi.org/10.1016/j.jmmm.2022.169988. [Online]. Available: https://www.sciencedirect.com/science/article/pii/S0304885322008733.

[38] E. Montoya, T. McKinnon, A. Zamani, E. Girt, and B. Heinrich, "Broadband ferromagnetic resonance system and methods for ultrathin magnetic films," *Journal of Magnetism and Magnetic Materials*, vol. 356, pp. 12–20, 2014, ISSN: 0304-8853. DOI: https://doi.org/10.1016/j.jmmm.2013.12.032. [Online]. Available: https://www.sciencedirect.com/science/article/pii/S0304885313009256.

[39] G. Woltersdorf, "Spin-pumping and two-magnon scattering in magnetic multilayers," Ph.D. dissertation, Simon Fraser University, 2004.

[40] M. Sparks, *Ferromagnetic-Relaxation Theory*. McGraw-Hill, 1964.

[41] C. Scheck, L. Cheng, and W. E. Bailey, "Low damping in epitaxial sputtered iron films," *Applied Physics Letters*, vol. 88, no. 25, p. 252 510, Jun. 2006, ISSN: 0003-6951. DOI: 10.1063/1.2216031. eprint: https://pubs.aip.org/aip/apl/article-pdf/doi/10.1063/1.2216031/14353883/252510_1_online.pdf. [Online]. Available: https://doi.org/10.1063/1.2216031.

[42] R. McMichael and P. Krivosik, "Classical model of extrinsic ferromagnetic resonance linewidth in ultrathin films," *IEEE Transactions on Magnetics*, vol. 40, no. 1, pp. 2–11, 2004. DOI: 10.1109/TMAG.2003.821564.

[43] P. Krivosik, N. Mo, S. Kalarickal, and C. E. Patton, "Hamiltonian formalism for two magnon scattering microwave relaxation: Theory and applications," *Journal of Applied Physics*, vol. 101, no. 8, p. 083 901, Apr. 2007, ISSN: 0021-8979. DOI: 10.1063/1.2717084. eprint: https://pubs.aip.org/aip/jap/article-pdf/doi/10.1063/1.2717084/14986853/083901_1_online.pdf. [Online]. Available: https://doi.org/10.1063/1.2717084.

[44] P. Landeros, R. E. Arias, and D. L. Mills, "Two magnon scattering in ultrathin ferromagnets: The case where the magnetization is out of plane," *Phys. Rev. B*, vol. 77, p. 214 405, 21 Jun. 2008. DOI: 10.1103/PhysRevB.77.214405. [Online]. Available: https://link.aps.org/doi/10.1103/PhysRevB.77.214405.

[45] N. Mo et al., "Origins of the damping in perpendicular media: Three component ferromagnetic resonance linewidth in co–cr–pt alloy films," *Applied Physics Letters*, vol. 92, no. 2, p. 022 506, Jan. 2008, ISSN: 0003-6951. DOI: 10.1063/1.2834835. eprint: https://pubs.aip.org/aip/apl/article-pdf/doi/10.1063/1.2834835/14386743/022506_1_online.pdf. [Online]. Available: https://doi.org/10.1063/1.2834835.

[46] P. Krivosik, S. S. Kalarickal, N. Mo, S. Wu, and C. E. Patton, "Ferromagnetic resonance and damping in granular co–cr films with perpendicular anisotropy," *Applied Physics Letters*, vol. 95, no. 5, p. 052 509, Aug. 2009, ISSN: 0003-6951. DOI: 10.1063/1.3200238. eprint: https://pubs.aip.org/aip/apl/article-pdf/doi/10.1063/1.3200238/13085241/052509_1_online.pdf. [Online]. Available: https://doi.org/10.1063/1.3200238.

[47] B. Heinrich and J. A. C. Bland, *Ultrathin Magnetic Structures: Fundamentals of Nanomagnetism*. Springer, 2005.

[48] R. Urban, G. Woltersdorf, and B. Heinrich, "Gilbert damping in single and multilayer ultrathin films: Role of interfaces in nonlocal spin dynamics," *Phys. Rev. Lett.*, vol. 87, p. 217 204, 21 Nov. 2001. DOI: 10.1103/PhysRevLett.87.217204. [Online]. Available: https://link.aps.org/doi/10.1103/PhysRevLett.87.217204.

[49] Y. Tserkovnyak, A. Brataas, and G. E. W. Bauer, "Enhanced gilbert damping in thin ferromagnetic films," *Phys. Rev. Lett.*, vol. 88, p. 117 601, 11 Feb. 2002. DOI: 10.1103/PhysRevLett.88.117601. [Online]. Available: https://link.aps.org/doi/10.1103/PhysRevLett.88.117601.

[50] B. Heinrich et al., "Spin pumping at the magnetic insulator (yig)/normal metal (au) interfaces," *Phys. Rev. Lett.*, vol. 107, p. 066 604, 6 Aug. 2011. DOI: 10.1103/PhysRevLett.107.066604. [Online]. Available: https://link.aps.org/doi/10.1103/PhysRevLett.107.066604.

[51] J. Ding et al., "Large damping enhancement in dirac-semimetal–ferromagnetic-metal layered structures caused by topological surface states," *Advanced Functional Materials*, vol. 31, no. 11, p. 2 008 411, 2021. DOI: https://doi.org/10.1002/adfm.202008411. eprint: https://onlinelibrary.wiley.com/doi/pdf/10.1002/adfm.202008411. [Online]. Available: https://onlinelibrary.wiley.com/doi/abs/10.1002/adfm.202008411.

[52] D. Jhajhria, N. Behera, D. K. Pandya, and S. Chaudhary, "Dependence of spin pumping in w/cofeb heterostructures on the structural phase of tungsten," *Phys. Rev. B*, vol. 99, p. 014 430, 1 Jan. 2019. DOI: 10.1103/PhysRevB.99.014430. [Online]. Available: https://link.aps.org/doi/10.1103/PhysRevB.99.014430.

[53] S. Ikeda et al., "A perpendicular-anisotropy CoFeB–MgO magnetic tunnel junction," *Nature Materials*, vol. 9, no. 9, pp. 721–724, Sep. 2010, ISSN: 1476-4660. DOI: 10.1038/nmat2804.

[54] A. V. Chumak et al., "Advances in magnetics roadmap on spin-wave computing," *IEEE Transactions on Magnetics*, vol. 58, no. 6, pp. 1–72, 2022. DOI: 10.1109/TMAG.2022.3149664.

[55] K. O. Levchenko, K. Davídková, J. Mikkelsen, and A. V. Chumak, *Review on spin-wave rf applications*, 2024. arXiv: 2411.19212 [physics.app-ph]. [Online]. Available: https://arxiv.org/abs/2411.19212.

[56] A. Chumak, A. Serga, and B. Hillebrands, "Magnonic crystals for data processing," *Journal of Physics D: Applied Physics*, vol. 50, no. 24, p. 244 001, 2017.

[57] A. Chumak, A. Serga, S. Wolff, B. Hillebrands, and M. Kostylev, "Design and optimization of one-dimensional ferrite-film based magnonic crystals," *Journal of Applied Physics*, vol. 105, no. 8, 2009.

[58] H. Qin and S. Van Dijken, "Nanometer-thick YIG-based magnonic crystals: Bandgap dependence on groove depth, lattice constant, and film thickness," *Applied Physics Letters*, vol. 116, no. 20, p. 202 403, May 18, 2020, ISSN: 0003-6951, 1077-3118. DOI: 10.1063/5.0009807.

[59] D. Richardson, B. A. Kalinikos, L. D. Carr, and M. Wu, "Spontaneous exact spin-wave fractals in magnonic crystals," *Physical Review Letters*, vol. 121, no. 10, p. 107 204, 2018.

[60] R. Shindou, R. Matsumoto, S. Murakami, and J.-i. Ohe, "Topological chiral magnonic edge mode in a magnonic crystal," *Physical Review B—Condensed Matter and Materials Physics*, vol. 87, no. 17, p. 174 427, 2013.

[61] Y.-M. Li, J. Xiao, and K. Chang, "Topological magnon modes in patterned ferrimagnetic insulator thin films," *Nano Letters*, vol. 18, no. 5, pp. 3032–3037, 2018.

[62] M. Kostylev et al., "Partial frequency band gap in one-dimensional magnonic crystals," *Applied Physics Letters*, vol. 92, no. 13, 2008.

[63] Z. Wang et al., "Observation of frequency band gaps in a one-dimensional nanostructured magnonic crystal," *Applied Physics Letters*, vol. 94, no. 8, 2009.

[64] A. Chumak, A. Serga, S. Wolff, B. Hillebrands, and M. Kostylev, "Design and optimization of one-dimensional ferrite-film based magnonic crystals," *Journal of Applied Physics*, vol. 105, no. 8, 2009.

[65] G. Gubbiotti, S. Tacchi, M. Madami, G. Carlotti, A. Adeyeye, and M. Kostylev, "Brillouin light scattering studies of planar metallic magnonic crystals," *Journal of Physics D: Applied Physics*, vol. 43, no. 26, p. 264 003, 2010.

[66] A. B. Ustinov, B. A. Kalinikos, V. E. Demidov, and S. O. Demokritov, "Formation of gap solitons in ferromagnetic films with a periodic metal grating," *Physical Review B—Condensed Matter and Materials Physics*, vol. 81, no. 18, p. 180 406, 2010.

[67] H. Qin and S. van Dijken, "Nanometer-thick yig-based magnonic crystals: Bandgap dependence on groove depth, lattice constant, and film thickness," *Applied Physics Letters*, vol. 116, no. 20, 2020.

[68] M. Morozova, O. Matveev, Y. P. Sharaevskii, S. Nikitov, and A. Sadovnikov, "Nonlinear signal processing with magnonic superlattice with two periods," *Applied Physics Letters*, vol. 120, no. 12, 2022.

[69] D. D. Stancil and A. Prabhakar, *Spin Waves: Theory and Applications.* Springer US, 2009.

[70] L. Temdie et al., "Chiral excitation of exchange spin waves using gold nanowire grating," *Magnetochemistry*, vol. 9, no. 8, p. 199, 2023.

[71] H. Qin et al., "Nanoscale magnonic fabry-pérot resonator for low-loss spin-wave manipulation," *Nature communications*, vol. 12, no. 1, p. 2293, 2021.

[72] M. Wu, "Nonlinear spin waves in magnetic film feedback rings," in Elsevier, 2010, vol. 62, pp. 163–224.

[73] M. Wu, B. A. Kalinikos, P. Krivosik, and C. E. Patton, "Fast pulse-excited spin waves in yttrium iron garnet thin films," *Journal of applied physics*, vol. 99, no. 1, 2006.

[74] A. Chumak, A. Serga, B. Hillebrands, and M. Kostylev, "Scattering of backward spin waves in a one-dimensional magnonic crystal," *Applied Physics Letters*, vol. 93, no. 2, 2008.

[75] A. V. Chumak et al., "Spin-wave propagation in a microstructured magnonic crystal," *Applied Physics Letters*, vol. 95, no. 26, 2009.

[76] T. Langner et al., "Spin-wave propagation through a magnonic crystal in a thermal gradient," *Journal of Physics D: Applied Physics*, vol. 51, no. 34, p. 344 002, 2018.

[77] B. Jonsson and S. T. Eng, "Solving the schrodinger equation in arbitrary quantum-well potential profiles using the transfer matrix method," *IEEE journal of quantum electronics*, vol. 26, no. 11, pp. 2025–2035, 1990.

[78] F. Barath, A. Barrett, J. Copeland, D. Jones, and A. Lilley, "Mariner ii: Preliminary reports on measurements of venus: Microwave radiometers," *Science*, vol. 139, no. 3558, pp. 908–909, 1963.

[79] N. Skou and D. Le Vine, *Microwave Radiometer Systems: Design and Analysis*, 2nd ed. Artech House, Inc., 2006, ISBN: 1-58053-974-2.

[80] N. Telecommunications and I. Administration, *United states frequency allocation chart*, online, 2025. [Online]. Available: `https://www.ntia.gov/page/united-states-frequency-allocation-chart`.

[81] N. Oceanic and A. Administration, *Radiosondes*, online, Sep. 2025. [Online]. Available: `https://www.noaa.gov/jetstream/upperair/radiosondes`.

[82] H. Nyquist, "Thermal agitation of electric charge in conductors," *Phys. Rev.*, vol. 32, pp. 110–113, 1 Jul. 1928. DOI: `10.1103/PhysRev.32.110`. [Online]. Available: `https://link.aps.org/doi/10.1103/PhysRev.32.110`.

[83] S. T. Brown, A. Tanner, S. C. Reising, and W. Berg, "Single-point calibration for microwave sounders: Application to tempest-d," *Journal of Atmospheric and Oceanic Technology*, vol. 40, no. 6, pp. 669–676, 2023.

[84] F. T. Ulaby and D. G. Long, *Microwave Radar and Radiometric Remote Sensing*.

[85] X. Bosch-Lluis et al., "Instrument Design and Performance of the High-Frequency Airborne Microwave and Millimeter-Wave Radiometer," *IEEE Journal of Selected Topics in Applied Earth Observations and Remote Sensing*, vol. 12, no. 11, pp. 4563–4577, Nov. 2019, ISSN: 1939-1404, 2151-1535. DOI: `10.1109/JSTARS.2019.2949590`.

[86] S. T. Brown, S. Desai, W. Lu, and A. Tanner, "On the long-term stability of microwave radiometers using noise diodes for calibration," *IEEE Transactions on Geoscience and Remote Sensing*, vol. 45, no. 7, pp. 1908–1920, 2007. DOI: `10.1109/TGRS.2006.888098`.

[87] A. E. Cox and M. D. Janezic, "Preliminary studies of electromagnetic properties of microwave absorbing materials used in calibration targets," in *2006 IEEE International Geoscience and Remote Sensing Symposium Digest*, 2006.

[88] D. W. Draper, D. A. Newell, D. A. Teusch, and P. K. Yoho, "Global Precipitation Measurement Microwave Imager Prelaunch Hot Load Calibration," *IEEE Transactions on Geoscience and Remote Sensing*, vol. 51, no. 9, pp. 4731–4742, Sep. 2013, ISSN: 1558-0644. DOI: `10.1109/TGRS.2013.2239300`.

[89] D. W. Draper, D. A. Newell, F. J. Wentz, S. Krimchansky, and G. M. Skofronick-Jackson, "The Global Precipitation Measurement (GPM) Microwave Imager (GMI): Instrument Overview and Early On-Orbit Performance," *IEEE Journal of Selected Topics in Applied Earth Observations and Remote Sensing*, vol. 8, no. 7, pp. 3452–3462, Jul. 2015, ISSN: 2151-1535. DOI: `10.1109/JSTARS.2015.2403303`.

[90] A. Murk et al., "Development of microwave calibration targets for upcoming esa missions," in *2012 IEEE International Geoscience and Remote Sensing Symposium*, 2012, pp. 2949–2952. DOI: `10.1109/IGARSS.2012.6350707`.

[91] E. M. Twarog, W. E. Purdy, P. W. Gaiser, K. H. Cheung, and B. E. Kelm, "Windsat on-orbit warm load calibration," *IEEE Transactions on Geoscience and Remote Sensing*, vol. 44, no. 3, pp. 516–529, 2006.

[92] D. J. Fixsen, "The temperature of the cosmic microwave background," *The Astrophysical Journal*, vol. 707, no. 2, p. 916, 2009.

[93] D. Le Vine and S. Abraham, "Galactic noise and passive microwave remote sensing from space at l-band," *IEEE Transactions on Geoscience and Remote Sensing*, vol. 42, no. 1, pp. 119–129, 2004. DOI: 10.1109/TGRS.2003.817977.

[94] D. Albers, "Design, fabrication, and demonstration of low-mass, low-power, small-volume, direct detection millimeter-wave radiometers at 92 and 130 ghz," M.S. thesis, Colorado State University, 2012.

[95] N. I. Landy, S. Sajuyigbe, J. J. Mock, D. R. Smith, and W. J. Padilla, "Perfect metamaterial absorber," *Phys. Rev. Lett.*, vol. 100, p. 207 402, 20 May 2008. DOI: 10.1103/PhysRevLett.100.207402. [Online]. Available: https://link.aps.org/doi/10.1103/PhysRevLett.100.207402.

[96] C. M. Watts, X. Liu, and W. J. Padilla, "Metamaterial Electromagnetic Wave Absorbers," *Advanced Materials*, vol. 24, no. 23, Jun. 2012, ISSN: 0935-9648, 1521-4095. DOI: 10.1002/adma.201200674.

[97] A. Gagnon et al., "An initial validation of the nasa tropics pathfinder microwave radiometer observations," *IEEE Journal of Selected Topics in Applied Earth Observations and Remote Sensing*, vol. 18, pp. 2512–2525, 2025. DOI: 10.1109/JSTARS.2024.3518541.

[98] S. Padmanabhan et al., "Tempest-d radiometer: Instrument description and prelaunch calibration," *IEEE Transactions on Geoscience and Remote Sensing*, vol. 59, no. 12, pp. 10 213–10 226, 2020.

[99] H. King et al., "The 90 ghz radiometric imaging," NASA, Tech. Rep., 1976.

[100] "Mirs - microwave integrated retrieval system - instrument description - mhs," Accessed: Dec. 15, 2025. [Online]. Available: https://www.star.nesdis.noaa.gov/mirs/mhs.php.

[101] "Gpm microwave imager (gmi) — nasa global precipitation measurement mission," Accessed: Dec. 15, 2025. [Online]. Available: https://gpm.nasa.gov/missions/GPM/GMI.

[102] D. Gu, D. Houtz, J. Randa, and D. K. Walker, "Reflectivity Study of Microwave Blackbody Target," *IEEE Transactions on Geoscience and Remote Sensing*, vol. 49, no. 9, pp. 3443–3451, Sep. 2011, ISSN: 0196-2892, 1558-0644. DOI: 10.1109/TGRS.2011.2125975.

[103] D. Gu et al., "Characterization of Microwave Blackbody with Monostatic Measurement," in *IGARSS 2024 - 2024 IEEE International Geoscience and Remote Sensing Symposium*, Jul. 2024, pp. 6262–6267. DOI: 10.1109/IGARSS53475.2024.10641062.

[104] D. M. Kerns, *Plane-wave scattering-matrix theory of antennas and antenna-antenna interactions*. US Department of Commerce, National Bureau of Standards, 1981, vol. 162.

[105] T. Johnson, "Integration, characterization, and calibration of the highfrequency airborne microwave and millimeter-wave radiometer (HAMMR) instrument," M.S. thesis, Colorado State University, United States – Colorado, 2014, 278 pp., ISBN: 9781321491456.

[106] V. D. Hadel, "Development of internally-calibrated, direct detection millimeter-wave radiometers to improve remote sensing of wet-tropospheric path delay," Ph.D. dissertation, Colorado State University, 2015.

[107] "About the fort collins weather station," Accessed: Aug. 8, 2024. [Online]. Available: https://climate.colostate.edu/~autowx/fclwx_about.php.

[108] "Thermophysical properties of fluid systems," Accessed: Aug. 8, 2024. [Online]. Available: https://webbook.nist.gov/chemistry/fluid/.

[109] B. Warbiany, *The hamr future*, Feb. 2026. [Online]. Available: https://blog.westerndigital.com/hamr-technology-future-hdd-storage-capacity/.

[110] C. A. Mack, *The basics of microlithography*, Online, 2023.

[111] *Technical datasheet az 1500 series*, Rev. 03/21, Merck KGaA, 2021. [Online]. Available: https://www.microchemicals.com/dokumente/datenblaetter/tds/merck/en/tds_az_1500_series.pdf.

[112] A. DeMann, *Laser lithography*, Online, 2018. [Online]. Available: https://physlabs.colostate.edu/lithography/contact/.

[113] T. Goto et al., "Three port logic gate using forward volume spin wave interference in a thin yttrium iron garnet film," *Scientific Reports*, vol. 9, no. 1, p. 16 472, Nov. 2019, ISSN: 2045-2322. DOI: 10.1038/s41598-019-52889-w.

[114] Y. Okamura, M. Ishida, and S. Yamamoto, "Magnetooptic rib waveguides in yig: An experiment," *Applied optics*, vol. 23, no. 1, pp. 124–126, 1984.

Wet-Etching Yttrium Iron Garnet

The magnonic crystals presented in Chapter 5 were fabricated using a standard photolithography process. The key parts of the recipe are summarized in the paper, but a fuller explanation is provided here. This recipe is certainly not perfect, but should provide a starting point that can be further refined. Many of the settings I used were established by other students who were also working with YIG, and I refered the blog in Reference [110] as an introduction.

1. Prepare and clean the sample.

   A uniform YIG sample is first prepared by cleaning with acetone and isopropyl alcohol (IPA) in an ultrasonic cleaner.

2. Coat the sample with photoresist using a spin-coater.

   The photoresist used was AZ 1512, and the spin-coater was set to 30 s at 4500 rpm. AZ 1512 is a positive photoresist, meaning that exposed sections will be removed. Spin curves, which plot the resulting thickness against the rpm, should be provided on a datasheet. The photoresist is light sensitive—at this point, the sample should be kept out of direct exposure except at non-reactive frequencies.

3. Soft-bake the sample on a hotplate.

   Soft-baking (or pre-baking) the sample adheres the photoresist to the sample. The AZ 1500 series datasheet [111] suggests a soft-bake temperature of 90–110 °C, and a higher temperature for better adhesion to metals. This recipe uses 120 °C for one minute.

4. Expose the photoresist.

   The physics department at Colorado State University has an LW405C laser writer for maskless exposure [112], using a 405 nm GaN laser diode at 60–100 mW. This enables rapid prototyping. On the laser writer, this recipe used lens number 3, an exposure setting of 21.7 equivalent to 261 $\mathrm{mJ\,cm^{-2}}$, and a filter setting of 30.

5. (Optional) Post-bake the sample.

   Post-exposure bakes can help to remove standing-wave patterns in the thickness of the photoresist that are created by reflections from the sample during the exposure. This recipe did not perform a post-bake.

6. Develop the photoresist.

   The liquid developer was AZ 917 MIF, from the same provider as for the photoresist. Developer was dropped on top of the sample (called puddle developing) for one minute. Afterwards, the sample is rinsed and the exposed photoresist is removed. The sample can now be safely exposed to general lighting.

7. Hard-bake the sample.

   This step hardens the photoresist, making it more resilient to the high-temperature acid used for etching. Without this step, the photoresist may lift off entirely when placed in the acid.

8. Etch the sample.

   YIG will be chemically removed by (ortho)phosphoric acid, H_3PO_4, at a rate that increases with acid temperature. Literature values include 1.7 $\mathrm{nm\,s^{-1}}$ at 140 °C [113], 16.7 $\mathrm{nm\,s^{-1}}$ at 160 °C [57], and 300 $\mathrm{nm\,s^{-1}}$ at 270 °C [114]. This recipe used 160 °C but found the rate to be closer to 10 $\mathrm{nm\,s^{-1}}$, likely due to uncertainty in the acid temperature. A uniform acid temperature is critical to an even etch, so some sort of temperature bath should be used to achieve this. An alumina-pellet bath was used at Colorado State University, but other options include baths of oil or sand or glycerine, or heated aluminum blocks.

9. Remove remaining photoresist.

   This step is made much more difficult by the hard-bake; however, a combination of the cleaning process in step 1 and using dedicated photoresist remover should work. A successful removal used remover at 70 °C on a hotplate for 30 minutes, then rinsed in IPA and water.